VRIJE
UNIVERSITEIT
BRUSSEL

Master thesis in Physics and Astronomy.

PROBING A FREEZE-IN DARK MATTER MODEL WITH GRAVITATIONAL WAVES

Max Lalleman

2020-2021

Promotor: Prof. Dr. Alberto Mariotti
Supervisors: Sam Junius and Kevin Turbang

Sciences and Bio-Engineering Sciences

Abstract

In this project, we combine a dark matter minimal model with a stochastic background of gravitational waves to investigate if it is possible to link a GW signal with dark matter production mechanisms. We use a simplified minimal model to describe dark matter where we expand the Standard Model with four new particles and a new gauge $U(1)_D$ symmetry. The two relevant mechanisms to dark matter in the early Universe, UV and IR Freeze-In, are given by one operator which changes during the cosmological evolution when the new gauge symmetry spontaneously breaks and one particle in the operator takes a non-zero vacuum expectation value. If this is a first order phase transition, i.e. if there is a barrier between the true and false vacuum, this can lead to a stochastic background of gravitational waves. In such a phase transition, the field must tunnel from the false to the true vacuum thereby creating nucleation bubbles. These bubbles expand in the plasma and create sound waves in it that lead to the stochastic background. That background could possibly be seen in interferometers such as LISA, BBO and the Einstein Telescope. In the framework of the minimal model, it is investigated if the peak frequency of the GW signal can identify the type of dark matter production mechanism in the early Universe. This will provide a concrete example of the connection between dark matter Freeze-In models and gravitational wave signatures.

This master's thesis came about during the period in which higher education was subjected to a lockdown and protective measures to prevent the spread of the COVID-19 virus. The process of formatting, data collection, the research method and/or other scientific work the thesis involved could therefore not always be carried out in the usual manner. The reader should bear this context in mind when reading this master's thesis, and also in the event that some conclusions are taken on board.

Contents

1 Introduction

This thesis combines two of the most examined topics currently in the world of high-energy physics, namely dark matter and gravitational waves. In particular the main investigation of this thesis will be examining the properties and parameters of a minimal dark matter model and trying to link them to a gravitational wave signal coming from a stochastic background of gravitational waves. Such a background will be created by a first-order phase transition that might be observed in upcoming interferometer experiments like LISA and the Einstein Telescope.

Dark matter is an unknown form of matter that does not interact via the electromagnetic force. Its existence has been confirmed by multiple independent observations. There are multiple ways to describe dark matter, some models use fundamental particles while other models hypothesise dark matter as primordial black holes or other massive objects. In this thesis, a simplified minimal dark matter model is used expanding the Standard Model with four new particles and a new $U(1)$ gauge symmetry. When considering the particle models of dark matter, there exist multiple production paradigms that generate dark matter in the Early Universe. The most researched production regimes for dark matter as fundamental particles are Freeze-Out and Freeze-In production.

In section 2, after a short summary of some important cosmological parameters, we give an overview of the evidence for dark matter, what it could be and what are the relevant Early Universe production mechanisms.

In section 3 and 4, the original investigations of this thesis regarding dark matter production and phenomenology are developed. In section 3, the original dark matter minimal model is introduced which is the one that will be studied for the rest of this thesis. The relevant particles, interactions and parameters of the minimal model are also discussed in this section. For this particular model, two production mechanisms, called UV Freeze-In and IR Freeze-In, will contribute to the dark matter abundance during the cosmological evolution of the Universe. It is possible to describe both production mechanisms using only one operator in the presence of a symmetry that is spontaneously broken by a scalar field that takes a non-vanishing vacuum expectation value. The scale at which this happens is important for the generation of the gravitational wave signal as discussed later on.

In section 4, both dark matter production mechanisms are discussed in detail. The dark matter yield and relic abundance are calculated for different scenarios. There will be an analysis of the yield for different values of parameters in the model leading to various dominating production mechanisms. Depending on the parameters, in one regime, the UV production will be dominant, while in another region of parameter space, the IR production will be dominant. A third possibility is that there is a mixed contribution and that neither production regime is dominating over the other. We will also scan the different parameters to find the regions in the parameter space where the correct relic abundance as observed by Planck, $\Omega h^2 = 0.12$, is recovered. Within this parameter space, we also point to the regions where the different mechanisms dominate the dark matter production.

The next part of the investigation starts with discussing gravitational waves or GW, especially those coming from a stochastic background, or SBGW for short, as a result of a first-order phase transition. Phase transitions happen all the time in our life, one of the most simplest examples is boiling water. However, a phase transition can also have a more exotic source. In the case of the thesis, the phase transition will come from the aforementioned spontaneous symmetry breaking of the new gauge symmetry, i.e. the changing from one vacuum, the false one, to a true vacuum. To describe this phenomenon, we introduce the finite temperature effective potential, which adds one-loop and thermal corrections to the tree-level potential. There exist two types of phase transitions, a first-order phase transition or FOPT and a second-order one. The difference between the two is that in a second-order phase transition, one can just roll smoothly from the false to the true vacuum. In a first-order phase transition, one needs to tunnel between these two vacua. It is the latter process that will be of interest in this thesis since this will result in the creation of gravitational waves. The process of tunneling will create nucleation bubbles in the Early Universe in which the field has tunneled to the true vacuum of the potential. These bubbles, by releasing energy into the plasma around them, can create sound waves in this plasma. These sound waves will then be responsible for the generation of gravitational waves.

In Section 5, we will give a short introduction to gravitational waves as well as introducing the concept of a stochastic background of gravitational waves. After going over the possible sources for such a stochastic background and how to quantify the sensitivity of an interferometer experiment, we will investigate the intricacies of the finite temperature effective potential for a scalar field and also show an example for the Standard Model.

In subsection 5.5, we discuss in detail the difference between a second-order and a first-order phase transition illustrated by a simple toy model for both cases. After that, we examine the tunneling process from the false vacuum to the true vacuum first at zero temperature and after that at finite temperature. Here, the concept of the bounce action will be introduced. The bounce action will lead us to the nucleation condition which helps us in computing the nucleation temperature, the characteristic temperature at which the first-order phase transition happens.

In subsection 5.6, we will introduce the GW spectrum and how to compute it for a first-order phase transition as well as give an overview of the possible sources of a GW spectrum coming from the FOPT. There will be a focus on sound waves generated in the plasma surrounding these bubbles, since this is the relevant production mechanism for a GW signal in the thesis.

Section 6 contains the original investigations for the dark matter minimal model introduced in section 3 regarding the SBGW where we will use the relevant concepts and parameters from section 5 to study the phase transition. However, this study depends on the scale of the problem. Three scales will be chosen corresponding to three possible scenarios for dark matter production, a UV Freeze-In dominated production, IR Freeze-In dominated production and a mixed Freeze-In dark matter production. For each of these scales, a benchmark will be chosen for which the GW spectrum will be computed. In this section, we will also explore the parameter space of the model by examining the properties of the GW spectrum parameters for a varying gauge coupling of the new gauge $U(1)$ symmetry.

Until now, everything has been computed numerically, however in section 6.2, a possible semi-analytical approach to the story of the effective potential and the phase transition is investigated. There, we perform a high T expansion for the thermal part of the effective potential and do a comparison with the full computations for the potential. The high T expansion will be useful to explain when a phase transition is first-order depending on the parameters of the dark matter minimal model.

As a conclusion to the thesis, in section 6.3, there will be a short study of the possible detectability of the GW spectra coming from the first-order phase transitions in the dark matter minimal model whereby the spectra will be compared to the sensitivity curves of experiments. We will find that the GW signal corresponding to the different production mechanisms, UV, IR or mixed Freeze-In contribution, will peak at different frequencies and therefore potentially detectable at different interferometers. This will provide, in a minimal model, an example of an interplay between the dark matter dynamics in the

Early Universe and the expected properties of a corresponding SBGW signature.

In this thesis, natural units are used. That means that

$$c = k_b = \hbar = 1. \tag{1.1}$$

2 Dark Matter

In this section, a small introduction to dark matter physics is given, including existing evidence for dark matter, and basic aspects of the dark matter dynamics in the Early Universe. First of all, some useful parameters, definitions and background information about cosmology will be given. After a small summary of the energy distribution of the Universe, there will be an overview of the experimental evidence of dark matter in section 2.2. One may also wonder what the possible options are that can explain the nature of dark matter, these can be found in section 2.3. As a last part of the intricate dark matter puzzle, we examine how dark matter is produced during the cosmological evolution of the Universe. The production mechanisms of dark matter are investigated in section 2.4.

2.1 Short Introduction to Cosmological Parameters

To begin this introductory section to dark matter, some useful cosmological parameters and definitions will be given which will be important for the calculations and analysis performed in the thesis.

The number density n The evolution of particles can be followed when considering the number density n of such a particle. It is defined as the number of particles N in a certain volume V, $n = N/V$. The number density is useful, because the amount of particles does not change by itself. Interactions with other particles however can change the amount of particles and the number density. When the particles are present in an expanding Universe their number density decreases even if N stays the same, because $V \sim a^3$ increases, with a the scale factor of the Universe which quantifies the expansion of the Universe.

One may ask then when the amount of particles does not change in the Universe. This happens when the particle is in thermal equilibrium meaning that interactions happen in such a way that N is constant. This process is quantified by the equilibrium number density n^{EQ} defined as

$$n^{EQ} = g \int \frac{d^3p}{(2\pi)^3} e^{-m/T} \,, \tag{2.1}$$

where m is the mass of the particle in equilibrium, T is the temperature of the Universe and g is the degeneracy or the degrees of freedom of the particle. The equilibrium density has two asymptotic states as a function of T

$$\begin{aligned} &= g \left(\frac{mT}{2\pi}\right)^{3/2} e^{-m/T} \quad && \text{if } m \gg T \,, \\ &= g\frac{T^3}{\pi^2} && \text{if } m \ll T. \end{aligned} \tag{2.2}$$

If a particle is in thermal equilibrium, its number density is equal to the equilibrium number density. In the limit $m \gg T$, if the particle stays in thermal equilibrium, it becomes Boltzmann suppressed.

The Friedmann equations One can derive the Friedmann equations from the Einstein equations using the Friedmann-Lemaître-Robertson-Walker metric for an expanding Universe [1]. These equations relate the scale factor to the energy-momentum density of the Universe. The first Friedmann equation is given by [1]

$$H^2 = \frac{8\pi G}{3}\rho - \frac{k}{a^2} \,, \tag{2.3}$$

where the Hubble parameter is defined as $H = \dot{a}/a$, $\dot{a} = da/dt$, G is Newton's gravitational constant and k represents the curvature of the Universe. The second Friedmann equation is [1]

$$\frac{\ddot{a}}{a} = -\frac{4\pi G}{3}(\rho + 3p)\,, \tag{2.4}$$

where p is the pressure and $\ddot{a} = d^2a/d^2t$. The energy density in this case is a combination of all the different energy-matter contributions present in the Universe

$$\rho = \rho_R + \rho_m + \rho_k + \rho_\Lambda\,, \tag{2.5}$$

where ρ_R is the radiation contribution, ρ_m is the matter contribution consisting of baryonic matter and dark matter, ρ_k is the curvature contribution and at last, there is the dark energy contribution ρ_Λ. In the cosmological evolution of the Universe, the dominant contribution to the energy density changes from radiation, which dominates after inflation, to matter and eventually to dark energy. In this thesis, all important events happen at a time where the Universe is radiation dominated. When the Universe is radiation dominated, the energy density is given by

$$\rho_R(T) = \frac{\pi^2 g_*^\rho}{30} T^4\,, \tag{2.6}$$

with g_*^ρ the effective number of degrees of freedom for the energy density. If the Universe is flat and has no curvature, k = 0, then the Hubble parameter in a radiation dominated Universe becomes

$$H(T) = \sqrt{\frac{8\pi G \rho_R(T)}{3}} = \frac{1.66\sqrt{g_*^\rho}T^2}{M_{Pl}}\,, \tag{2.7}$$

where the Planck Mass is $M_{Pl} = \sqrt{\frac{1}{8\pi G}}$ = 2.435×10^{18} GeV.

Temperature of reheating T_{re} The Universe can go through multiple stages in its evolution. One is the aforementioned radiation dominated stage. Before that stage, the Universe is dominated by the inflaton during the inflation phase of the Universe [2]. Not much is known about this phase of the Universe yet. However, the precise dynamics of inflation are not so relevant to the work done here and hence are not discussed. The inflation phase of the Universe comes to an end when the inflaton decays into the particles of the Universe thereby starting the process of reheating [3]. In this thesis, it is assumed that reheating takes place at one specific moment in time, i.e. at a fixed temperature called the temperature of reheating T_{re}. It is possible to introduce more complex procedures of reheating spanning multiple moments in the cosmological evolution. However, this is beyond the scope of this thesis and will also not have a significant impact on the results. After reheating, the Universe will be radiation dominated for all moments relevant to the subject of this thesis.

The expansion rate H_0 The Hubble constant H_0 gives information about the current expansion rate of the Universe. Disregarding the current discrepancy between the different measurements of this constant one can define

$$H_0 = 100\, h\, km\, s^{-1}\, Mpc^{-1}\,, \tag{2.8}$$

where h encapsulates the result of the measurement. In this thesis the Planck results are followed, hence $h \sim 0.67$ [4]. The smaller the value of h, the slower the Universe is expanding.

Yield Y Due to the expansion of the Universe, the number density $n = N/V$ will drop even if the amount of particles N stays the same. Therefore it is useful to define a quantity that is not affected by this expansion. Starting from the number density of dark matter, it is possible to define the comoving number density or yield $Y = n/S$, where

$$S = \frac{2\pi^2}{45} g_*^S T^3 \tag{2.9}$$

is the entropy and g_*^S is the effective number of degrees of freedom for the entropy. The yield stays the same even for an expanding Universe if the amount of particles N does not change.

Density parameter Ω This parameter specifies the density of a certain component, which could be any energy or matter distribution, in the Universe. It is defined as

$$\Omega = \frac{\rho}{\rho_c}, \tag{2.10}$$

where

$$\rho_c = 3H(t)^2/8\pi G, \tag{2.11}$$

is the critical density, defined as the density for an Universe which is flat, or in other words where the curvature k is zero, see Eq.(2.3). The density parameter is a function of time and the present value of the parameter is denoted as Ω_0.

One can rewrite the first Friedmann equation using the density parameter as

$$\Omega - 1 = \frac{k}{H^2 a^2}, \tag{2.12}$$

where the concept of the critical density becomes clearer since it is that density where Ω = 1. It is possible to find an equation for the relic abundance for dark matter χ as a function of the final yield

$$\Omega_\chi h^2 = \frac{16\pi^3 G}{135\epsilon^2} g_S T_0^3 m_\chi Y_\chi^\infty = 0.14 \frac{m_\chi}{1GeV} \frac{g_S}{100} \frac{Y_\chi^\infty}{2\times 10^{-11}}, \tag{2.13}$$

where Y_χ^∞ can come from any of the dark matter production mechanisms, $T_0 = 2.725\,K$ is the current temperature of the Universe, m_χ is the mass of the dark matter particle and $\epsilon = 2.131 \times 10^{-42}$ GeV.

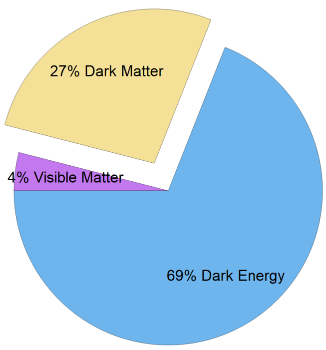

Figure 2.1: The energy-matter distribution of the Universe. The highlighted part represents the dark matter density consisting of 27 % of the complete energy-matter distribution of the Universe [5].

It is observed that the Universe consists of around 69% dark energy, 4% visible matter and 27% dark matter [5], as shown in the pie chart in Figure 2.1. This experimental knowledge of dark matter comes from observations of the CMB by WMAP [6] and more recently by Planck [7]. These experiments give a constraint for the dark matter relic abundance $\Omega_\chi h^2$ = 0.12, which has to be accounted for when building dark matter models.

This project will not talk about the intricate mysteries of dark energy or about the well-known world of baryonic matter. The interests of this thesis lay in the discussion of dark matter and its properties. In the next section, we will give a short summary of the evidence around us in the Universe for this hypothetical form of matter. It seems to only interact gravitationally with other particles. Possibly, it could also interact via an unknown dark force. After that, we will look at what this dark matter can be and the possible proposed production mechanisms in the Early Universe for it.

2.2 Evidence for Dark Matter

The main evidence for dark matter comes from observing the Universe, both in and outside the Milky Way. Dark matter does not interact via the electromagnetic force and only seems to interact with the Standard Model or SM via the gravitational force or other unknown dark forces. It is seen as a hidden, meaning not visible, kind of matter. By observing motion in space, ranging from stars to galaxies, it is possible to find evidence for the existence of dark matter by calculating the expected gravitational forces only considering the visible matter. If these calculations do not agree with the observations of these motions, it is possible to attribute the discrepancy to the presence of dark matter. We will list some of the evidence in this section [8].

Rotation velocity curve One of the most famous examples of evidence for dark matter are the rotation velocity curves of galaxies. These curves show the velocity of matter rotating in a spiral disk as a function of the radius from the center of the galaxy in which they are rotating. To compute such a curve, the laws of Newton can be used. Take a galaxy with a mass $M(R)$ within the radius R, then the balance between the centrifugal force and the gravitational force demands that the velocity of a moving object at a radius R obeys

$$\frac{v^2}{R} = \frac{GM(R)}{R^2}, \tag{2.14}$$

or

$$v = \sqrt{\frac{GM(R)}{R}}. \tag{2.15}$$

At large distances, when all the visible mass is enclosed in the radius R, the velocity should drop off via $v \sim \sqrt{1/R}$. However, when the velocity is measured at these larger distances, this specific behaviour is not found as shown in Figure 2.2. It is observed that the velocity stays rather constant at larger distances. This is only possible if there is additional dark mass at the outer regions of the galaxy which cannot be observed directly. This extra mass would lead to an extra gravitational effect on the rotation velocity curves making them constant. Therefore, these galaxy rotation curves are one indication for the existence of dark matter.

The hot gas in galaxy clusters The gas in a cluster is heated by falling into the gravitational well of the cluster. However, the self-gravity of the gas does not produce enough attraction to counteract the outgoing pressure due to the high temperature of the gas, thereby leading to the conclusion that the gas should not fall into the cluster.

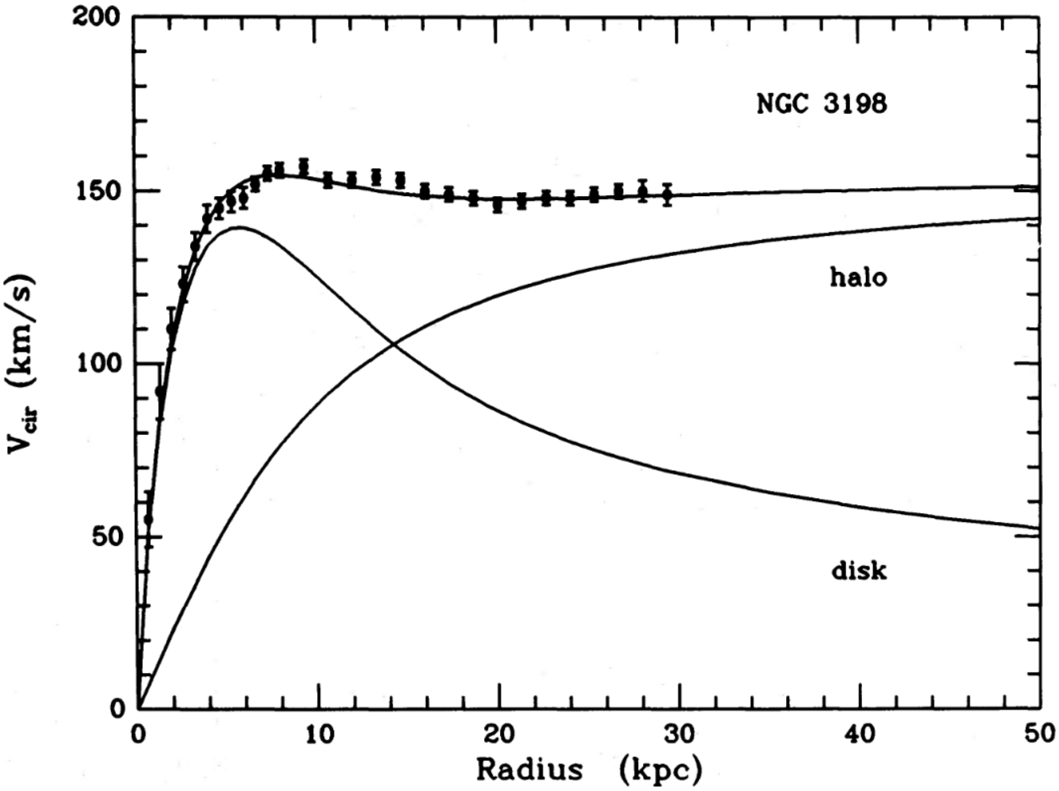

Figure 2.2: The observed rotation velocity curve from the spiral galaxy NGC3198 is shown together with a possible dark matter halo profile and the disk profile where mostly visible matter resides. As stated in the text, it is seen in the figure that the velocity stays rather constant at higher radii outside the visible part of the galaxy. This is not in accordance with the observed amount of visible matter in this galaxy and therefore implies the existence of extra, dark matter distributed in a halo profile. Figure taken from [9].

However, we can observe that it does. Hence, this can be seen as another indication for the existence of dark matter, because the dark matter would create an additional gravitational effect pulling the gas towards the center of the cluster [10].

Gravitational lensing Gravitational lensing happens when a massive object present in space bends the light coming from behind it. This happens because the curvature of space near a mass deflects these passing rays of lights. The bending will give a deformed image of the light when observed on Earth. The amount of deformation depends on the mass of the massive object, therefore it is possible to determine the mass of the object. It seems like the light is bent more than we would expect when only looking at the amount of visible matter, hence this is also an indication for the existence of dark matter [11].

Bullet Cluster The Bullet Cluster is the result of the collision of two smaller clusters. In theory, since dark matter does not interact electromagnetically, it should flow further through the other cluster without any friction, while the visible sector should feel friction and it cannot flow as far as dark matter. Hence, there will be a slight difference in the distribution of the two masses in the Bullet Cluster. The baryonic matter will be concentrated more in the center, while dark matter would be more present in the outer layers. This is confirmed by using observations of gravitational lensing [12].

CMB The CMB or Cosmic Microwave Background radiation is a relic of the Early Universe. The CMB came to life when recombination happened in the Early Universe and photons were allowed to travel freely because there are no longer hindered by interactions with electrons which have bonded with protons to form hydrogen atoms. It is a stochastic background of radiation with a spectrum of small temperature anisotropies. The power spectrum of these anisotropies is the best known observable of the CMB. From this power spectrum, it is possible to get information about the amount of dark matter in the Universe.

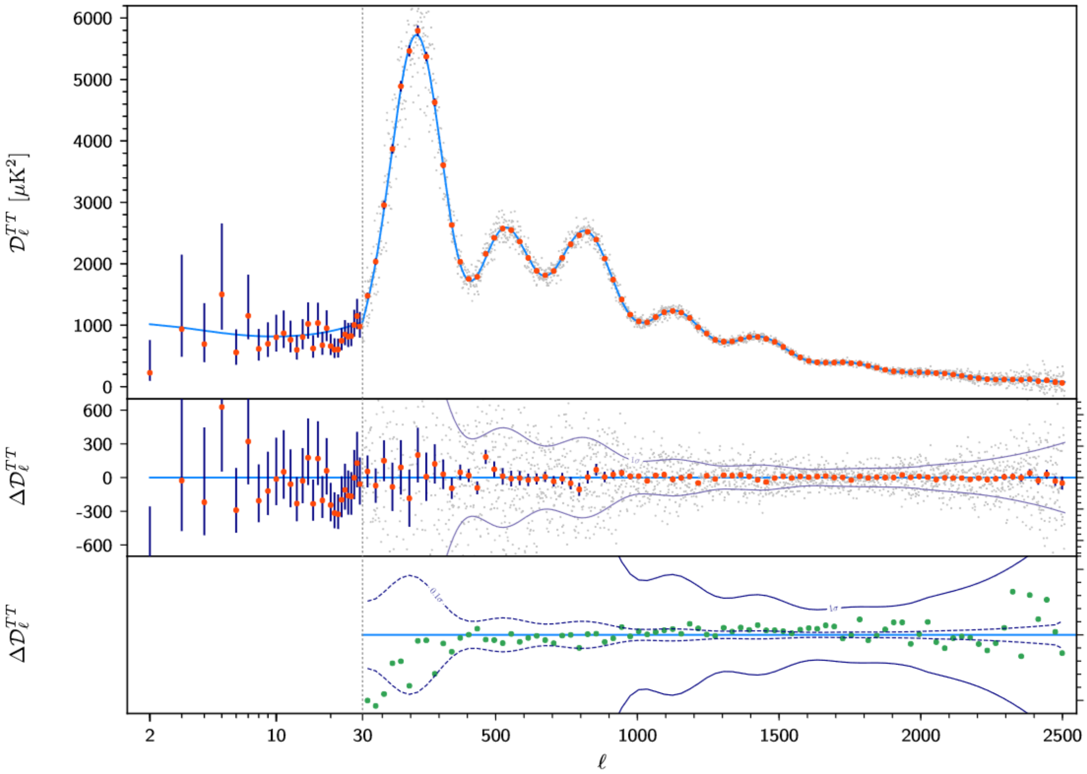

Figure 2.3: This plot shows the results of the Planck 2018 data. We only focus on the first plot, which shows the power spectrum for the CMB. In the plot, the peaks of the spectrum mentioned in the text are clearly visible. It is then when examining the relative and absolute value of these peaks that it is possible to deduce information about dark matter. Figure taken from [13].

We give the results of the Planck Collaboration in Figure 2.3 [13]. We will not go into the details of the peaks in the power spectrum from the CMB that give information about the abundance of dark matter. One only needs to know that the relative and absolute height of the peaks cannot be explained without the presence of dark matter.

2.3 What can Dark Matter be?

Dark matter is responsible for about a fourth of the energy-mass distribution of the Universe. Hence it is important to investigate and find ideas to explain its presence. The possible explanations of dark matter can roughly be put into two main classes: a (new) particle or some compact object [8]. A suitable particle candidate for dark matter should be electromagnetically neutral, stable and cannot decay, as it would otherwise not be present anymore.

Already known particles The only possibility in the group of Standard Model particles are neutrinos. Other particles interact via the electromagnetic force such that they can be observed and are almost by definition not dark or are not stable. The neutrino on the contrary is almost massless and interacts very weakly with other particles. However, the SM neutrinos are hot dark matter and also too light to account for all the dark matter in the Universe. Hot dark matter refers to particles, such as neutrinos, which are travelling at relativistic velocities. This has an effect on the structure formation in the Universe [14]. If dark matter would be mostly hot, the structures of the Universe would be different. Results have given constraints on the mass of such hot dark matter where it is required that $m_\chi > 0.5$ keV [15]. Therefore neutrinos are excluded, because their mass is too small, for example there is a bound on the mass of the electron anti-neutrino of $m_{\bar{\nu}_e} < 0.8$ eV [16].

Unknown elementary particles It is possible to introduce one or more particles and add them to the SM to account for dark matter. One example is adding a sterile neutrino [17] or an axion [18]. Another example is looking at supersymmetry and taking the lightest possible supersymmetric particle, the neutralino, as a possible candidate for the dark matter particle.

Compact Objects Possible compact objects are for example Primordial Black Holes which are formed in the Early Universe. They could account for all the dark matter, but are not yet discovered. Another example are so called MACHO's or MAssive Compact Halo Objects. They are proposed to be objects like for example brown dwarfs. However it seems that they cannot account for all the dark matter in the Universe [19].

2.4 Dark Matter production mechanisms

In this section, we will talk about the two leading production mechanisms for dark matter particles during the Early Universe. These are the Freeze-Out and the Freeze-In production mechanisms. The Freeze-Out mechanism involves couplings and interactions whose strength is comparable to the weak interaction of the Standard Model. Particles that undergo this mechanism are WIMPs or Weakly Interacting Massive Particles. However, this kind of production mechanism is falling slightly out of favour due to experimental constraints even though it has not been completely ruled out yet [20, 21]. Instead, in the Freeze-In case the couplings and interactions have a very weak or feeble strength, much smaller than in the Freeze-Out mechanism. The particles that experience the Freeze-In mechanism are FIMPs or Feebly Interacting Massive Particles. The Freeze-In production will be the main focus of the thesis, but it will not hurt to compare these two mechanisms and explain the differences between them [22, 23].

2.4.1 Freeze-Out

The concept for Freeze-Out production of dark matter is as follows [24]. In the Early Universe, right after inflation ends and the Universe is reheated, it is assumed that there is an existing abundance of dark matter. This abundance is in thermal equilibrium with the thermal bath. The thermal bath fills the very Early Universe and consists of a plasma of particles interacting at a constant temperature. To be part of the thermal bath, the dark matter needs to be able to interact with the SM particles via some force mediated by another possibly new particle, an example of such an interaction is shown in Figure 2.4. Dark matter particles that undergo the Freeze-Out mechanism are called Weakly Interacting Massive Particles or WIMPs.

The strength of interactions in the thermal bath is very high such that the density of the particles in the bath is consistent with the equilibrium density. A particle is in thermal equilibrium with the bath as long as the interaction rate Γ is higher than the expansion rate H of the Universe meaning that the interactions that keep the particle in equilibrium are happening faster than the expansion of the Universe.

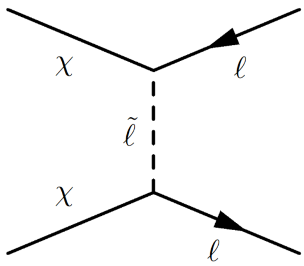

Figure 2.4: An example of a possible Feynman diagram for the Freeze-Out mechanism. It is a two-by-two scattering process. The dark matter particle is represented by χ, the mediator which might be a new particle as $\tilde{\ell}$ and the resulting leptons are given by ℓ.

The Universe expands faster and faster throughout time making it more difficult for dark matter to stay in thermal equilibrium with the bath. At some point $H > \Gamma$ and the interaction will not happen anymore fast enough to make sure that the number density of dark matter follows the equilibrium density. This process is called Freeze-Out, since the dark matter will be frozen-out away from the equilibrium density. Once the particle is frozen-out, its yield stays the same for the rest of the evolution of the Universe if it is a stable particle, which is required for a dark matter particle.

By investigating the Boltzmann equation, see appendix A.1 for more details, it is possible to calculate the number density of dark matter for the Freeze-Out production mechanism

$$a^{-3}\frac{d(n_\chi a^3)}{dt} = \langle\sigma v\rangle \left(\left(n_\chi^{EQ}\right)^2 - n_\chi^2\right) , \tag{2.16}$$

where we have the scale factor of the Universe a, n_χ is the number density of the dark matter, $\langle\sigma v\rangle$ is the thermally averaged cross section as defined in Eq.(A.9) and n_χ^{EQ} is the equilibrium density for dark matter.

This can be rewritten in terms of the yield $Y = n_\chi/S$

$$\frac{dY}{dT} = -S(T)\frac{\langle\sigma v\rangle}{H(T)T}\left(Y_{EQ}^2 - Y^2\right) , \tag{2.17}$$

where $S(T)$ is the entropy, Y_{EQ} is the equilibrium yield and T is introduced as the new time variable via $\dot{T} \sim -HT$. This equation also shows more clearly the interplay between the interaction rate $\Gamma \sim n\,\langle\sigma v\rangle$ and the expansion rate H, since they appear as a ratio.

To get the correct relic abundance for dark matter, the coupling of the interaction in the Freeze-Out case should be approximately 0.5, depending on the mass of the dark matter. This will be different in the Freeze-In case. If $m_\chi \sim 100\,\text{GeV}$ and an interaction cross section around the order of magnitude of that of the electroweak interaction is taken, then the WIMP miracle is recovered. This miracle is the interesting result that the correct relic abundance is achieved when considering the cross section of a weakly interacting particle with a mass around the same order of magnitude of already known heavy particles such as the W boson. The relic abundance in this case would be [25]

$$\Omega h^2 = 0.3\left(\frac{x_f}{10}\right)\left(\frac{g_S}{100}\right)^{1/2}\frac{10^{-39}\ \text{cm}^2}{\langle\sigma v\rangle} , \tag{2.18}$$

where 10^{-39} cm^2 is a typical cross section for a weak interaction and $x_f = m_\chi/T_f$ is the moment of freeze-out. This shows explicitly the WIMP miracle where the correct relic abundance, around Ωh^2 =0.12 is recovered for a WIMP particle. Since Freeze-Out is not the focus of this thesis, more details of the paradigm will not be investigated in this case.

2.4.2 IR Freeze-In

The second possible production mechanism for dark matter particles in the Early Universe is the Freeze-In paradigm. Contrary to Freeze-Out, the dark matter particle in Freeze-In is always out of thermal equilibrium with the thermal bath. In other words, in the Freeze-In regime the coupling of dark matter to the thermal bath is assumed to be so feeble that dark matter is thermally decoupled. In this scenario, the dark matter is created by the decay of another particle which is called the mediator that is in thermal equilibrium with the bath particles. This mediator can be a Standard Model particle or it could also be a new particle. A second fundamental part of the Freeze-In paradigm is that we assume that there is no dark matter coming from the inflaton decay, so that the dark matter abundance right after reheating is approximately zero. Dark matter will all be created by the decay of the mediator.

The mediator will decay into the dark matter particle and some other (SM) particle(s). In the Freeze-In production regime, the coupling of the interaction must be a lot smaller than in the Freeze-Out regime to get the correct relic abundance. The coupling here will be of the order of magnitude 10^{-11}, hence the coupling strength is feeble. If the coupling would be higher, then the dark matter would come into thermal equilibrium with the bath and therefore we would be back in the Freeze-Out case. In the common Freeze-In case, the decay of the mediator is described by the following operator and relevant process

$$\mathcal{L} \supset \lambda\, B_1 B_2\, \chi \quad \Longrightarrow \quad B_1 \to B_2\, \chi\,, \tag{2.19}$$

where $\lambda \sim 10^{-11}$ is the small coupling, B_1 is the mediator which is a bath particle, B_2 is another bath particle and χ is the dark matter particle. These bath particles are assumed to be in thermal equilibrium and therefore are Maxwell-Boltzmann distributed, meaning that the phase space distribution functions of these particles are given by $f_i \approx e^{-E_i/T}$. In the Freeze-In regime, the small coupling is assumed to exist. In this thesis, we will try to come forth with a physics explanation for the smallness of the coupling.

The dark matter particles are created steadily as long as the mediator is abundantly present. The number density of the mediator will eventually be negligible compared to the dark matter density due to Boltzmann suppression and there will be no longer a significant contribution to the dark matter density coming from this decay. The dark matter yield will stay constant from that point on. Most of the dark matter in the Freeze-In regime will be produced at $T \sim m_{B_1}$, hence at lower temperatures, thereby coining the name IR Freeze-In production.

We can examine the (simplified) Boltzmann equation for the decay process in Eq.(2.19)

$$\dot{n}_\chi + 3Hn_\chi = g_{B_1} \int \frac{d^3p_{B_1}}{(2\pi)^3 2E_{B_1}} \frac{\Gamma_{B_1} f_{B_1}}{\gamma_{B_1}}, \tag{2.20}$$

with g_{B_1} the degrees of freedom of particle B_1, $\gamma_{B_1} = E_{B_1}/m_{B_1}$, where E_{B_1} is the energy of the mediator and m_{B_1} is its mass. The decay rate Γ_{B_1} corresponds to the decay from Eq.(2.19). The Boltzmann equation can then be rewritten into

$$\dot{n}_\chi + 3Hn_\chi = a^{-3}\frac{d(n_\chi a^3)}{dt} = g_{B_1}\Gamma_{B_1}\left\langle \frac{1}{\gamma_{B_1}} \right\rangle n_{B_1}^{EQ}, \tag{2.21}$$

where

$$\left\langle \frac{1}{\gamma_{B_1}} \right\rangle = \frac{\int \frac{d^3p}{(2\pi)^3 2E_{B_1}} f_{B_1} \frac{1}{\gamma_{B_1}}}{\int \frac{d^3p}{(2\pi)^3} f_{B_1}^{EQ}} = \frac{\int \frac{d^3p}{(2\pi)^3 2E_{B_1}} f_{B_1} \frac{1}{\gamma_{B_1}}}{n_{B_1}^{EQ}} \tag{2.22}$$

is the thermally averaged Lorentz factor and

$$n_{B_1}^{EQ} = \int \frac{d^3p}{(2\pi)^3} f_{B_1}^{EQ} , \tag{2.23}$$

is the equilibrium number density. It is possible to take Γ and $\langle 1/\gamma_{B_1} \rangle$ together to define the thermally averaged decay rate in analogy to the thermally averaged cross section.

Again investigating Eq.(2.21), it is seen that it is analogous to Eq.(2.16). On the left side, there is the time derivative of the number density, while the right hand side of the equation consists of a thermally averaged object and the equilibrium number density. In the Freeze-Out case, we are looking at a scattering process therefore it is the thermally averaged cross section that is important, while in the Freeze-In, a decay is investigated, therefore the thermally averaged decay rate is important. It can be computed that this particular Boltzmann equation leads to the following yield $Y = n_\chi / S$ for dark matter

$$Y_\infty^{IR} = \frac{135\, g_{B_1}\, M_{Pl}}{8\pi^3 (1.66) g_*^S \sqrt{g_*^\rho}} \left(\frac{\Gamma_{B_1}}{m_{B_1}^2} \right) , \tag{2.24}$$

To derive this yield, the integral over momentum space is converted to one over energy and then carried out

$$\begin{aligned} \dot{n}_\chi + 3 n_\chi H &= g_{B_1} \int \frac{d^3 p_{B_1}}{(2\pi)^3} \frac{f_{B_1} \Gamma_{B_1}}{\gamma_{B_1}} , \\ &= g_{B_1} \int_{m_{B_1}}^{\infty} dE_{B_1} \frac{m_{B_1} \Gamma_{B_1}}{2\pi^2} \left(E_{B_1}^2 - m_{B_1}^2 \right)^{1/2} e^{-E_{B_1}/T} , \\ &= \frac{g_{B_1} m_{B_1}^2 \Gamma_{B_1}}{2\pi^2} T K_1 \left(m_{B_1}/T \right) , \end{aligned}$$

where K_1 is the first modified Bessel function of the second kind. Again changing the number density to the yield $Y = n_\chi / S$ and changing the integration variable twice, once from t to T via $\dot{T} \approx -HT$

$$Y_{IR} \approx \int_{T_{\min}}^{T_{\max}} \frac{g_{B_1} m_{B_1}^2 \Gamma_{B_1}}{2\pi^2} \frac{K_1 \left(m_{B_1}/T \right)}{SH} dT, \tag{2.25}$$

then another time from T to $x = m_{B_1}/T$

$$Y_{IR} \approx \frac{45}{(1.66) 4\pi^4} \frac{g_{B_1} M_{Pl} \Gamma_{B_1}}{m_{B_1}^2 g_*^S \sqrt{g_*^\rho}} \int_{x_{\min}}^{x_{\max}} K_1(x) x^3 dx , \tag{2.26}$$

where we filled in S, see Eq.(2.9), and H, see Eq.(2.7). The integral over x can be analytically performed using the bounds $x_{min} = 0$ and $x_{max} = \infty$. The result is $3\pi/2$, leading to Eq.(2.24). These boundaries are approximations from the real boundaries, however one can only find an analytical expression for the yield if these boundaries are chosen. This is not an out of nowhere approximation, since $x_{max} = m_{B_1}/T_0$ is anyway close to ∞ because T_0 is close to zero. The other boundary of the integral is also an approximation. However since it is assumed that $T_{min} \gg m_{B_1}$, this is reasonable, if one takes into account that most IR Freeze-In dark matter production happens at $T \sim m_{B_1}$.

In Figure 2.5, there is a comparison given between the evolution of the yields in the Freeze-In and Freeze-Out case. In the beginning, the Freeze-Out yield follows the equilibrium density, since the dark matter is in thermal equilibrium until the dark matter is frozen-out. From that moment on, the yield stays constant. One can examine Eq.(2.17) to get an idea why this happens. There we see the interplay between the ratio of the interaction rate $\langle \sigma v \rangle n$ and the Hubble rate H and the difference between Y^2 and Y_{EQ}^2. If the ratio of the rates is large as it is at high temperature, then Y_χ will want to keep close to Y_{EQ}, hence the Freeze-Out yield follows the equilibrium density. At a certain point, the ratio of the rates will become smaller when the temperature decreases and the interaction rate cannot keep up with the expansion rate of the Universe anymore. From then on, Y will go away from Y_{EQ} and the dark matter will freeze-out.

There are three coloured full lines in the Freeze-Out case. These lines represent a different coupling strength. The direction of the arrow indicates an increasing coupling. A bigger coupling strength in the Freeze-Out case results in a bigger thermally averaged cross section, hence the interaction rate can keep up longer with the expansion rate. That means the moment of Freeze-Out will happen later and the yield will follow the equilibrium density longer, such that the final density is lower as indicated in the plot by the arrow.

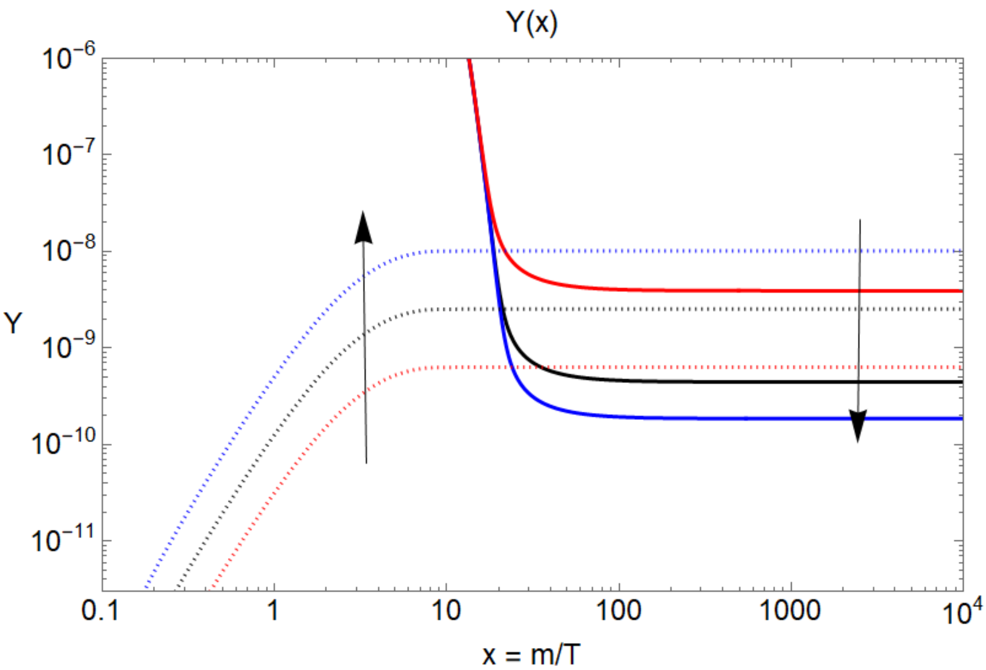

Figure 2.5: A comparison between the yield as a function of $x = m_{\tilde{\ell}}/T$ for the Freeze-Out case is plotted here, shown as a full line, and the Freeze-In case, shown as a dotted line. The different colours account for different coupling strengths. The arrows show increasing values of the coupling for both cases. As seen these arrows are in an opposite direction to each other, indicating a different effect on the yield for the different procedures if the coupling changes.

In the plot, there are also three different dotted coloured lines shown for the IR Freeze-In yield. The Freeze-In yield does not exist at first and then rises until it also becomes constant, when the mediator is no longer significantly present in the Universe. Since this is a logarithmic plot, we observe that the most significant contribution to the dark matter yield in this production regime is for low temperatures close to the mass of the mediator m_{B_1}. This is the reason why this particular type of Freeze-In production is also called IR Freeze-In as mentioned before. This will be the opposite of the temperature properties of the Freeze-In production mechanism examined in the following section, namely UV Freeze-In. The three different colours correspond to an increasing coupling strength. However, an increased coupling strength in the Freeze-In regime will give a larger decay rate, hence a larger yield for the dark matter, see Eq.(2.24). The increase in coupling strength indicated by the arrow is therefore in the opposite direction than for Freeze-Out.

Until now, the more common case for Freeze-In production, IR Freeze-In, with renormalisable operators was discussed. However there exists another type of Freeze-In production which is UV Freeze-In production that utilises non-renormalisable operators. The reason this is called UV will become clear later on in Section 3.2.

2.4.3 UV Freeze-In

The second type of Freeze-In production regime for dark matter we will explore in this thesis is the UV Freeze-In production mechanism. In analogy with the IR Freeze-In discussed in the previous section, in UV Freeze-In the dark matter particle is thermally decoupled from the Standard Model. However, differently than in IR Freeze-In, the feeble coupling of dark matter with the thermal bath is encoded in an higher-dimensional operator and dark matter is produced through scattering and not through the decay of the mediator.

In general, in the UV Freeze-In paradigm, dark matter is coupled to the thermal bath with a non-renormalisable higher-dimensional operator like [22]

$$\mathcal{L}_{HDO} = \frac{\alpha}{M^n}\left(\varphi_1\varphi_2\ldots\varphi_n\right)\chi\psi_1\psi_2\,, \tag{2.27}$$

where α is an order 1 coupling, χ is the dark matter, ψ_1 and ψ_2 are two fermionic bath states and φ_i is a Higgs-like state which is assumed to be in thermal equilibrium. One can take n = 1 with one Higgs-like state. The following operator can then be written down

$$\mathcal{L}_{HDO} = \frac{\alpha}{M}\varphi\chi\psi_1\psi_2, \tag{2.28}$$

where M is the high scale characterizing the higher-dimensional operator assumed to be larger than the temperature of reheating. A contribution to the dark matter yield will come from the non-renormalisable operator via a four-particle interaction such as $\psi_1\varphi \to \chi\psi_2$. This contribution is dominated by high temperatures, depending on parameters such as the reheating temperature T_{re}.

One can investigate what is the contribution of this process to the dark matter production by utilising the following Boltzmann equation

$$\begin{aligned}\dot{n}_\chi + 3Hn_\chi = \int \mathrm{d}\Pi_\varphi \mathrm{d}\Pi_{\psi_1}\, \mathrm{d}\Pi_{\psi_2}\, \mathrm{d}\Pi_\chi (2\pi)^4\delta^{(4)}\left(p_{\psi_1} + p_\varphi - p_{\psi_2} - p_\chi\right) \\ \times\left[|\mathcal{M}|^2_{\varphi\psi_1\to\chi\psi_2} f_\varphi f_{\psi_1} - |\mathcal{M}|^2_{\chi\psi_2\to\varphi\psi_1} f_\chi f_{\psi_2}\right]\,,\end{aligned} \tag{2.29}$$

where $d\Pi_i = \frac{d^3p_i}{(2\pi)^3}\frac{1}{2E_i}$ and f_i is the distribution function for a given state. It is assumed that all states except dark matter are in thermal equilibrium and are Maxwell-Boltzmann distributed such that $f_i \approx e^{-E_i/T}$. Since it is assumed to be out-of-equilibrium, the dark matter has a temperature $T \backsimeq 0$, implying that $f_\chi \backsimeq 0$, such that the initial dark matter number density is $n_\chi \backsimeq 0$, because

$$n_\chi = \frac{g_i}{2\pi^3}\int d^3p f_\chi\,, \tag{2.30}$$

as is required for Freeze-In. As a result the latter term in the Boltzmann equation Eq.(2.29) can be neglected. The Boltzmann equation can be rewritten as [22, 26]

$$\dot{n}_\chi + 3n_\chi H \approx \frac{T}{2048\pi^6}\int ds d\Omega\, \sqrt{s}\, |M|^2_{\varphi\psi_1\to\chi\psi_2} K_1(\sqrt{s}/T)\,, \tag{2.31}$$

where s is the center of mass energy of the interaction at a temperature T and the masses of the relevant particles are assumed to be negligible compared to the temperature at which we are working. In this approximation the Feynman amplitude of a scattering process from the dimension five operator is $|M|^2_{\varphi\psi_1\to\chi\psi_2}=\alpha^2 s/M^2$, see [22], such that

$$\dot{n}_\chi + 3n_\chi H \approx \frac{T\alpha^2}{512\pi^5 M^2}\int_0^\infty ds s^{3/2} K_1(\sqrt{s}/T). \tag{2.32}$$

Using the definition $Y = n_\chi/S$, switching variables from t to T and performing the integral over s, it is found that

$$\frac{dY_{UV}}{dT} \approx -\frac{1}{SHT}\frac{T^6\alpha^2}{16\pi^5 M^2}. \tag{2.33}$$

Carrying out the temperature integral from T_{re} until now which is approximated as $T_0 \approx 0$ and filling in S and H gives

$$Y_\infty^{UV} \approx \frac{0.4\, T_{re}\, \alpha^2\, M_{Pl}}{\pi^7 M^2 g_*^S \sqrt{g_*^\rho}}. \tag{2.34}$$

An example for the UV Freeze-In yield compared to the Freeze-Out case is shown in Figure 2.6. The general features of the Freeze-In and Freeze-Out mechanism are visible. The Freeze-Out mechanism was already discussed when studying Figure 2.5. The Freeze-In mechanism on the other hand starts without an existing abundance of dark matter. Specific to the UV Freeze-In mechanism, the yield rises very steeply at around the moment of reheating and stays constant from that point on. The arrow demonstrates the dependence of the UV yield on T_{re}, since the direction of the arrow shows an increasing value for T_{re}. As expected, see Eq.(2.34), a larger value of T_{re} gives a bigger yield. The yield also starts rising at an earlier moment in the evolution of the Universe because T_{re} is bigger, meaning that reheating has happened earlier in the evolution of the Universe and the creation of dark matter can therefore happen at an earlier time and thus higher temperature.

Now that we are more familiar with dark matter, the evidence for its existence, what it could be and the most common production mechanisms for it in a general framework, we want to introduce a model for dark matter and its production. This model will introduce new particles that describe the dark matter as well as a new gauge symmetry which will spontaneously break in the cosmological evolution of the Universe. The interplay between these will ensure that both the IR and UV Freeze-In production mechanism have a role in creating dark matter.

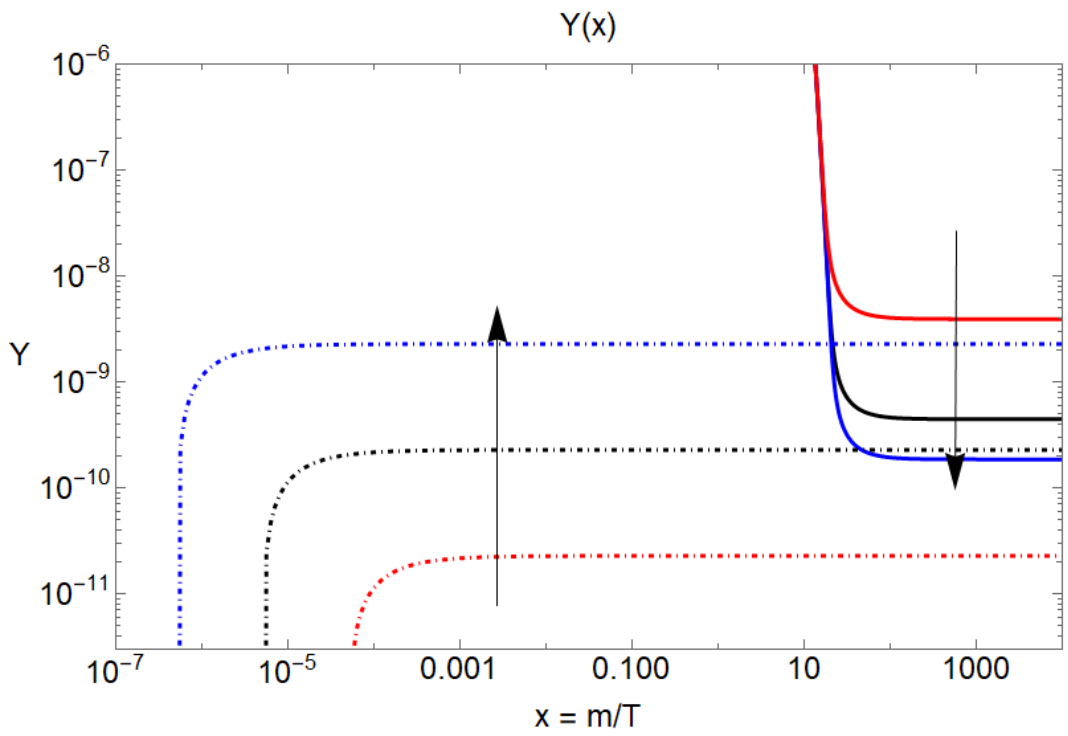

Figure 2.6: The full lines as before are the yields for dark matter created by a Freeze-Out mechanism where the arrow indicates an increasing coupling strength. The dot-dashed lines represent yields coming from UV Freeze-In dark matter production. In this case, the arrow stands for an increasing value of T_{re}.

3 Dark Matter Minimal Model

3.1 Motivation

As mentioned in the previous chapter, a small coupling is required for the IR Freeze-In production mechanism to be valid and to make sure the mechanism can retrieve the correct dark matter relic abundance. We will try to construct a procedure such that this small coupling is not imposed, but is explained dynamically.

Such a small coupling in IR Freeze-In will be achieved by firstly introducing a new higher-dimensional, non-renormalisable operator. The investigated operator is given by

$$\mathcal{L} \supset \frac{\phi}{\Lambda} B_1 B_2 \chi, \tag{3.1}$$

where we used B_1 and B_2 to denote the representations of general bath particles as in Section 2.4, which will be specified when our model is explained in the next section. The dark matter particle is denoted as χ and there is a new massive scalar particle ϕ. The scale Λ represents some unknown degrees of freedom and are only relevant when $T > \Lambda$. The operator has to be UV completed at high temperatures $T > \Lambda$ since the description in Eq.(3.1) is not valid in that regime. From now on, we only consider scenarios where the temperature of reheating in the Universe is always $T_{re} < \Lambda$. Since the operator is higher-dimensional, it is also non-renormalisable. That means that the UV divergences cannot be solved by adding a finite number of counterterms to the Lagrangian.

The second part of achieving the small coupling is utilising the following process. We can assume that during the cooling of the Universe, at a certain temperature T_ϕ, ϕ undergoes a phase transition where it takes a non-zero vacuum expectation value or

VEV v_ϕ and spontaneously symmetry breaking or SSB occurs. This would lead to the following operator

$$\mathcal{L} \supset \frac{v_\phi}{\Lambda} B_1 B_2 \chi, \tag{3.2}$$

where v_ϕ is the VEV of ϕ. This operator is the same as in Eq.(3.1), only at a different regime of the Universe, where ϕ took a VEV. The scale Λ would then be taken high enough such that the coupling of the operator $v_\phi/\Lambda \ll 1$ and the common IR Freeze-In case, see Eq.(2.19), is recovered. The interaction term in Eq.(3.2) is indeed the same as the operator in Eq.(2.19) if we identify λ as v_ϕ/Λ. Hence now, there is a reason for the small coupling to exist. The strength of the interaction is defined by this coupling. Because of the smallness of the coupling, the interaction will be feeble. Thus, in this case, the smallness of the coupling is transferred to the ratio between two scales, v_ϕ and Λ.

This process is analogous to the Froggart-Nielsen mechanism which tries to explain the small Yukawa couplings and the fermion mass hierarchy in the Standard Model. In that mechanism a $U(1)_{FN}$ symmetry is introduced under which the SM fermions and a new scalar are charged. The symmetry is broken and the scalar gets a VEV. Then the small Yukawa couplings are recovered as the ratio between the VEV and a large UV scale. For details on the FN mechanism we refer to [27, 28].

The dynamical generation of the coupling in Eq.(3.2) where a scalar ϕ takes a VEV has two important consequences:

- Firstly, while for a temperature $T < T_\phi$, dark matter is produced through the IR Freeze-In mechanism, at higher temperatures $T > T_\phi$, dark matter is produced by a higher-dimensional operator in Eq.(3.1) that connects it to the thermal bath. This means that the dark matter production in that regime is UV Freeze-In production.

- Secondly, ϕ taking a VEV and the breaking of the symmetry can imply a first-order phase transition in the Early Universe thereby producing gravitational waves as is investigated in the second part of the thesis.

The idea of this thesis is to explore further on these concepts. We explore the phenomenology of the dark matter, the other new particles and the spontaneous symmetry breaking with this new higher-dimensional operator by looking at a minimal model where this happens.

3.2 Concrete realization: a Minimal Dark Matter Model

First of all we start by looking at what new elements are needed to achieve our goal keeping in mind we want to describe the dark matter production via the two new operators given in Eq.(3.1) and Eq.(3.2). These two operators will give rise to two different production regimes of the dark matter, which we will call the UV production and the IR production respectively.

The dark matter minimal model introduced in this thesis will consist of multiple new particles, a new $U(1)_{DARK} = U(1)_D$ symmetry and two different regimes of dark matter production in the Freeze-In paradigm. The effective scale Λ of this theory will be very large, so that we do not have to worry about the high energy implications of the effective operator and a small coupling is recovered as is required in Freeze-In.

New particles Firstly we look at the new particles in the model. Of course we start off with all the Standard Model particles, however we are not able to describe dark matter with already existing SM particles. New exotic particles will be added to the SM in the minimal model to describe it.

- **Dark Matter** χ: The first new particle is the actual dark matter particle χ, which we assume to never be in thermal equilibrium with the thermal bath. This is a prerequisite to work within the Freeze-In paradigm. The small coupling of the interaction makes sure that the dark matter is never in thermal equilibrium with the bath. It is also assumed that this particle is a Majorana fermion.

- **Scalar** ϕ: The second particle we introduce is the scalar ϕ. This particular particle, together with the $U(1)_D$-symmetry under which it is charged will help explaining the small coupling of the model as well as having an impact on the creation of gravitational waves via a first-order phase transition. This will be discussed in section 6. The symmetry will spontaneously break when ϕ takes a VEV. If $T > v_\phi$, then ϕ is a dynamical field where its VEV is equal to zero. However, when $T < v_\phi$, ϕ takes a non-zero VEV. The new symmetry and its SSB are used to achieve the small coupling necessary in Freeze-In production mechanisms via the operator given in Eq.(3.2).

- **Mediator** $\tilde{\ell}$: The third particle a new scalar that is called the mediator $\tilde{\ell}$ [1]. This particle does have the same quantummechanical charges as the right-handed lepton except for the new $U(1)_D$ symmetry under which the mediator will also be charged. The mediator is therefore also connected to the hypercharge symmetry of the Standard Model. It will be especially of importance when looking at the IR Freeze-In production of the dark matter particle. It is actually the decay of the mediator into a lepton and χ which is the dominant dark matter production process in the IR Freeze-In regime. The mediator is the second particle that will be charged under the new symmetry.

New Gauge Symmetry $U(1)_D$ We have mentioned a new symmetry $U(1)_D$ that is added in this minimal model. It would be a gauge symmetry and some of the new particles will be charged under this new symmetry as shown in Table 3.1. There will be no Standard Model particles charged under this new symmetry. Another symmetry we add is a $\mathbb{Z}_2$ symmetry charging χ and the mediator such that the dark matter only interacts with the thermal bath via operator in Eq.(3.4) and Eq.(3.5).

	ϕ	$\tilde{\ell}$	χ
$U(1)_D$	1	-1	0
$\mathbb{Z}_2$	0	-1	-1

Table 3.1: The charges of the new particles under the new gauge symmetry $U(1)_D$ and $\mathbb{Z}_2$ symmetry.

We will charge ϕ under the new symmetry and if we want the Lagrangian, especially the higher-dimensional operator, to be invariant under the new symmetry some of the other particles must also be charged. We chose to charge the mediator under this symmetry, in such a way that the new operator is invariant under this new symmetry. We will chose to give ϕ a charge one under the $U(1)_D$-symmetry in the model, while we give the mediator charge minus one in the model. Since this is a gauge symmetry, we also expect there to be a new gauge boson Z'. Both particles ϕ and Z' have a mass of order v_ϕ. When the temperature drops below $T_\phi \sim v_\phi$, their dynamics will not play any role.

[1]The symbol of the mediator is chosen with supersymmetry or SUSY in mind, however the mediator is not a common SUSY particle and this minimal model is not a SUSY model [29, 30]

In the minimal model, the following terms will be added to the Lagrangian

$$\mathcal{L} \supset |\mathcal{D}_\mu\phi|^2 + |\mathcal{D}_\mu\tilde{\ell}|^2 + \frac{i}{2}\bar{\chi}\not{\partial}\chi + V(\phi) + V(\tilde{\ell}) + \frac{\phi}{\Lambda}\ell\tilde{\ell}\chi - \frac{1}{4}F'_{\mu\nu}F^{\mu\nu\prime}.^2 \tag{3.3}$$

In these terms, we have included a new kind of covariant derivative for ϕ, $\mathcal{D}_\mu = \partial_\mu - ig_D Z'_\mu$ that includes terms with the new gauge boson Z' of the new $U(1)_D$ symmetry. The covariant derivative of the mediator $\tilde{\ell}$ also includes the Z' term, but also a term with hypercharge. We assume that the dark coupling constant g_D is of order 1. Since we do not charge χ under any symmetry, we only wrote the partial derivative in the kinetic term for the dark matter particle. It is not necessary to specify the form of the potential $V(\phi)$ in this section of the thesis, because it does not influence the dark matter production which is the focus point of this part of the thesis. In a later section, when addressing the gravitational wave generation from first order phase transitions, the form of the potential will be specified.

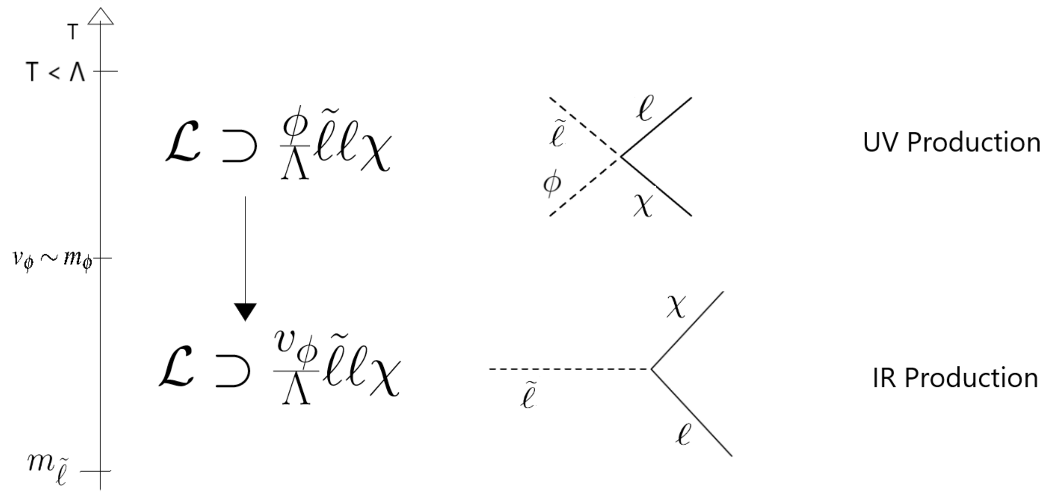

Figure 3.1: This scheme shows the evolution from the dominant operator that is responsible for the dark matter production at that point together with the relevant Feynman diagrams. It also gives an overview of the relevant scales for this production represented on the temperature axis at the left of the scheme. When the temperature goes down during this evolution, the dominant production channel changes. At high temperature, the operator is in the UV Freeze-In regime and that accounts for the dark matter production at high T close to $T_{re} < \Lambda$. Then, at $m_\phi \sim v_\phi$, the $U(1)_D$ symmetry breaks when ϕ takes a VEV v_ϕ. This changes the operator and the IR production regime becomes the dominant dark matter production. It is when $T \sim m_{\tilde{\ell}}$ and the mediator gets Boltzmann suppressed that the dark matter production stops significantly.

Interactions Consider the decay of the inflaton. It is assumed to decay into the visible sector, which does not include the dark matter particle χ, which is the hidden sector. It is also assumed that the decay of the inflaton happens immediately and that there is one temperature T_{re} at which this decay, the process of reheating, happens. In this model, after reheating, there will be a negligible amount of dark matter in the universe. Then, the dark matter in the minimal model can be produced by two main interaction processes.

[2]Here, we neglect possible quartic interactions among the scalars of the dark matter sector and with the Higgs, assuming they are small. The interactions between ϕ and H can introduce mixing in the mass matrix of ϕ and H.

An important assumption from the model is that $T_{re} < \Lambda$, such that the degrees of freedom in the UV completion of our model are never relevant for dark matter production. A schematic overview of these interactions is given in Figure 3.1.

In the following paragraphs, a qualitative discussion of the dark matter production mechanisms which are active during the evolution of the Universe will be given all the way from T_{re} to very low T. A detailed discussion with all the computations and formulas will take place in section 4.

- **UV Production** [31, 32]: The first (and second) possible interaction that creates dark matter in the UV production regime is the annihilation of ϕ and the mediator (or the lepton) which are in thermal equilibrium resulting into the production of χ and the lepton (or the mediator). The third process is when the mediator and the lepton annihilate into ϕ and χ. This is a two-to-two scattering process. This particular interaction happens dominantly in the unbroken phase of the $U(1)_D$ symmetry ranging from T_{re} to v_ϕ. All the particles except χ are in thermal equilibrium.

  The corresponding operator of the dark matter UV Freeze-In production is

  $$\mathcal{L} \supset \frac{\phi}{\Lambda}\tilde{\ell}\ell\chi. \tag{3.4}$$

  This is analogous to Eq.(3.1), but now specified for the concrete model of the thesis. We have replaced the bath particles with the specific particles used in the minimal model. This is a non-renormalizable operator, hence this production channel of dark matter happens primarily at higher temperatures in the evolution of the Early Universe and therefore higher energies. This is the reason why this production is called UV production. Specifically, the UV nomenclature refers to the production of dark matter mainly happening at the highest possible temperature of the Universe, T_{re}. The dark matter UV production happens close to the temperature of reheating such that the yield of dark matter shoots up at temperatures close to T_{re}. After that, there is no more a significant contribution to the yield at lower temperatures coming from this production channel. This also means that the abundance of dark matter Ω_χ, since this follows from the yield, see Eq.(2.13), depends on the value of T_{re}. Since ϕ, ℓ and the mediator are in thermal equilibrium with the bath, we do not have to worry about their number densities decreasing in these processes at the high temperatures $T > m_\phi$ where the UV production happens.

- **IR Production**: The second interaction is the decay of the mediator into a lepton and χ, but it is described by the same operator as in the UV production. The difference is that this interaction happens in the broken phase of the $U(1)_D$ symmetry, ranging from v_ϕ to $m_{\tilde{\ell}}$, where ϕ has taken a VEV, v_ϕ. The broken phase and hence the IR Freeze-In production starts at v_ϕ, the point where the symmetry breaking happens, and ends at $T \sim m_{\tilde{\ell}}$, because at that point, the mediator gets Boltzmann suppressed. In this regime, ϕ has taken on a VEV and therefore ϕ will no longer be relevant for the creation of dark matter. This IR process can be described by the following operator

  $$\mathcal{L} \supset \frac{\phi}{\Lambda}\tilde{\ell}\ell\chi \xrightarrow{\phi \to v_\phi + \delta\phi} \frac{v_\phi}{\Lambda}\tilde{\ell}\ell\chi \left(+\frac{\delta\phi}{\Lambda}\tilde{\ell}\ell\chi\right), \tag{3.5}$$

  with $\delta\phi$ is the dynamical fluctuation of ϕ. This operator is the minimal model form of the more general operator Eq.(3.2). It is also clear now that the UV case happens before the SSB, the unbroken phase, while the IR case is relevant in the broken phase of the symmetry. The second term with the dynamical perturbation $\delta\phi$ will not have a significant contribution to the dark matter production as we explain in appendix A.3. The IR production of dark matter happens at lower temperature and lower energy compared to the UV production. Specifically most of the production will happen around $T \sim m_{\tilde{\ell}}$, which can be seen as the lowest possible temperature for production, hence the name IR production. This is the most standard way of Freeze-In production of dark matter. The IR production is not dependent on the temperature of reheating in contrast to the UV production.

From Eq.(3.5), we can see that the small coupling comes from the ratio of the VEV v_ϕ and Λ. If the scale Λ is then taken to be large, even larger than the temperature of reheating, a small coupling for this particular process will arise and therefore the small coupling that is needed for Freeze-In is explained. The amount of IR Freeze-In production depends on this small coupling.

Parameters of the model The important parameters in the model for dark matter production are Λ, T_{re}, v_ϕ ($\sim m_\phi$) and the masses of both the mediator and χ. Based on different values of these parameters, the dominant production mechanisms of the dark matter will differ, in one part of the parameter space UV production will be dominant, in other parts of this space IR production will be dominant, while in other parts of the parameter space there will be a mixed region of dark matter production where both production mechanisms are relevant.

For example, if we take a large value for the VEV v_ϕ, close to T_{re}, but still $T_{re} > v_\phi$, then the UV production will still occur. However, it is likely that the UV production will not have a significant effect on the relic abundance of dark matter. In that case, the significant contribution to the dark matter relic abundance will come from IR production due to the high value of the VEV, which translate to a bigger coupling v_ϕ/Λ which makes the IR production bigger. To understand the effect that T_{re} and v_ϕ have on the relative dominance of the different dark matter production mechanisms, we refer to the end of section 4.2, where we examine this effect and find an approximated threshold for T_{re} that determines whether the UV or the IR or neither dominate dark matter production.

However, it can also be the other way around. If the VEV is close to the mass of the mediator and therefore small, then the UV contribution will be the dominant one, since the IR production depends on the VEV via the coupling of the relevant IR interaction, see Eq.(3.5). It is also possible that v_ϕ lies somewhere in between T_{re} and $m_{\tilde{\ell}}$. Then, the yield has to be computed to see which contribution is dominant. There is a region of the parameter space where the two contributions are similar. This region is called the mixed region where neither kind of production dominates over the other.

It is then a matter of varying the values of the relevant parameters such that we can get the correct relic abundance of dark matter Ωh^2 = 0.12 in agreement with observations.

4 Analysis of the Dark Matter Minimal Model

We will discuss the two relevant dark matter production mechanisms in this section, UV Freeze-In and IR Freeze-In, for our dark matter minimal model in detail by examining the relevant processes and their corresponding Boltzmann equations. After that, we will compute and investigate the dark matter yield and relic abundance for these production mechanisms and we will examine in what segments of the parameter space which production mechanism is dominant. We start with the UV Freeze-In production.

4.1 UV Production

The UV production channel is described by the operator Eq.(3.4). This leads us to study the three Feynman diagrams that contribute to the creation of dark matter in the UV production, see Figure 4.1, which are two more than the one seen in Figure 3.1 on the top row of the scheme.

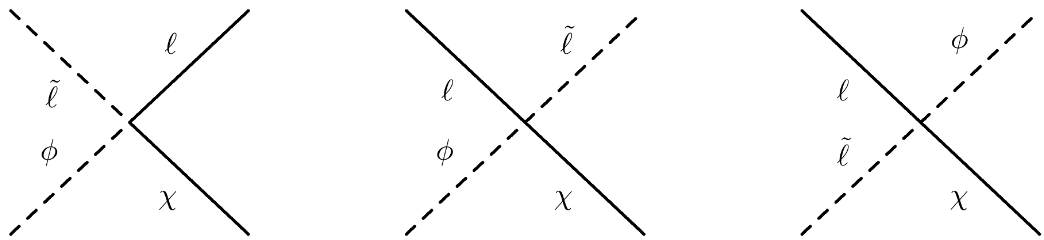

Figure 4.1: These three diagrams show the dominant interactions that will create dark matter in the UV production regime. The first two diagrams on the left define an annihilation of the scalar ϕ and another particle, it could be the lepton or the scalar mediator, which results in the creation of χ and another particle, which could be the mediator or the lepton. The third diagram shows an annihilation of the mediator with a lepton into ϕ and χ.

We want to calculate the yield Y and investigate its time evolution. The relic abundance of dark matter will also be computed to investigate the parameter space of our model and get constraints on some of the values for the parameters by requiring that $\Omega h^2 = 0.12$.

To calculate the number density n_χ and hence the yield Y_χ of dark matter, we need to solve the Boltzmann equation for the three scattering processes relevant for the UV production of dark matter. The equation is given by [31]

$$\begin{aligned} \dot{n}_\chi + 3Hn_\chi = \sum_{i,j,k} \int & \mathrm{d}\Pi_i \mathrm{d}\Pi_j \, \mathrm{d}\Pi_k \, \mathrm{d}\Pi_\chi (2\pi)^4 \delta^{(4)} \left(p_i + p_j - p_k - p_\chi\right) \\ & \times |\mathcal{M}|^2_{ij\to\chi k} f_i f_j \, , \end{aligned} \tag{4.1}$$

where we have already neglected the reverse reaction as already discussed in section 2.4.3. We have also summed over the three possible interactions that contribute to the UV production with $i, j, k \in \{\phi, \tilde{\ell}, \ell\}$. We notice that the right hand side of the Boltzmann equation allows us to treat every process in the sum separately and add them afterwards.

We can therefore start discussing here in detail the first diagram, as shown in Figure 3.1, as an illustration and then we explain how to combine all contributions to the total UV Freeze-In production dark matter yield coming from the three diagrams. It is possible to calculate the Feynman amplitude of the first diagram, see appendix A.2.1. The amplitude is computed to be

$$|\mathcal{M}|^2 = \frac{s}{\Lambda^2} \, , \tag{4.2}$$

where s is the center of mass energy of the interaction and we ignored all the masses of the particles involved.

The part of the Boltzmann equation for the first diagram can then be rewritten as [26]

$$\frac{dY_{\phi\tilde{\ell}\to\ell\chi}}{dT} = -\frac{45 M_{Pl}}{512\, g_S\, \pi^8 (1.66)\sqrt{g^\rho}\Lambda^2 T^5} \int_{m_\phi^2}^{\infty} ds\, d\Omega\, P_{\phi\tilde{\ell}}\, P_{\ell\chi}\, |\mathcal{M}|^2_{\phi\tilde{\ell}\to\ell\chi}\, K_1\left(\frac{\sqrt{s}}{T}\right)/\sqrt{s}\,, \quad (4.3)$$

where K_1 denotes the first modified Bessel function of the second kind. We refer to appendix A.2.1 for more details about the Boltzmann equation in the UV Freeze-In regime. We have defined the Hubble parameter $H(T) = \frac{1.66\sqrt{g^\rho}T^2}{M_{Pl}}$. $P_{1,2}$ is defined as

$$P_{1,2} = \frac{[s-(m_1+m_2)^2]^{\frac{1}{2}}[s-(m_1-m_2)^2]^{\frac{1}{2}}}{2\sqrt{s}}. \quad (4.4)$$

We introduce the yield $Y = \frac{n_\chi}{S}$ with $S = \frac{2\pi^2 g_S T^3}{45}$, the entropy at a given temperature and g_S is the effective number of relativistic (entropy) degrees of freedom. In a normal Standard Model dominated Universe, this value would be 106.75 at the highest temperatures. However since the dark matter minimal model introduces new particles, ϕ, $\tilde{\ell}$ and χ, these relativistic degrees of freedom will also change. In this model it will be equal to 113.75. After filling in both $P_{i,j}$, where it was assumed that $m_\phi \gg$ all other masses, and performing the integral over $d\Omega$, the Boltzmann equation is again rewritten to

$$\frac{dY_{\phi\tilde{\ell}\to\ell\chi}}{dT} = -\frac{45\, M_{Pl}}{512\, g_S \pi^7\, (1.66)\sqrt{g_\rho}\Lambda^2}\frac{I(T)}{T^5}\,, \quad (4.5)$$

with

$$I(T) = \int_{m_\phi^2}^{\infty} ds\, [s-m_\phi^2]\, s^{1/2}\, K_1\left(\frac{\sqrt{s}}{T}\right). \quad (4.6)$$

The yield will be computed numerically using *Mathematica*. To simplify the numerical calculations, it is possible to manipulate the Boltzmann equation even more by introducing the coordinates $z = \frac{s}{m_\phi^2}$ and $y = \frac{T}{m_\phi}$. That leads to

$$\frac{I(T)}{T^5} = I(y) = \frac{1}{y^5}\int_1^\infty dz\, (z-1)\, \sqrt{z}\, K_1\left(\frac{\sqrt{z}}{y}\right)\,, \quad (4.7)$$

and

$$\frac{dY_{\phi\tilde{\ell}\to\ell\chi}}{dy} = -\frac{45\, m_\phi}{512 g_S \pi^7 1.66\sqrt{g_\rho}\Lambda}\,\frac{M_{Pl}}{\Lambda} I(y)\,, \quad (4.8)$$

for the rewritten Boltzmann equation. Therefore the only dependence of the Boltzmann equation on the temperature, which serves as our time variable in the calculation, is hidden in the integral $I(y)$. This integral cannot be analytically solved.

The goal now is to calculate the yield at any given point in the history of the Universe starting from the point of reheating up to the point of symmetry breaking. Hence we can integrate Eq.(4.8) from $y_{min} = \frac{T_{re}}{m_\phi}$ to $y_{max} = \frac{T}{m_\phi}$. The boundaries of the integral are identified with the beginning of UV production at T_{re}, characterized by y_{min} and with a given temperature T at which you would want to know the contribution of UV production to the dark matter yield, represented by y_{max}. If $y_{max} \sim 1$, which corresponds to $T \sim m_\phi \sim v_\phi$, the point of symmetry breaking, it is possible to calculate the UV contribution to the dark matter relic abundance. For $T < T_\phi \sim v_\phi$ there will be no more significant dark matter production coming from UV Freeze-In.

As mentioned at the beginning of this section, the Feynman diagram as shown in the scheme, Figure 3.1, is not the only interaction that creates dark matter using the higher-dimensional operator from Eq.(3.4). One can do permutations of the particles involved in this diagram and find other two-by-two processes that produce dark matter, being $\phi\ell \to \tilde{\ell}\chi$ and $\ell\tilde{\ell} \to \phi\chi$, as shown in Figure 4.1. These three different Feynman diagrams however do not all have the same Feynman amplitude. In fact, the two diagrams that we have not discussed yet have the same amplitude which is different than the one used in the illustration so far. Their Feynman amplitude is given by

$$|\mathcal{M}|^2 = \frac{s + t - m_\phi^2}{\Lambda^2}\,, \tag{4.9}$$

where $t = (p_1 - p_3)^2$ is the Mandelstam variable. That leads us to write an additional contributing factor to the integral $I(y)$ coming from the other two Feynman diagrams, Eq.(4.7), as

$$F(y) = \frac{2}{y^5}\int_1^\infty dz\,\frac{(z-1)^2}{2\sqrt{z}}K_1\left(\frac{\sqrt{z}}{y}\right)\,, \tag{4.10}$$

where the 2 in front comes from the other two diagrams having the same amplitude and thus contribution to the UV yield. For more detailed calculations, please consider reading the appendix A.2. Using this additional factor, we can write the total yield as

$$\frac{dY^{UV}_{Total}}{dy} = -\frac{45\,m_\phi}{512 g_S \pi^7 1.66\sqrt{g_\rho}\Lambda}\,\frac{M_{Pl}}{\Lambda}\left(I(y) + F(y)\right)\,, \tag{4.11}$$

It is however useful to try and get an analytical estimate for the integral. This estimate is computed by looking at the limits of the boundaries of the integral.

We begin this analytical estimate by looking at Eq.(4.6), the yield for the interaction $\phi\tilde{\ell} \to \ell\chi$. Let's take the approximation where we go to the limit where $s \gg m_\phi^2$ or $z \gg 1$. Then the integral $I(y)$ becomes

$$I(y) = \frac{1}{y^5}\int_0^\infty dz\, z^{3/2}\, K_1\left(\frac{\sqrt{z}}{y}\right)\,, \tag{4.12}$$

and is analytically solvable. The result of this integral is 32, leading to

$$Y^{UV}_{\phi\tilde{\ell}\to\ell\chi} = \frac{45\,M_{Pl}}{16\,g_S\pi^7\,(1.66)\sqrt{g_\rho}\Lambda^2}T_{re}\,, \tag{4.13}$$

where we integrated from T_{re} until now, $T_0 \approx 0$. However, this is only for the first diagram with amplitude Eq.(4.2). To compute the integral for the other diagrams, we need to take $z \gg 1$ in Eq.(4.10), hence $(z-1)^2 \simeq z^2$. In this regime, we find the same integral as in Eq.(4.12). This means that the total analytical yield is written as

$$Y^{\infty}_{UV,Total} = \frac{2 \times 45\,M_{Pl}}{16\,g_S\pi^7\,(1.66)\sqrt{g_\rho}\Lambda^2}T_{re}\,, \tag{4.14}$$

where the extra factor 2 comes into play, because the other two diagrams combined have the same contribution in this limit as the first diagram. The most important lesson from this equation is the behaviour of $Y \sim \frac{T_{re}M_{Pl}}{\Lambda^2}$. This will help understanding the behaviour of the plots in the following section. It is clear that an important parameter in the UV case is the temperature of reheating. All significant production in the UV regime will happen close to this temperature.

4.2 IR production

In the IR production regime, we are in the broken phase of the $U(1)_D$ symmetry, working with the operator in Eq.(3.2). This regime produces dark matter via a different interaction than UV Freeze-In. It utilises a decay of the mediator instead of a scattering process. The Feynman diagram of this process is shown in Figure 3.1 on the bottom row of the scheme.

The corresponding amplitude for this diagram is

$$|\mathcal{M}|^2 = \left(\frac{v_\phi}{\Lambda}\right)^2 (m_{\tilde{\ell}}^2 - m_\chi^2), \tag{4.15}$$

where we assumed that the mass of the lepton is negligible compared to m_χ and $m_{\tilde{\ell}}$, see the calculations in Appendix A.2. From the amplitude follows that the decay rate is given by

$$\Gamma_{\tilde{\ell}} = \frac{1}{16\pi}\left(\frac{v_\phi}{\Lambda}\right)^2 m_{\tilde{\ell}}\left(1 - \left(\frac{m_\chi}{m_{\tilde{\ell}}}\right)^2\right)^2 . \tag{4.16}$$

We immediately see that there is a heavy dependence of the decay rate on the mass of the mediator, the coupling v_ϕ/Λ and the ratio between the dark matter mass and the mass of the mediator.

It is again necessary to write down the Boltzmann equation for this process, which is given by

$$\begin{aligned}\dot{n}_\chi + 3Hn_\chi = \int & d\Pi_\chi d\Pi_{\tilde{\ell}} d\Pi_\ell (2\pi)^4 \delta^4\left(p_\chi + p_\ell - p_{\tilde{\ell}}\right) \\ & \times |M|^2_{\tilde{\ell}\to\ell+\chi} f_{\tilde{\ell}} ,\end{aligned} \tag{4.17}$$

where we neglected the reverse reaction. This can be rewritten using the same process as in section 2.4 such that

$$\dot{n}_\chi + 3Hn_\chi = \frac{g_{\tilde{\ell}}\, m_{\tilde{\ell}}^2\, \Gamma_{\tilde{\ell}}}{2\pi^2}\, T\, K_1\left(\frac{m_{\tilde{\ell}}}{T}\right) , \tag{4.18}$$

where $g_{\tilde{\ell}}$ are the degrees of freedom for the mediator. Using the same definition for the yield as in the UV case, we find that the yield becomes

$$Y_{IR} = \frac{45}{1.66\, 4\pi^4} \frac{g_{\tilde{\ell}}\, M_{Pl}\, \Gamma_{\tilde{\ell}}}{m_{\tilde{\ell}}^2\, g_S \sqrt{g^\rho}} \int_{x_{min}}^{x} dx\, K_1(x)\, x^3 , \tag{4.19}$$

where we defined a new variable $x = \frac{m_{\tilde{\ell}}}{T}$. The boundaries of this integral are defined as $x_{min} = \frac{m_{\tilde{\ell}}}{m_\phi}$ and $x = \frac{m_{\tilde{\ell}}}{T}$. These borders correspond respectively to the beginning of the IR production when the broken phase starts from $m_\phi \sim v_\phi$ and the temperature at which you would like to calculate the yield contribution of the IR production. By filling in the decay rate, Eq.(4.16), into Eq.(4.19), it is found that

$$Y_{IR} = \frac{45}{64(1.66)\pi^5} \frac{M_{Pl}\, g_{\tilde{\ell}}}{g_S \sqrt{g_\rho}} \left(\frac{v_\phi}{\Lambda}\right)^2 \frac{1}{m_{\tilde{\ell}}} \left(1 - \frac{m_\chi^2}{m_{\tilde{\ell}}^2}\right)^2 I(x) , \tag{4.20}$$

where

$$I(x) \;=\; \int_{x_{min}}^{x} dx\, K_1(x)\, x^3. \tag{4.21}$$

Like in the UV case, the goal is to compute the yield of dark matter at any temperature. The temperature dependence of the yield is hidden in x. It is also possible to calculate the IR contribution to the dark matter relic abundance if we take $x = x_{max} = \infty$ and take $x_{min} = 0$, see the discussion in section 2.4.2. Most of the IR production is dominated at low temperatures, so the Freeze-In computation is not that sensitive to the high temperature behaviour. For these boundaries, the integral $I(x)$ becomes analytically solvable and is nothing more than $3\pi/2$, which leads us to write

$$Y_{IR}^{\infty} = \frac{135}{128(1.66)\pi^4} \frac{M_{Pl}\, g_{\tilde{\ell}}}{g_S\sqrt{g_\rho}} \left(\frac{v_\phi}{\Lambda}\right)^2 \frac{1}{m_{\tilde{\ell}}} \left(1 - \frac{m_\chi^2}{m_{\tilde{\ell}}^2}\right)^2 . \tag{4.22}$$

From this analytic estimate, we can learn how the IR dark matter yield depends on the different parameters of the model. When looking at Eq.(2.24), it is noticed that the computed yield agrees with the form of the general term. The decay rate is present as well as the dependence on $m_{\tilde{\ell}}$ and the M_{Pl} factor. As expected there is also a dependence on the ratio between the masses of dark matter and the masses of the mediator, since a decay can only happen if the sum of the masses of the decay products is smaller than the mass of decaying particle. Hence, when neglecting the mass of the lepton, if $m_{\tilde{\ell}}$ comes close to m_χ, Y_χ^{IR} should go to zero. This is seen in Eq.(4.22), because of the 1 - $m_\chi^2/m_{\tilde{\ell}}^2$ factor. If $m_{\tilde{\ell}} < m_\chi$, the roles would be reversed and the dark matter particle would decay in the mediator, meaning that the mediator would become the dark matter particle. However this cannot be the case, since the mediator is charged, which is impossible for dark matter. Hence, it is required that $m_{\tilde{\ell}} > m_\chi$.

It might also be interesting to investigate in which regime the IR production is dominant and if we can set a threshold on T_{re} such that for T_{re} smaller than this threshold, we know that the dark matter production is IR dominated. We can examine this using the approximated analytical yields from Eq.(4.14) for the UV production and Eq.(4.22) for the IR production. These two yields can then be compared

$$\frac{Y_{IR}^{\infty}}{Y_{UV,Total}^{\infty}} \backsimeq \frac{3\pi^3 g_{\tilde{\ell}}}{8} \frac{(v_\phi)^2}{T_{re} m_{\tilde{\ell}}}, \tag{4.23}$$

where it was assumed that $m_\chi \ll m_{\tilde{\ell}}$. Now consider a situation where the IR contribution is dominating, $\frac{Y_{IR}}{Y_{UV}} > 1$. That leads to the following threshold for T_{re}, depending on v_ϕ and $m_{\tilde{\ell}}$

$$T_{re}^{thr} = \frac{3\pi^3 g_{\tilde{\ell}}}{8} \frac{v_\phi^2}{m_{\tilde{\ell}}}. \tag{4.24}$$

If T_{re} would be bigger than the threshold T_{re}^{thr}, we know that the UV contribution of the dark matter production dominates, while if T_{re} would be smaller, then the IR contribution dominates. If T_{re} is however comparable to the threshold, then we have a mixed contribution, where neither of the two mechanisms dominate and both production regimes contribute significantly. In section 4.3, we will do the numerical computations of the dark matter yield and discuss if this analytical threshold is consistent with those results. This will be the case for all regimes of dark matter production.

This concludes the discussion for the two relevant production mechanisms in the minimal model of this thesis. We now continue by calculating the yield and the relic abundance in sections 4.3 and 4.4 for the minimal model of the thesis using the concepts introduced up until now.

4.3 Dark Matter Yield

We will now do the full numerical computation of the dark matter yield in multiple regimes, following its behaviour throughout the time evolution of the Universe. In the previous subsections of this chapter, we already discussed the possible production channels of dark matter. It is now possible to combine all these production channels and compute the overall yield of dark matter at a certain time. This is shown in Figure 4.2. To make this figure, some parameters were fixed, shown in Table 4.1.

If T_{re} and therefore the UV dark matter Freeze-In production, represented as the blue dot-dashed line, is fixed, we can get different dominant production regimes by varying $v_\phi \sim m_\phi$ which varies the amount of IR production. Figure 4.2 examines the yield for three different values of v_ϕ. We can see the effect of varying v_ϕ when examining Eq.(4.16), there the decay rate of the process depends on the coupling squared. It follows that if v_ϕ is increased, then the decay rate and the IR yield which depends on the decay rate, also increase. This is the effect we see in Figure 4.2.

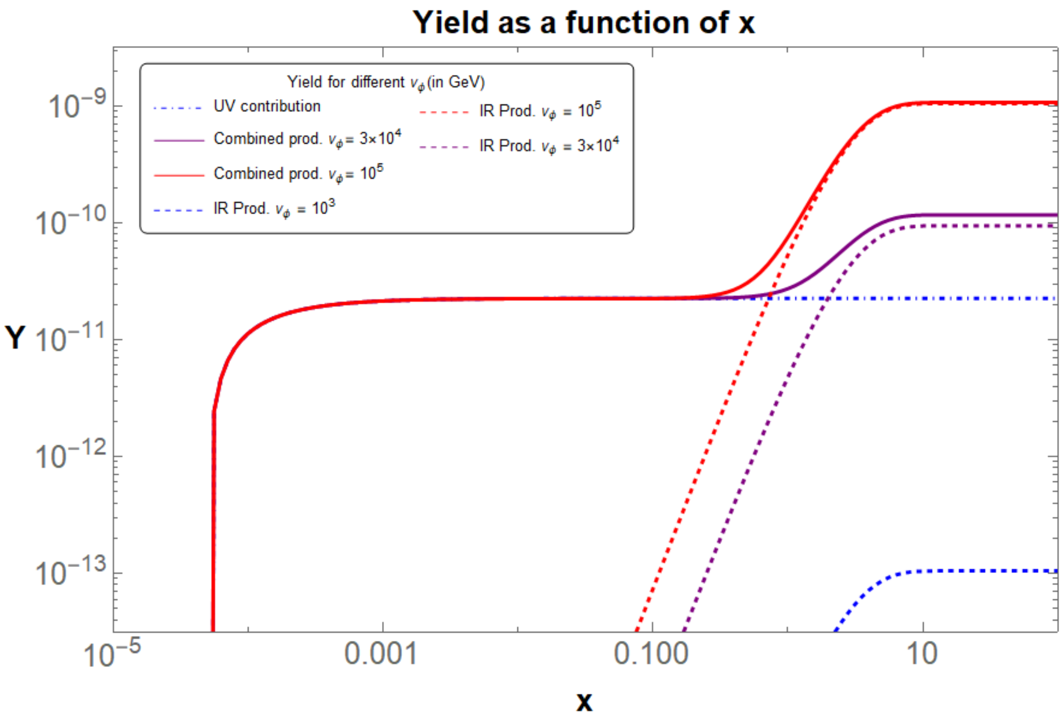

Figure 4.2: The yield Y of dark matter depending on $x = \frac{m_{\tilde{\ell}}}{T}$ is shown, which is a measure for the temperature and therefore the age of the Universe. The yield has been plotted for three different scenarios, where v_ϕ is different, in the dark matter production. One where $v_\phi = 10^5$ GeV and UV production is dominant, one where $v_\phi = 10^3$ GeV and IR production is dominant and one where $v_\phi = 3 \times 10^4$ GeV and neither is dominant and thus there is a mixed contribution. The total contributions of these three cases are given by the full lines. The dashed lines give the IR contribution in these cases. Since the UV contribution does not depend on v_ϕ, it is characterized by a single blue dot-dashed line which is the same for all three different scenarios, because T_{re} is constant in the three cases.

	m_χ	$m_{\tilde{\ell}}$	Λ	T_{re}
Value	1 GeV	500 GeV	10^{15} GeV	10^7 GeV

Table 4.1: To make Figure 4.2, some parameters of the minimal model were fixed to a certain value presented in this table.

Before analysing the three different cases, one can already make some general observations. It is seen as expected that the yield increases steeply at the early time of reheating because of the UV production and then stagnates in a plateau. Then, there is no activity until the IR production kicks in around $x \sim 0.1$.

The IR production will grow when the temperature decreases up until $T \sim m_{\tilde{\ell}}$ or $x \sim \mathcal{O}(1)$, where most of the IR production happens. After that stage, the mediator starts to become Boltzmann suppressed, because of its annihilation into SM particles and the dark matter production will no longer be significant. The IR production is different for the three values of v_ϕ and these three cases are discussed below.

The red lines represent $v_\phi = 10^5$ GeV where we calculate the yield as a function of $x = \frac{m_{\tilde{\ell}}}{T}$,. The full red line, which represents the combined UV and IR production, shoots up at the point where the IR production kicks in, represented by the red dashed line, and shows a situation where the IR production is the dominant factor in dark matter production. The IR contribution is also higher than in the other two cases, because the coupling v_ϕ/Λ of the interaction is the biggest for the three regimes.

The magenta lines represent $v_\phi = 3 \times 10^4$ GeV and shows a mixed situation, where both the UV and the IR regime do have a significant contribution to the dark matter yield. This is noticed because the dashed magenta line does not completely overlap with the full line. However it does have a clear effect on the total yield. Since v_ϕ is smaller in this regime, the IR contribution will decrease compared to the red line, since the coupling is smaller. This effect is also visible in the figure, because the difference between the two instances is approximately one order of magnitude, which is the difference between v_ϕ^2 for the two cases.

Both the IR and UV contribution are of the same order of magnitude and have a significant contribution to the dark matter yield and therefore also its relic abundance. We will investigate the relic abundance further in the following section.

In all these calculations, it has been assumed that to compute the IR Freeze-In contribution the initial amount of dark matter abundance is negligible. However, one may wonder if this assumption holds, since before the IR Freeze-In the UV Freeze-In production can already create a significant contribution to the dark matter abundance. We can consider three cases. Looking at Figure 4.2, it is seen that in the case of an IR dominated dark matter production the UV contribution will be close to negligible anyway compared to the IR contribution, so in this regime the assumption holds. For a UV dominated production of dark matter, there is no problem as well since the IR contribution is not relevant.

The last regime is the most interesting one, namely the mixed contribution since here the already existing UV abundance cannot be neglected compared to the IR created abundance. The effect will modify the Boltzmann equation in Eq.(4.17), since we assumed an initial abundance of zero for dark matter. An existing initial abundance of dark matter will lead to depletion of the dark matter number density through processes like $B_2\chi \to B_1$ that have been neglected in our analysis. This modifies the dark matter relic abundance and yield in the IR-UV mixed region.

A detailed investigation of this depletion effect is beyond the scope of the thesis. However, such a modification will have an effect on the contours of the relic abundance, investigated in the next section in Figure 4.4. The only expected modification of the contours comes in the mixed region, where the contours bend, which will not impact qualitatively the outcome of our investigation and the connection to the second part of the thesis. We continue now with the discussion of Figure 4.2.

If we take $v_\phi = 10^3$ GeV, close to $m_{\tilde{\ell}}$, the blue line in Figure 4.2 is computed. This particular yield rises up in the beginning and stays constant when the contribution of IR production comes in. The IR contribution to the yield is around two to three orders of magnitude less than the UV contribution, which means it is negligible compared to the UV contribution. Hence, the blue line is an example of a UV-dominated yield for dark matter. The IR yield is the smallest in this case, because the coupling, dependent on v_ϕ, is the smallest of the three cases.

Figure 4.2 can also be made for a varying amount of UV dark matter production. In this case, the parameter that will be altered is T_{re} and v_ϕ will be fixed, therefore the IR production will be the same in all three cases since it is independent of T_{re}. From Eq.(4.14) it is clear that changing T_{re} will have a significant effect on the dark matter yield. This is shown in Figure 4.3. The parameters chosen to make this plot are displayed in Table 4.2.

From this plot, we notice very clearly that the temperature of reheating is an important parameter that determines the amount of dark matter produced via the UV production channel. The UV production rate scales with the temperature, therefore at larger temperatures the production will be larger as well. If T_{re} is increased, we also allow for higher temperatures and it follows that the UV production is increased as well.

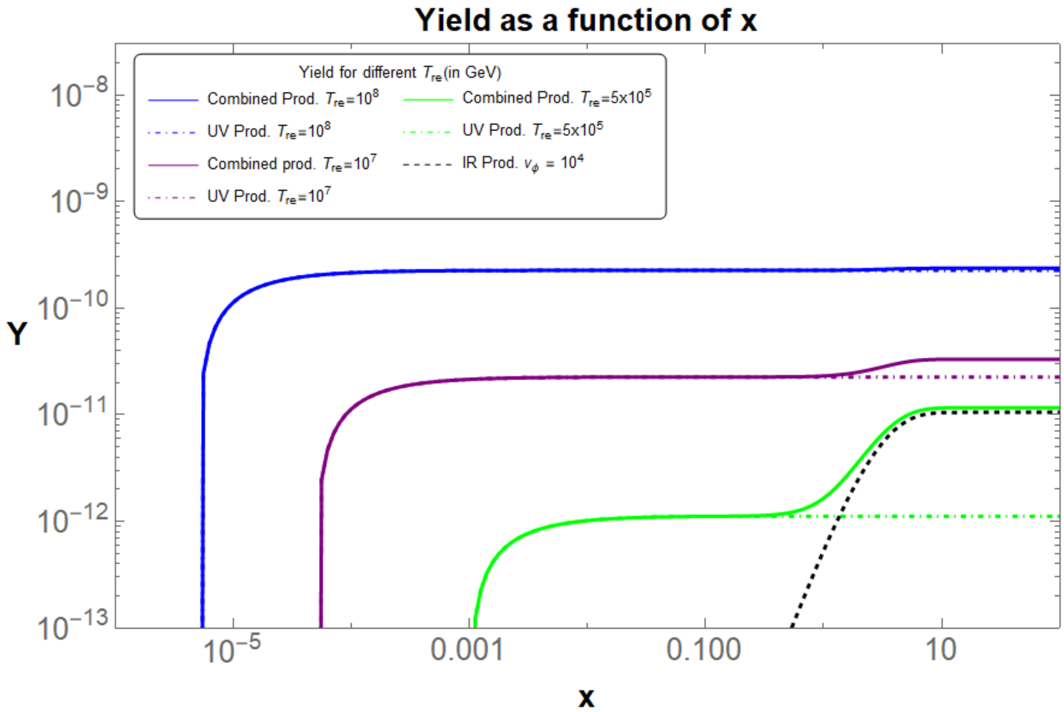

Figure 4.3: As in Figure 4.2, this plot shows the yield Y as a function of $x = m_{\tilde{\ell}}/T$. The yield has been computed for three different scenarios, where T_{re} has various values. We have taken $v_\phi = 10^4$ GeV fixed, such that the IR production is the same in all scenarios, given by the dashed black line. The dot-dashed lines give the UV contribution for each of the different scenarios and the full lines are the combined production channels for both the IR and UV production. Again, there is one scenario where UV production is dominant, for the highest T_{re}, one where IR is dominant and one where there is a mixed production.

	m_χ	$m_{\tilde{\ell}}$	Λ	v_ϕ
Value	1 GeV	500 GeV	10^{15} GeV	10^4 GeV

Table 4.2: The parameters in this table represent those chosen such that one can get an IR dominated, a mixed dominated and a UV dominated case for dark matter production keeping the IR production fixed. Since UV production is dependent on T_{re}, all other parameters present in the model can be fixed and T_{re} is varied to investigate the UV production dependence on it as seen in Figure 4.3.

For example the scenario where $T_{re} = 10^8$ GeV has an order of magnitude higher yield as the scenario where $T_{re} = 10^7$ GeV. That is in complete agreement with the analytical estimation of Eq.(4.14). In general one can say that if the UV production needs to be dominant, the temperature of reheating needs to be increased.

The third and last scenario in Figure 4.3 is when $T_{re} = 5 \times 10^5$ GeV. This is a significantly lower value for the temperature of reheating. As a result the UV contribution to the total dark matter yield is smaller compared to the other two scenarios. As seen in the figure, the IR contribution dominates this instance.

As a last check, we want to see if the analytical approximation for the threshold Eq.(4.24) is consistent with the results we see in Figure 4.2 and 4.3. We start by investigating the first figure. There we have taken T_{re} = 10^7 GeV, such that the UV contribution is fixed. It was also assumed that $m_{\tilde{\ell}}$ = 500 GeV. Therefore, Eq.(4.24) can be rewritten as

$$10^7\,\mathrm{GeV} \lesssim 22.5 \times \frac{v_\phi^2}{500\,\mathrm{GeV}}\,, \tag{4.25}$$

where $\pi^3 \sim 30$ and $g_{\tilde{\ell}} = 2$. We start comparing for $v_\phi = 10^3$ GeV. We fill in the right hand side and find 4.5×10^4 GeV for the threshold. Indeed, the temperature of reheating is bigger than this threshold and the UV contribution should dominate as is confirmed in the figure. Next up, we pick $v_\phi = 10^5$ GeV. Then we find that $T_{re} \lesssim 4.5 \times 10^8$ GeV. Therefore we expect here the IR contribution to be dominant according to Eq.(4.24) and as seen in the figure, this is confirmed by the numerical calculations.

We can also reverse the roles and consider Figure 4.3, where the IR contribution is fixed and $v_\phi = 10^4$ GeV. Then, Eq.(4.24) is

$$T_{re}^{thr} = 4.5 \times 10^6\,\mathrm{GeV}. \tag{4.26}$$

If T_{re} meets this requirement, then the IR contribution is the dominant one. This is confirmed by the analysis of the figure. The UV contribution is dominant for $T_{re} = 10^8$ GeV as is expected from the threshold. For $T_{re} = 5 \times 10^5$ GeV, which is lower than our requirement, the IR contribution dominates, again confirming that the analytical estimate of this relation is quite good. For the third and final scenario, the one where there is a mixed contribution, we have that $T_{re} = 10^7$ GeV. This value is close to the threshold in Eq.(4.26), where we expect that the UV and IR contribution are of the same order. We can conclude that our numerical results are in agreement with the analytical estimates. That concludes the segment about the dark matter yield and we can now go further by analysing the dark matter relic abundance.

4.4 Relic abundance

In this last part of the dark matter section from the thesis, we calculate the correct relic abundance contours of $\Omega h^2 = 0.12$, shown in Figure 4.4, for different values of three parameter ratios: M_{Pl}/Λ, T_{re}/Λ and v_ϕ/Λ. Ωh^2 can be calculated from the yield using Eq.(2.13). The three parameter ratios dependence of the relic abundance are hidden in the yield. For example, the IR yield depends on v_ϕ/Λ and M_{Pl}/Λ, see Eq.(4.22), while the UV yield depends on M_{Pl}/Λ and T_{re}/Λ, see Eq.(4.14).

First of all, we explain why these particular parameters were chosen. The scale Λ is the scale up to which the higher-dimensional operator is valid, however this scale cannot be bigger than the Planck mass. Therefore it is a good idea to look at the ratio between these two variables to get a general idea at the size of the effective scale and also to make sure the scale is not chosen to be too big.

This leads us to the parameter on the vertical axis of the plot, which is a measure of the UV production. It is the ratio between the temperature of reheating and the effective scale Λ. We take this ratio always smaller than 1, since $\Lambda > T_{re}$ at all times, because otherwise, the effective operator, Eq.(3.4), we use is no longer valid at all temperatures where most of the dark matter is produced in the UV regime.

However which contribution is dominant also depends on the parameter relevant for the IR case, the coupling or the ratio of v_ϕ and Λ, a measure of the IR production. This parameter can be found on the horizontal axis of the plot.

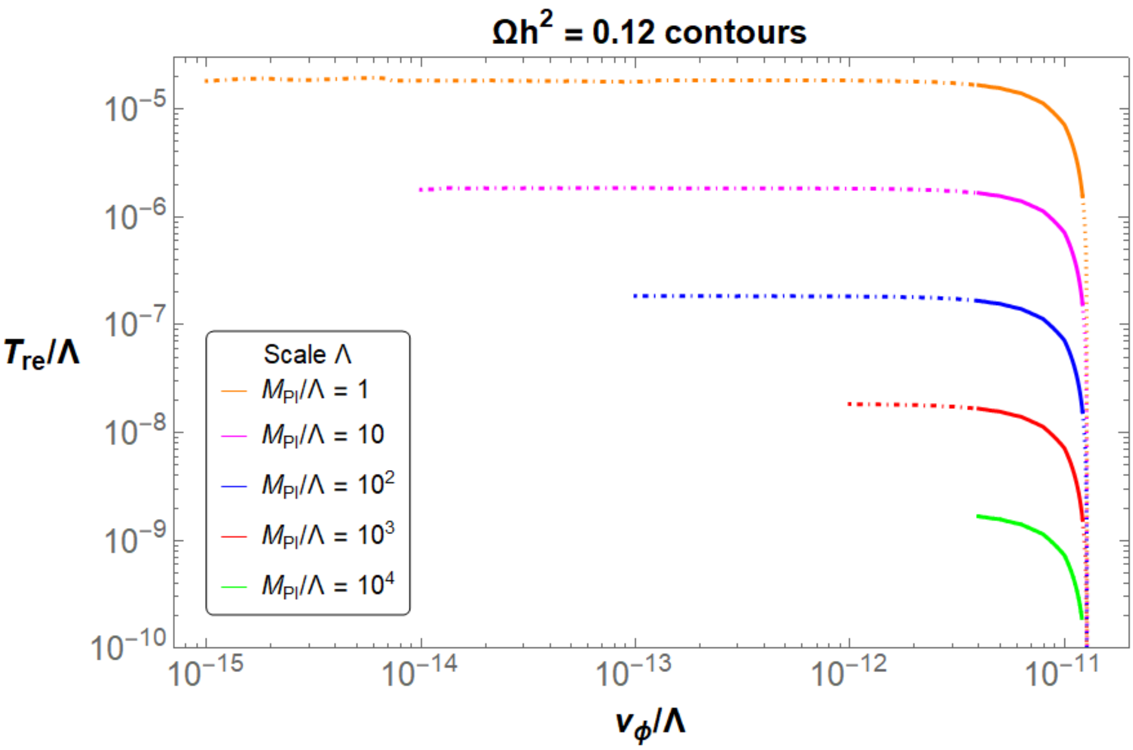

Figure 4.4: This shows the contour $\Omega h^2 = 0.12$ for different values in our parameter space for the ratio between the Planck mass M_{Pl} and the effective scale Λ. On the horizontal axis, we have the ratio between v_ϕ and Λ, which is a measure for the IR production, while on the vertical axis there is the ratio of T_{re} and Λ, which is a measure for the UV production. The contour lines are also divided into three parts. A dotted part on the right hand side where the IR production is dominant, a full line in the middle where the production is mixed which is not-dominant production in either UV or IR Freeze-In and a dot-dashed line where the UV production is dominant on the left hand side of the plot. A production channel is defined as dominant when $Y_{DOM} > 0.9\, Y_{total}$.

Therefore, what we see in the plot is at what parameter values of these ratios the dark matter production is either UV or IR dominated. A dot-dashed line stands for UV-dominated dark matter production, while a dotted line stands for an IR-dominated dark matter production. In between these two regimes, there is a mixed contribution, which is represented by a full line.

At higher values of v_ϕ/Λ, the dark matter production is IR-dominated. This is because the relic abundance of dark matter in the IR is directly related to this ratio. However, the interesting part here is that all the lines of different M_{Pl}/Λ-ratios come together at the same point for v_ϕ/Λ. This means that there is no dependence on T_{re}/Λ in this specific region of the plot. This is consistent with the previous explanations, in this region we are in an IR dominated regime and the UV contribution, which is dependent on T_{re}, does not play a role.

If we then follow the contours more to the left side of the plot, where they bend from a vertical line to a horizontal line, we encounter a region where the dark matter production is *mixed*. In this region, the UV Freeze-In and IR Freeze-In contribute both significantly to the overall dark matter relic abundance. We also observe that the contour lines in the mixed region of the plot, represented by the full lines, are turning from the vertical line of v_ϕ/Λ at around 10^{-11}, the IR dominated production, to the horizontal line of T_{re}, the UV dominated production. This lets us know that both ratio's are important in this regime, which is to be expected since we are in the mixed regime.

The last part of the plot on the left is the region where the UV contribution is dominant. In this case the lines do not come together into one point, however they do all stay horizontal in this regime. They all start to be UV-dominated at the same value for v_ϕ/Λ independent of the value of M_{Pl}/Λ. This is because v_ϕ/Λ only matters when there is a significant IR contribution. The UV process does not depend on this ratio, since in the UV case ϕ has not even taken a VEV, because UV production happens in the unbroken phase. Therefore, the moment when UV becomes dominant is the same for every single ratio M_{Pl}/Λ. The same reasoning applies for why the lines stay horizontal, since there is no dependence on v_ϕ/Λ in these regimes.

We also notice a change of the vertical position of the UV dominated contours for different ratio's of M_{Pl} and Λ. We see that if the ratio is lower, which means that the value of Λ is higher, then the contour of $\Omega h^2 = 0.12$ goes up on the graph. This is because Λ is higher, therefore the coupling of the interaction becomes smaller and the interaction needs to start sooner, and at higher energies, hence higher T_{re}, to still achieve the correct relic abundance $\Omega h^2 = 0.12$.

This effect is confirmed by studying the behaviour of the dark matter relic abundance in the UV regime. Inspecting Eq.(4.14), we see that $\Omega h^2 \sim T_{re}\frac{M_{Pl}}{\Lambda^2}$. If Λ becomes larger with one order of magnitude, then T_{re} has to increase with two factors of magnitude to maintain the same abundance in correspondence with the observations, therefore the ratio on the vertical axis of the plot will increase with one order of magnitude.

A last effect to be investigated is the reason why the contour lines stop in the plot. This is an effect of the mass hierarchy in the dark matter minimal model. To find Eq.(4.5), it is assumed that ϕ has the biggest mass. To make Figure 4.4, it was assumed that $m_{\tilde{\ell}} = 500$ GeV. Now take for example the orange line for the ratio M_{Pl}/Λ = 1 and examine the end of this contour on the left side in the figure. There v_ϕ/Λ = 10^{-15} so v_ϕ = 10^3 GeV. Because it is needed that $m_\phi \sim v_\phi > m_{\tilde{\ell}}$, the line stops there. If it went further m_ϕ would become too small for the assumptions used to calculate the yield and relic abundance to be valid.

With this, the dark matter part of this thesis is concluded and we can continue on with the next part about the stochastic background of gravitational waves and how this intersects with the dark matter minimal model of this thesis.

The gravitational waves arise when the new $U(1)_D$ symmetry spontaneously breaks and ϕ takes on a non-zero VEV. This effect is a first-order phase transition. Such a phase transition can possibly create a stochastic background of gravitational waves in the Early Universe via different types of processes. These gravitational waves travel throughout the Universe and reach the Earth. There experiments like LIGO, VIRGO but also upcoming experiments like LISA, BBO and Einstein telescope, can possibly observe such a signal from which we hopefully can deduce some properties of dark matter.

5 Gravitational Waves

This section will explain the phenomenon of gravitational waves with a strong focus on a stochastic background of gravitational waves or SBGW. The SBGW is analogous to the CMB for photons. In this section, we will explain the origin of the SBGW. A stochastic background of gravitational waves can be the result of a large number of independent sources, for example the merger of black holes or binary neutron stars. Such events taken together form the astrophysical background. However, the stochastic background of gravitational waves can also come from other sources of cosmological origin and then, it is referred to as the cosmological SBGW. For instance it can be generated during first-order phase transitions that occurred in the very Early Universe. The first-order phase transition arises when the finite temperature effective potential gets a different true minimum due to the temperature of the Universe decreasing thereby changing the form of the potential. The true vacuum of the potential changes and it is possible to quantum tunnel from the first and now false vacuum to the new true one. That leads to first-order phase transitions [33].

Gravitational Waves: Gravitational Waves can be analysed using General Relativity, first predicted by Albert Einstein [34]. These waves can be created when a mass is accelerated, for example in a merger of binary black holes. In its purest sense, a gravitational wave is a travelling gravitational field where the polarisation is transverse to the direction of the propagation of the wave. The effect of the gravitational wave is the stretching of space in one direction while contracting in the other direction, perpendicular to the propagation. The wave will also carry energy and momentum. However, gravitational waves are quite weak and therefore very massive astrophysical objects, such as binary black holes and binary neutron stars, which create very energetic events are needed for detectors to be able to observe these waves on Earth. The merger of such objects leads to the emission of gravitational waves, since there is an energy loss when the objects spiral in and merge together. It has to be noted that astrophysical sources are not the only ones that can create gravitational waves as mentioned before. Later on in Section 5.1 other possible sources and the one relevant to this project will be explored.

It is possible that the superposition of these individual events, coming from binary black holes, binary neutron stars or a combination of these two, make a stochastic background of gravitational waves that can be observed. The signals of the background can be observed on Earth by gravitational wave interferometers such as LIGO, VIRGO and KAGRA [35, 36, 37]. We will now try to give a small introduction to gravitational waves in linearized general relativity.

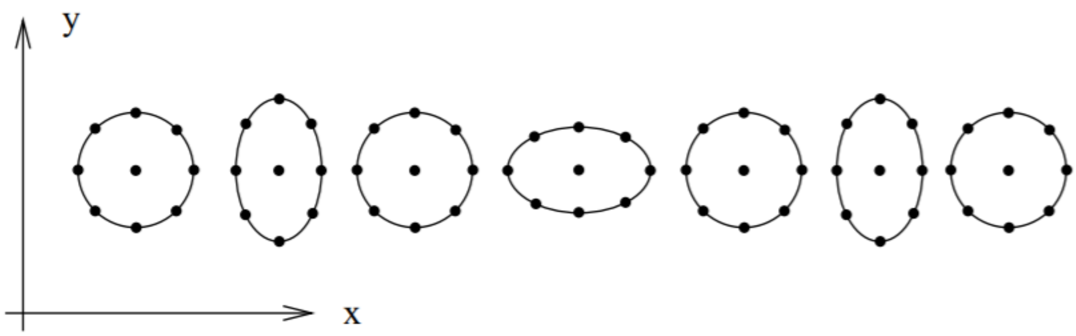

Figure 5.1: This shows the + polarisation of an oscillating gravitational wave. Figure taken from [1].

It is assumed that the wave only gives a slight modification to flat space

$$g_{\mu\nu} \sim \eta_{\mu\nu} + h_{\mu\nu}, \tag{5.1}$$

where $g_{\mu\nu}$ is the spacetime metric, $\eta_{\mu\nu}$ is the Minkowski metric and $h_{\mu\nu}$ is the metric perturbation leading to the gravitational waves. After being emitted, the wave will travel like a plane wave, for example in the z-direction. There are two possible polarisations transverse to the direction of the propagation. There is the $+$ polarisation, shown in Figure 5.1, and the $\times$ polarisation, shown in Figure 5.2. In the former case, the space will be expanded and contracted in the direction of the axes x and y, perpendicular to z, while in the latter case space will wiggle along axes which are rotated by $45°$ compared to the actual axes.

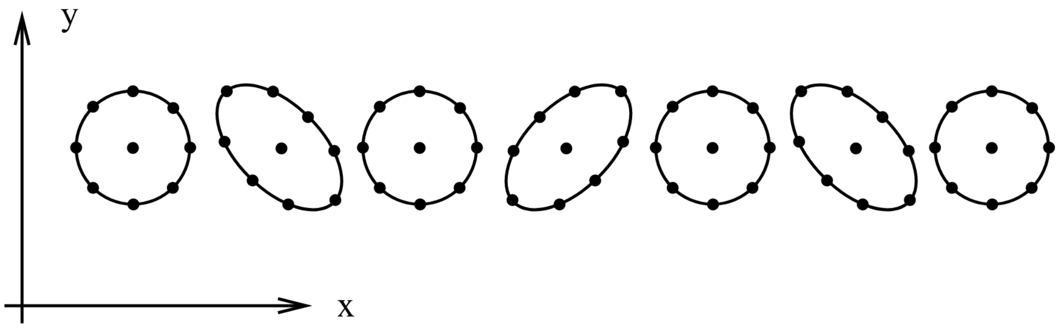

Figure 5.2: This figure shows the oscillation of a gravitational wave when it has $\times$ polarization. Figure taken from [1].

We can take a look at the metric perturbations of the $+$ polarisation by taking a plane wave in the z-direction

$$h_{ij}(z,t) = h_+ \begin{pmatrix} 1 & 0 & 0 \\ 0 & -1 & 0 \\ 0 & 0 & 0 \end{pmatrix}_{ij} e^{i(kz-\omega t)}. \tag{5.2}$$

We now imagine a length L_0 along the x- axis being perturbed by a gravitational wave. The wave causes the length to oscillate as

$$L(t) = L_0 + \frac{h_+ L_0}{2} cos(\omega t). \tag{5.3}$$

There is a change in the length along the $x-$axis. The length will stretch according to

$$\Delta L_x = \frac{h_+ L_0}{2} cos(\omega t). \tag{5.4}$$

Along the $y-$axis, there is a similar result, but in that case the length contracts

$$\Delta L_y = -\frac{h_+ L_0}{2} cos(\omega t). \tag{5.5}$$

Due to the oscillating nature of the waves, the axes will take turns stretching and contracting. The relative change of the length of the two arms is

$$\Delta L = \Delta L_x - \Delta L_y = h_+ L_0 cos(\omega t), \tag{5.6}$$

where

$$h_+ = \frac{\Delta L}{L_0}, \tag{5.7}$$

is the relative amplitude of the gravitational wave or the strain. It will be this strain which corresponds to the stretching and contracting of space as the physical effect of a gravitational wave that can be observed by the detectors on Earth like LIGO, VIRGO and KAGRA [38].

5.1 Stochastic background of gravitational waves

A stochastic background of gravitational waves or SBGW is observed differently than the gravitational waves coming from individual events. The latter ones are coming from very specific points in the Universe which are identified with specific individual events happening in the Universe, like a binary black hole merger. A stochastic background, think for example about the CMB, will be coming from all directions in a continuous way. The background can be either isotropic or anisotropic depending on its origin. There are two possible types of SBGW. Indeed, as already mentioned, it can have an astrophysical origin or a cosmological origin. The SBGW can be very useful trying to probe the earliest moments of the Universe, for example when trying to study inflation.

A stochastic background appears as noise in a single detector, because for example in the binary black holes background it is a superposition of overlapping individual events. The signal in a detector would be the sum of noise $n(t)$, coming from other outer sources and the gravitational wave coming from the stochastic background $h(t)$ written as

$$s(t) = n(t) + h(t), \tag{5.8}$$

but with $n(t) \gg h(t)$. One way to detect the stochastic background is to take the correlation between two detectors

$$\begin{aligned}\langle s_1(t)s_2(t)\rangle &= \langle (n_1(t) + h(t))(n_2(t) + h(t))\rangle \\ &\sim \langle h(t)h(t)\rangle,\end{aligned} \tag{5.9}$$

where $\langle\rangle$ represents the time average. The background is not detectable in a single detector. It is by looking at the correlation of the data from both detectors that we can detect a SBGW if the sensitivity of the detector is good enough.

Gravitational waves from the Early Universe can have a wide range of frequencies, however the existing detectors, like LIGO and VIRGO have an observational band between 10 Hz and a few kHz [35]. It is estimated that in this band there will be a significant contribution from the astrophysical SGWB of binary mergers.

The magnitude of the SBGW is usually given in terms of energy density per logarithmic frequency interval with respect to the critical density of the Universe, which means that

$$\Omega_{GW}(f) = \frac{f}{\rho_c}\frac{d\rho_{GW}}{df}, \tag{5.10}$$

with ρ_c the critical density, given in Eq.(2.11). Given this formula for the spectrum, one may ask what are the possible sources for a GW spectrum. As mentioned in the introduction a stochastic background can come from different kinds of sources with a different origin, astrophysical or cosmological. In the following paragraphs there will be an overview of these possible sources for a SBGW.

5.2 Sources for SBGW

Astrophysical sources: The SBGW coming from astrophysical sources will be a superposition of multiple individual events coming from astrophysical objects, such as black holes, neutron stars and others. However, it has to be noted that this background is present mainly due to a resolution problem. More advanced detectors, like the future Einstein Telescope, would possibly be able to observe more mergers individually, no longer seeing them as noise and a background. That will in turn lead to to the possibility of these detectors being more sensitive to backgrounds produced by other sources, such as first-order phase transitions. The most important contributions of astrophysical origin are mentioned here.

- Binary Black Holes or BBH: This is one of the most probable sources for the SBGW. Due to the detection of signals from BBH in LIGO and VIRGO, it is reasonable to assume that there is a significant population of BBH in the Universe, which could then create a SBGW. This background would have sources coming from over the whole history of the Universe. If we want to estimate the background coming from BBH mergers, there are many factors that have to be taken into account. An important point is to know how the binaries are formed, which would explain how often these mergers occur in the Universe. The reason why they are formed would have an influence on the formation rate and merger rate of these objects.

  BBH are formed in binary systems of massive stars. They typically have a low metallicity, which is the abundance of elements heavier then hydrogen and helium present in an object. An other possible formation channel for BBH is through dynamical interactions in dense stellar environments, such as globular clusters. Such clusters can produce a significant population of massive BBH that merge in the local Universe. The formation rate of the BBH affects the production of the SBGW. A more exotic formation channel is that of primordial black holes, produced in the Early Universe. It is probable that the amplitude of the signal coming from the primordial black holes is much lower than the amplitude of the signal arising from the stellar BBH mergers.

- Binary Neutron Stars or BNS: A stochastic background of BNS would come from every neutron star merger in the Universe. These mergers follow the same concept as the BBH. The only difference is that the mergers happen here between neutron stars, the second most massive astrophysical object after black holes. The process is the same: these neutron stars are made in a binary star system after the life of these stars. After some time it is possible that they merge by spiraling into each other thereby losing energy in the form of gravitational waves.

  Using observations of LIGO, the energy density for this source can be predicted as $\Omega_{GW} = 0.7^{+1.5}_{-0.6} \times 10^{-9}$ for a frequency of 25 Hz. This can be compared to the predicted background coming from binary black holes $\Omega_{GW}(f\text{=25 Hz}) = 1.1^{+1.2}_{-0.7} \times 10^{-9}$. The combination of the two gives the total astrophysical background predicted by LIGO and VIRGO observations at $\Omega_{GW}(f\text{=25 Hz}) = 1.8^{+2.7}_{-1.3} \times 10^{-9}$ [39]. The difference between BNS and BBH is that BBH signals happen fast compared to the average length between two individual different events. However for BNS signals this is not the case, hence there is a greater chance for BNS events to overlap. As a last note, there might also be a background coming from a neutron star and a black hole merger.

Cosmological sources: A SBGW can also come from cosmological sources, such as inflation and first-order phase transitions. This is a real stochastic background and cannot be resolved when using more sensitive or better detectors. It will be isotropic. Some information about these sources can be found in the following paragraph.

- Inflation: It is possible for gravitational waves to be produced at the end of inflation, during the period of reheating, when the inflaton decays into the visible sector. These waves could have information about the Universe in the inflation era. They would exist over a wide range of wavelengths corresponding to the size of the observable Universe to subatomic distances.

- First-Order Phase Transitions or FOPT: This will be the source for gravitational waves we are interested in in this thesis. A phase transition happens continuously in the daily life, for example when you warm up water to its boiling point. However, there could also be more abstract phase transitions. In the minimal model, we will consider a phase transition (or PT) when tunneling happens between a false and true vacuum of the potential. Such a first-order phase transition in the Early Universe could produce a SBGW. A PT can lead to bubbles forming in space that sit in a different vacuum than the other parts of the Universe. In the minimal model in this thesis, it will be a different vacuum expectation value for the ϕ field. These bubbles can then create GW by colliding with other bubbles or creating sound waves or turbulence in the plasma around them. Hence the characteristics of the gravitational waves will depend on the properties of the bubbles. In the following section the origin of these FOPT will be investigated further.

An overview of the sources for a SBGW together with the sensitivity of some gravitational waves interferometers is given in Figure 5.3. There it is seen that the current experiments, LIGO and VIRGO, might be capable in their upgraded version to just observe the astrophysical background. LISA however should be capable to observe that background more easily. The sensitivity of these detector has been shown as a curve in the figure. We discuss those curves and what they represent in the following section.

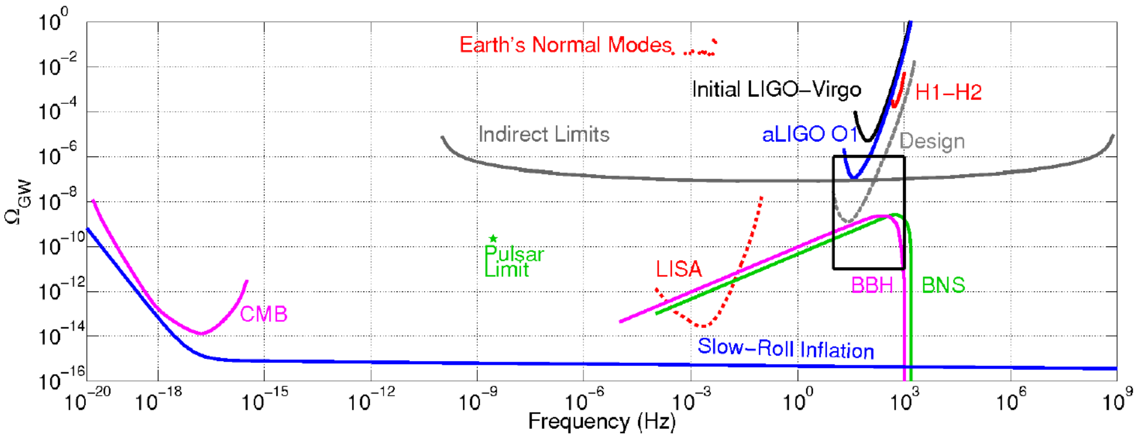

Figure 5.3: This overview shows the GW spectra coming from different sources together with the sensitivity curves of some detectors as a function of the frequency of the waves. The expected astrophysical background from Binary Black Holes (=BBH) and Binary Neutron Stars (=BNS) is shown as well as the expected background from slow-roll inflation. Also shown in the figure are the sensitivity curves for interferometers LIGO and VIRGO and their upgraded versions as well as the curve for LISA. There are also some constraints shown on the GW background, for example from the CMB, indirect limits and pulsars. Figure taken from [33].

5.3 PLS curves

To check if the computed GW spectra would be visible in detectors, the sensitivity of a detector must be calculated. The sensitivity of a detector of gravitational waves can be characterized by a power law integrated sensitivity curve or PLS. To illustrate the concepts in that computation we will focus in this section on the PLS of the upcoming space detector LISA [40] and reproduce the results and calculations of [41].

LISA will be the first ever space laser interferometer observatory specifically designed to detect gravitational waves. It has been proposed to consist of 2.5 million km length arms and have four years of nominal duration, which could be extended to ten years. The range of LISA will lay in the milli-Hertz range of frequencies, which can be very interesting for the dark matter minimal model of this project, see section 6.3.

The concept of power law integrated sensitivity curves or PLS can now be introduced, which is a graphical representation of the ability of a detector to measure a SBGW with a power law spectrum for a given signal-to-noise ratio or SNR and integration time. The first assumption to be made is that the actual data taking of LISA can only take place three years of the foreseen four, since the data is expected in chunks and hence there are some interruptions which ensure that it is not taking data for the full four years.

All noise components can be combined into one power spectral density or PSD noise function called $P_n^{(X)}$. More details can be found in [41]. From the noise function, one can construct the detector strain sensitivity curve $S_n(f)$. The signal-to-noise ratio is given in terms of the detector response PSD and the noise PSD

$$\mathrm{SNR} = \sqrt{t\int_0^\infty df \left(\frac{P_r(f)}{P_n^{(X)}(f)}\right)^2} = \sqrt{t\int_0^\infty df \left(\frac{S_h(f)}{S_n(f)}\right)^2}\,, \tag{5.11}$$

where t is the observation time.

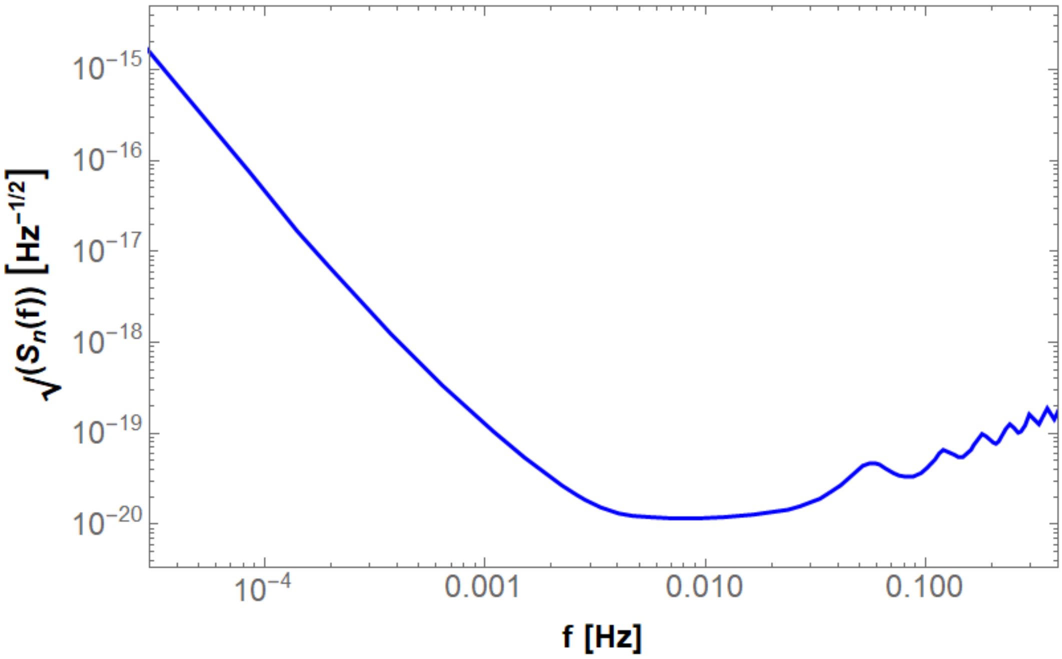

Figure 5.4: This shows the LISA strain sensitivity curve $S_n(f)$ [41].

The interest of this project is a stochastic GW background. The signal is expressed in terms of the GW energy density power spectrum defined in Eq.(5.10), which can be related to the GW strain PSD through

$$\Omega_{GW}(f) = \frac{4\pi^2}{3H_0^2} f^3 S_h(f)\,, \tag{5.12}$$

where H_0 = 100 h km s^{-1} Mpc^{-1} is the Hubble constant. We chose $h \simeq 0.67$ according to its observed value by Planck experiment [42]. Similarly, one can define the energy density sensitivity $\Omega_s(f)$ through the detector strain sensitivity as

$$\Omega_s(f) = \frac{4\pi^2}{3H_0^2} f^3 S_n(f). \tag{5.13}$$

The signal-to-noise ratio of a SBGW is then given by

$$\mathrm{SNR} = \sqrt{t\int_{f_{min}}^{f_{max}} df \left(\frac{\Omega_{GW}(f)}{\Omega_s(f)}\right)^2}\,, \tag{5.14}$$

where f_{min} and f_{max} denote the minimal and maximal frequencies of the detector range. The SNR increases with the square root of the observation time t. In [43], they introduce a graphical tool to visualise the improvement in sensitivity of a detector to a SBGW. This is called the PLS, a sensitivity curve constructed in such a way that every power law stochastic signal above it has an SNR larger than a certain threshold $\mathrm{SNR_{thr}}$. The SBGW described by a single power law can be compared to this PLS of the detector and that comparison indicates if the signal is detectable with a certain SNR_{thr} or larger.

The PLS will be constructed as follows. It is assumed that the signal of SBGW has a power law $\Omega_{GW}(f) = C_\beta f^\beta$ with a certain coefficient or power β. For each β that needs to be examined, one can find the value of C_β that provides a SNR equal to the threshold value SNR_{thr} across the LISA band given by

$$SNR_{thr} = \sqrt{t \int_{f_{min}}^{f_{max}} df \frac{C_\beta^2 f^{2\beta}}{\Omega_s^2(f)}}. \tag{5.15}$$

This process is repeated for values of β ranging from large negative values to a large positive ones. The PLS is then obtained by finding for each frequency the maximum value of $C_\beta f^\beta$. In this way it is guaranteed that a signal behaving as a power law has an SNR value greater than the threshold.

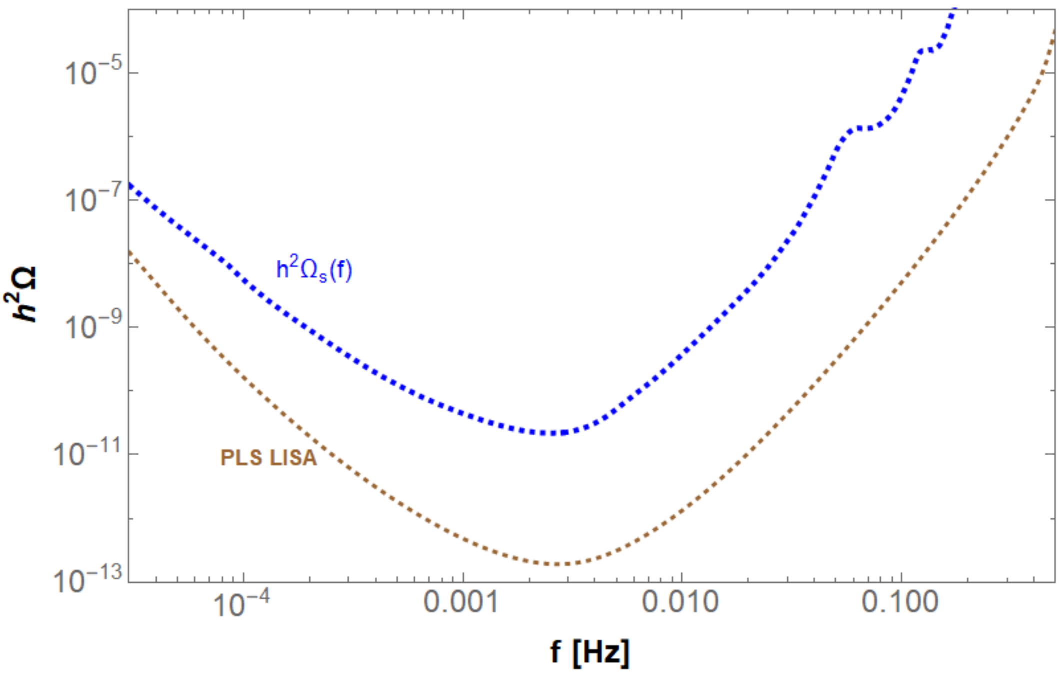

Figure 5.5: This shows the reproduced PLS curve in brown for LISA together with $h^2\Omega_s(f)$ coming from the strain sensitivity $S_n(f)$ from Figure 5.4 as the blue dotted line.

A last thing to choose when we want to reproduce the PLS curve of LISA is the choice of the threshold value. Following the process from [41, 44] the value of SNR_{thr} is chosen to be 10. As mentioned before the observation time will be equal to three years or $3 \times 3.154 \cdot 10^7\ s$. It is time to compute the PLS ourselves.

To start, one needs to know $S_n(f)$ such that $\Omega_s(f)$ can be calculated. This has been computed in [41], see Figure 5.4.

From this given detector strain sensitivity, one can compute the energy density sensitivity, Eq.(5.13), which is needed to calculate SNR. Assuming the power law signal for $\Omega_{GW} = C_\beta f^\beta$ and finding the correct coefficients C_β such that $\mathrm{SNR}_{thr} = 10$ for every β is the next step. By looking at every frequency and finding the maximum coefficient C_β

the PLS for LISA is reproduced, given in Figure 5.5, where it is shown together with the energy density sensitivity $\Omega_s(f)$.

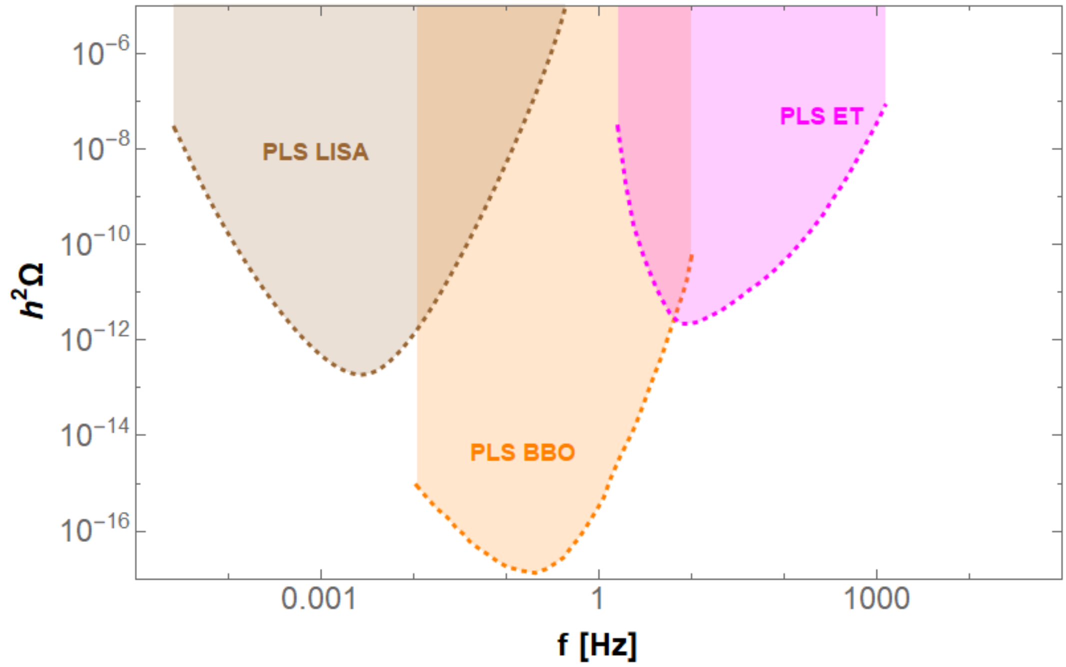

Figure 5.6: This figure shows the different PLS curves for three different types of detectors, LISA in brown, BBO in orange and Einstein Telescope in magenta.

Apart from LISA, there are also other (upcoming) experiments like BBO [45] and the Einstein Telescope [46] for which we want to know the PLS curve such that they can be compared to the computed spectra. These PLS curves are taken respectively from [47, 48, 49] and [49, 50] and are shown together in Figure 5.6. It should be noted that these PLS curves are already more sensitive than the existing LIGO and VIRGO experiments and therefore are interesting for the minimal model in this project, since the GW spectra that are calculated in this model can reach these PLS curves. These PLS curves can then be combined with the computed spectrum of the model to achieve the goal of this project and see if it might be possible to observe some GW spectra coming from our dark matter minimal model. We examine the detectability of the signals in section 6.3.

This concludes the examination of the sensitivity of the experiments. We continue now on our investigation into describing a SBGW coming from first-order phase transitions by examining the important concept of a finite temperature effective potential.

5.4 Finite temperature effective potential

Since first-order phase transitions will be important in this thesis, a closer look will be taken at the stochastic background coming from these events. First order phase transitions are described in quantum field theory by the dynamics of a scalar field whose vacuum expectation value changes during the cooling of the Universe. The first concept that needs to be introduced is the finite temperature effective potential [51, 52].

The finite temperature effective potential consists of three parts. First of all there is the potential present in the Lagrangian, the tree-level potential. The second part is the one-loop potential. This is the correction to the potential due to one-loop diagrams. Last of all, there is the finite temperature or thermal part of the potential that arrives into the picture when looking at finite temperature quantum field theory. This is important since the phase transition will happen in a hot plasma at a non-zero temperature.

As an example, consider the model of a self-interacting real scalar field

$$\mathcal{L} = \frac{1}{2}\partial^{\mu}\phi\partial_{\mu}\phi - V_0(\phi)\,, \tag{5.16}$$

with

$$V_0 = \frac{1}{2}m^2\phi^2 + \frac{\lambda}{4!}\phi^4, \tag{5.17}$$

the tree-level potential. Now, the tree-level potential gets corrected, because of one-loop and finite temperature effects. First of all there is the one-loop zero-temperature effective potential

$$V_{eff}(\phi) = V_0(\phi) + V_1(\phi)\,, \tag{5.18}$$

with the one-loop contribution

$$V_1\left(\phi\right) = \frac{1}{2}\int \frac{d^4p}{(2\pi)^4}\log\left[1 + \frac{\lambda\phi^2/2}{p^2+m^2}\right]. \tag{5.19}$$

The shifted mass is defined as

$$m^2(\phi) = \frac{d^2V_0(\phi)}{d\phi^2} = m^2 + \frac{1}{2}\lambda\phi^2\,, \tag{5.20}$$

such that the one-loop contribution can be rewritten as

$$V_1\left(\phi\right) = \int \frac{d^4p}{(2\pi)^4}\log\left[p^2 + m^2(\phi)\right]. \tag{5.21}$$

For more details, consider checking [51].

The integral that defines the one-loop effective potential will be UV divergent. That is a problem and therefore the potential has to be regularized. This can be done by introducing counterterms that will cancel the divergencies coming from the one-loop contributions. In the example above, counterterms would be added as

$$V_1^{c.t.} = \delta\Omega + \frac{\delta m^2}{2}\phi^2 + \frac{\delta\lambda}{4}\phi^4. \tag{5.22}$$

The expression of the effective potential will become finite, depending on the regularisation and on the renormalisation condition. We will describe two examples of both regularisation and renormalisation.

The first way to tackle regularisation is dimensional regularisation introduced by 't Hooft and Veltman. The details of the process can be found in [53]. There one takes the number of spacetime dimensions of the problem to be a general n. The one-loop potential would in that case look like

$$V_1\left(\phi\right) = \frac{1}{2}\left(\mu^2\right)^{2-\frac{n}{2}}\int \frac{d^np}{(2\pi)^n}\log\left[p^2 + m^2\left(\phi\right)\right]\,, \tag{5.23}$$

where μ is a mass scale which is needed to balance the dimension of the integration measure. The integral in Eq.(5.23) can be calculated using the derivative of the potential w.r.t. $m^2(\phi)$

$$V' = \frac{1}{2}\left(\mu^2\right)^{2-\frac{n}{2}}\int \frac{d^np}{(2\pi)^n}\frac{1}{p^2+m^2\left(\phi\right)}. \tag{5.24}$$

This integral is simpler to compute, using [51]

$$\int d^np\frac{\left(p^2\right)^{\alpha}}{\left(p^2+M^2\right)^{\beta}} = \pi^{\frac{\pi}{2}}\left(M^2\right)^{\frac{\pi}{2}+\alpha-\beta}\frac{\Gamma\left(\alpha+\frac{n}{2}\right)\Gamma\left(\beta-\alpha-\frac{n}{2}\right)}{\Gamma\left(\frac{n}{2}\right)\Gamma(\beta)}\,, \tag{5.25}$$

and integrating the result w.r.t. $m^2(\phi)$, one finds

$$V_1(\phi) = -\frac{1}{32\pi^2} \frac{1}{\frac{n}{2}\left(\frac{n}{2}-1\right)} \left(\frac{m^2(\phi)}{4\pi\mu^2}\right)^{\frac{n}{2}-2} \Gamma\left(2-\frac{n}{2}\right) m^4(\phi)\,. \tag{5.26}$$

This can be expanded in powers of 2 - $n/2$ keeping in mind that n = 4 in the case of this thesis. The expansion

$$\Gamma(z) = \frac{1}{z} - \gamma_E + \mathcal{O}(z)\,, \tag{5.27}$$

where γ_E is the Euler-Mascheroni constant, will be used to simplify Eq.(5.26). It is found that

$$\begin{aligned} V_1(\phi) = \frac{m^4(\phi)}{64\pi^2} \Bigg\{ &-\left[\frac{1}{2-\frac{n}{2}} - \gamma_E + \log 4\pi\right] \\ &+ \log\frac{m^2(\phi)}{\mu^2} - \frac{3}{2} + \mathcal{O}\left(\frac{n}{2}-2\right)\Bigg\}\,. \end{aligned} \tag{5.28}$$

Now renormalisation comes into place. Dimensional regularisation can be followed by $\overline{\text{MS}}$ renormalisation. This consists of subtracting the term proportional to

$$C_{UV} = \left[\frac{1}{2-\frac{n}{2}} - \gamma_E + log 4\pi\right]\,, \tag{5.29}$$

in the regularized potential Eq.(5.28). This divergent piece with the pole at n = 4 has to be absorbed by the counterterms. Details will not be given, see again [51] for more, but it is possible to find a regularised and renormalised zero temperature effective potential as

$$V(\phi) = V_0(\phi) + \frac{1}{64\pi^2} m^4(\phi)\left[\log\frac{m^2(\phi)}{\mu^2} - \frac{3}{2}\right]. \tag{5.30}$$

A second example of regularisation is cut-off regularisation. In this example we consider specifically the Standard Model one-loop potential, see [54] for more details. Here we regularize the theory with a cut-off Λ and impose the minimum at v = 246.22 GeV. The Higgs mass or in general the mass of any field that does the transition is assumed to not change with respect to their tree level values. This can be written down as

$$\begin{aligned} \left.\frac{d\left(V_1 + V_1^{c.t.}\right)}{d\phi}\right|_{\phi=v} &= 0\,, \\ \left.\frac{d^2\left(V_1 + V_1^{c.t.}\right)}{d\phi^2}\right|_{\phi=v} &= 0. \end{aligned} \tag{5.31}$$

One can write in this regularisation that

$$V_1(\phi) = \frac{1}{32\pi^2} \sum_{i=W,Z,t,h,\chi} n_i \left[m_i^2(\phi)\Lambda^2 + \frac{m_i^4(\phi)}{2}\left(\log\frac{m_i^2(\phi)}{\Lambda^2} - \frac{1}{2}\right)\right]. \tag{5.32}$$

Then, the finite zero temperature potential after cancelling the UV divergencies using the counter terms becomes

$$V(\phi) = V_0(\phi) + \frac{1}{64\pi^2}\sum_i \left\{m_i^4(\phi)\left(\log\frac{m_i^2(\phi)}{m_i^2(v)} - \frac{3}{2}\right) + 2m_i^2(v)m_i^2(\phi)\right\}. \tag{5.33}$$

This scheme of renormalisation and Eq.(5.33) will be the one that is used in this thesis.

The last thing to add to the finite temperature effective potential are the corrections coming from working with a finite temperature quantum field theory. This will be necessary since phase transitions happen at finite temperature. There will be thermal corrections V_T to the effective potential

$$V_{eff}(\phi, T) = V_0(\phi) + V_1(\phi) + V_T(\phi, T). \tag{5.34}$$

It can be found that for bosons the thermal part of the potential can be written as

$$V_T = \int \frac{d^3p}{(2\pi)^3}\left[\frac{\omega}{2} + \frac{1}{\beta} log(1 - e^{-\beta\omega})\right], \tag{5.35}$$

where the first part of the integral is the one-loop effective potential at zero temperature, to prove this, see [51], $\beta = 1/T$ and ω is defined as $\omega^2 = \vec{p}^2 + m^2(\phi)$, with $m^2(\phi)$ the shifted mass. The thermal correction to the potential can also be written down for fermions, however this is not relevant for the minimal model of this thesis, since there are no fermions that can give corrections to the potential. The second, temperature dependent part coming from bosons can be written as

$$\frac{1}{\beta}\int \frac{d^3p}{(2\pi)^3} \log\left(1 - e^{-\beta\omega}\right) = \frac{1}{2\pi^2\beta^4} J_B\left[m^2(\phi)\beta^2\right], \tag{5.36}$$

where

$$J_B\left[m^2\beta^2\right] = \int_0^\infty dx\, x^2 \log\left[1 - e^{-\sqrt{x^2+\beta^2 m^2}}\right], \tag{5.37}$$

is the thermal bosonic function J_B. There exists a high-temperature expansion of this function, which can be very useful for practical applications. It is given by

$$\begin{aligned} J_B\left(m^2/T^2\right) = &-\frac{\pi^4}{45} + \frac{\pi^2}{12}\frac{m^2}{T^2} - \frac{\pi}{6}\left(\frac{m^2}{T^2}\right)^{3/2} - \frac{1}{32}\frac{m^4}{T^4}\log\frac{m^2}{a_b T^2} \\ &- 2\pi^{7/2}\sum_{\ell=1}^{\infty}(-1)^{\ell}\frac{\zeta(2\ell+1)}{(\ell+1)!}\Gamma\left(\ell+\frac{1}{2}\right)\left(\frac{m^2}{4\pi^2T^2}\right)^{\ell+2}, \end{aligned} \tag{5.38}$$

where a_b = $16\pi^2$exp(3/2-2γ_E) and ζ is the Riemann zeta-function. In section 6.2, this particular case is investigated. Here, we end our discussion of the finite temperature effective potential and we continue now by studying phase transitions themselves.

5.5 Phase Transitions

In the previous section, the one-loop and thermal corrections to the tree level potential were examined such that the concept of the finite temperature effective potential is clearly defined. The specific form of the potential can lead to phase transitions. These transitions exist in two types, first-order phase transition which will be of interest in this thesis or second-order phase transitions. These two types will be illustrated with an example below [51, 52].

A second-order phase transition can be investigated using the following general toy model potential

$$V(\phi, T) = D(T^2 - T_0^2)\phi^2 + \frac{\lambda(T)}{4}\phi^4, \tag{5.39}$$

where D and T_0^2 are constants and λ is a slowly varying function of T. In the case of a positive mass term at zero temperature, the minimum of the potential is at ϕ = 0, that point is stable and corresponds to the vacuum state. However in the toy model studied here at zero temperature, the toy model potential has a negative mass term, hence ϕ =

0 is an unstable state. In the case of the negative mass term, the state which is the true minimum and therefore favoured to $\phi = 0$ is $\phi(0) = \pm\sqrt{\frac{2D}{\lambda}}T_0$, where the symmetry $\phi \to -\phi$ is broken, in a similar way to the Brout-Englert-Higgs mechanism [55, 56].

At a finite temperature, this potential has two stationary points given by $\phi(T) = 0$, the origin, and

$$\phi(T) = \sqrt{\frac{2D(T_0^2 - T^2)}{\lambda(T)}}. \tag{5.40}$$

These points correspond to the local extrema of the potential. The point is then to find the temperature at which ϕ = 0 starts becoming a local maximum. From Eq.(5.40), it is clear that T_0 is exactly this temperature. It is called the critical temperature. Therefore at $T < T_0$, the origin becomes a maximum and $\phi(T) \neq 0$ is now the true minimum of the potential. This type of phase transition is called second order, because there is no barrier between the two phases, $\phi = 0$ and Eq.(5.40). Such a potential is shown in Figure 5.7. The interesting dynamics involving bubbles and leading to a SBGW happens instead in first order phase transitions, which is investigated in the following section.

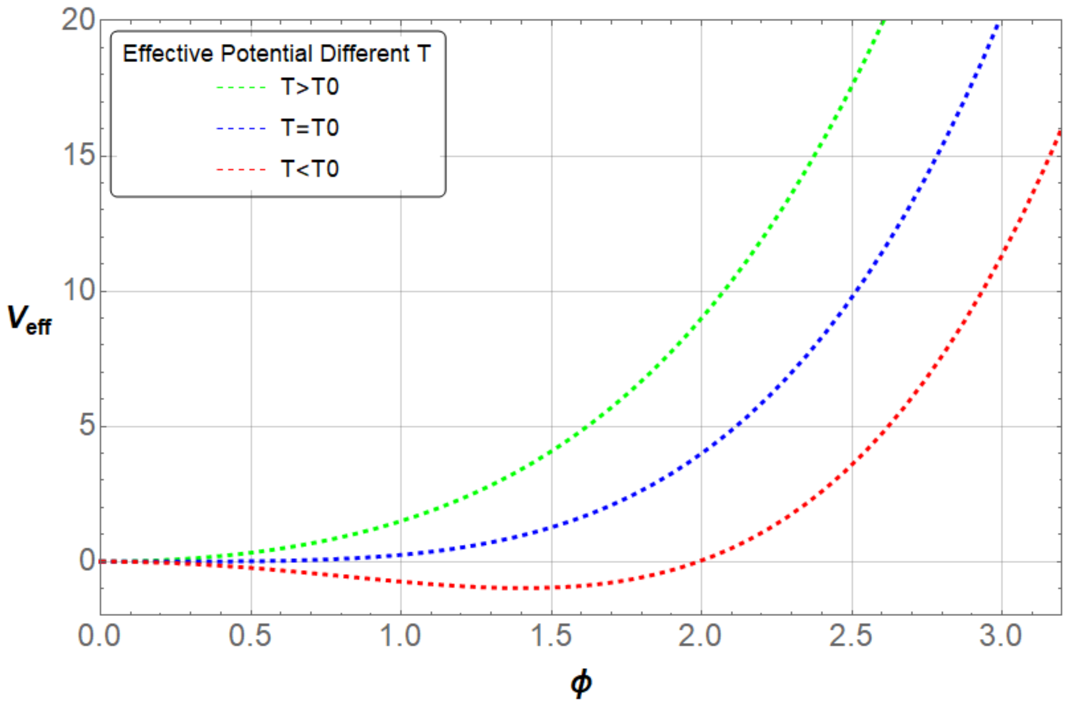

Figure 5.7: This shows the effective potential of the toy model for a second-order phase transition, Eq.(5.39), for different values of the temperature. One for a higher temperature, one for the critical temperature and one for a lower temperature. As seen by the two lower temperatures, there is never a barrier present in the potential for this toy model, which is characteristic for a second-order phase transition. To plot this potential, the constants D, T_0 and λ are taken to be 1.

5.5.1 First Order Phase Transition and the Effective Potential

As mentioned before, the dynamics of a phase transition are governed by the finite-temperature effective potential. For first-order phase transitions or FOPT, there is a barrier between the true vacuum, which is the broken phase, and the false vacuum or the unbroken phase. An example for a FOPT potential toy model is given by

$$V(\phi, T) = \frac{1}{2}\gamma(T^2 - T_0^2)\phi^2 - \frac{1}{3}AT\phi^3 + \frac{1}{4}\lambda\phi^4\,, \tag{5.41}$$

where $\phi \geqslant 0$ and γ, A and λ are strictly positive. The big difference between this toy model and Eq.(5.39) is the emerging of a new cubic term in the potential. This cubic term is responsible for the barrier in the potential at finite temperature. It is directly dependent on the temperature and goes away at zero temperature, which means that the barrier also disappears at zero temperature. There, Eq.(5.39) is recovered.

The potential is shown in Figure 5.8 for different values of T. Table 5.1 gives the parameters for which this figure was made. For very high temperatures T, the potential has a true minimum at $\phi = 0$, where $V(\phi) = 0$. This is the unbroken phase, which is represented as the blue line of the plot.

As the temperature is lowered, a second extremum of the potential appears at a temperature T_1 given by

$$T_1^2 = \frac{T_0^2}{1 - A^2/(4\lambda\gamma)}\,, \tag{5.42}$$

which is represented by the red line in the figure.

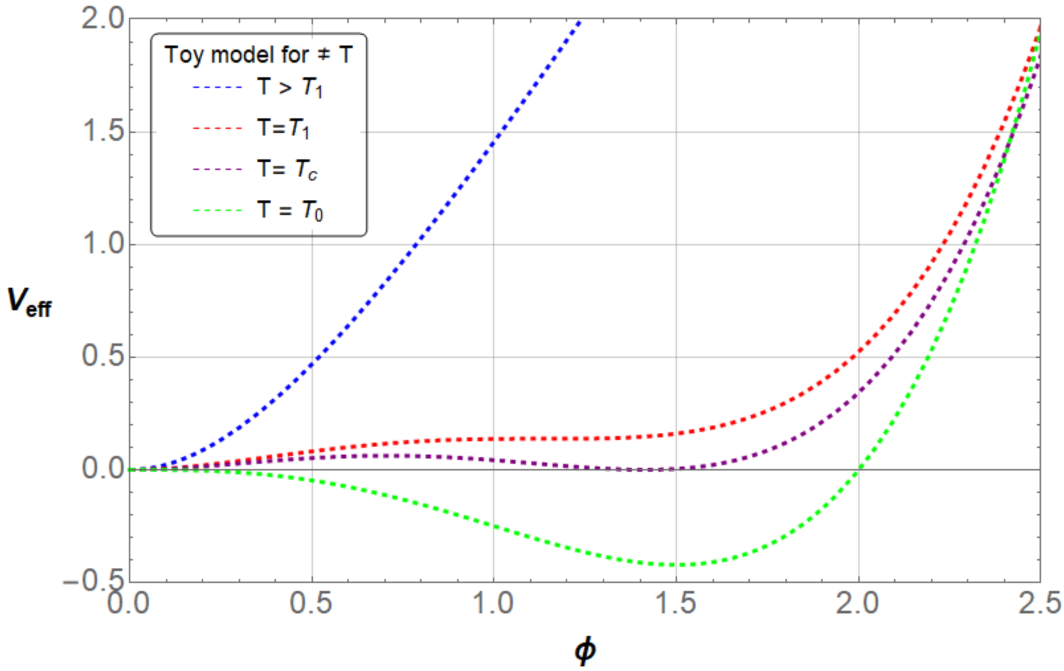

Figure 5.8: This plot shows the potential $V(\phi, T)$ for a first-order phase transition in the toy model, Eq.(5.41), for different values of T, starting from a higher temperature all the way to T_0 passing T_1, the point where a second extremum comes into play, and the critical temperature T_c, where the vacua become degenerate. One can clearly see a barrier forming in the potential when looking at T_c. This barrier is required for the first-order phase transition.

The second extremum is then situated at $\phi = \phi_1 = AT_1/(2\lambda)$ and $V(\phi_1) > 0$. When the temperature decreases even further, the extremum splits into a local maximum and a local minimum. The value of the potential at the local minimum keeps decreasing when the temperature drops until this minimum of the potential become degenerate with the other minimum at $\phi = 0$. This happens at the critical temperature

$$T_c^2 = \frac{T_0^2}{1 - 2A^2/(9\lambda\gamma)}\,. \tag{5.43}$$

	γ	T_0	A	λ	T_c	T_1
Value	1	1	1.5	1	$\sqrt{2}$	2.29

Table 5.1: The parameters shown here are used to plot the potential of the toy model given in Figure 5.8. On the left side of the double line, the input parameters are given, while on the right of it the parameters computed from these inputs are given. This notation is followed in all other tables as well. To find T_1 and T_c, Eqs. (5.42) and (5.43) are used respectively.

Note that the critical temperature here it is not simply given by T_0 as in the case of the second-order phase transition, here it is denoted as T_c instead. The potential at the critical temperature is the purple line in the plot for the toy model, where it is clear that the two minima now have the same value.

Lowering the temperature even more, $T < T_c$, then the minimum at ϕ_1, which was local, becomes the true minimum of the potential. The end of the analysis of the temperature dependence of the potential comes when we reach $T = T_0$. Here the extremum in $\phi = 0$ becomes a local maximum. This is the green line in the plot. It is possible to lower the temperature even further, but no other interesting features occur.

The described toy model highlights the central property of a first order phase transition, namely that in a certain temperature range there exist two minima of the potential separated by a barrier. In section 6.2, we will see how the temperature evolution of the scalar ϕ in the dark matter minimal model can be described by a semi-analytical potential which can be mapped to this very toy model.

The Universe during its evolution undergoes a number of phase transitions that can be a smooth crossover (=second-order) or first-order phase transitions. For example, the most recent one took place at the QCD scale, with a critical temperature $T_c \sim 150$ MeV. Above this temperature quarks and gluons are not confined into hadrons and form a quark-gluon plasma. At earlier times there is the electroweak phase transition at the critical temperature $T_c \sim 100$ GeV. If T goes below T_c, the Higgs field will take on a non-zero vacuum expectation value, thereby making the gauge W and Z bosons, quarks and leptons massive and breaking the $U(1)_Y \times SU(2)_L$ symmetry. It is possible that at even higher temperatures, there have been other unknown phase transitions, for example at the grand unified energy scale.

Focusing on the possibility of generating a SBGW during the phase transition, the interesting case is when the phase transition is first order. We examine the electroweak phase transition. The order of the phase transition depends on the value of the underlying particle physics model, in this case the Standard Model. Especially, the Higgs mass is of importance. A couple of years ago, this mass was measured at the LHC to be $m_H \sim 125$ GeV [57]. This is bad news for the first-order phase transition possibilities at the electroweak scale. For this particular value of the Higgs mass, there is no first-order phase transition and no GW production. Instead, there is a second-order phase transition, also called a smooth crossover at a temperature T = 150.5 $\pm$ 1.5 GeV. If the Higgs mass would have been smaller, $m_H < 80$ GeV, perhaps there could have been a FOPT [58].

5.5.2 Bubble dynamics

In this section FOPTs will be investigated in more detail. Starting from the concept of tunneling at zero and finite temperature, we go to the bounce action. From the bounce action, the nucleation condition can be computed as well as parameters α and β/H_* which will be useful for calculating the GW spectrum coming from a FOPT.

The question in this section will be: how and when does the FOPT take place? First we need to look at how it is possible to tunnel through the barrier of the potential in finite temperature quantum field theory from the false vacuum to the true vacuum. As a small detour and preparation for the finite temperature, we first examine tunneling at zero temperature.

Zero temperature tunneling To start the discussion of tunneling the most simple general example that can be imagined with the right properties is considered. The simplest theory is a scalar theory in zero temperature quantum field theory with a certain potential $V(\phi)$.

Consider a scalar field theory in Minkowski space

$$S_M = \int d^4x \left[-\frac{1}{2}\eta^{\mu\nu}\partial_\mu\phi\partial_\nu\phi - V(\phi) \right]. \tag{5.44}$$

Then choose a potential that has a false vacuum in ϕ = 0, with $V(\phi) = 0$ and a true vacuum at $\phi = \phi_0 > 0$, where $V(\phi_0) < 0$. It is possible to perform a Wick rotation, introducing Euclidean time $\tau = it$. Then $d^4x = -id\tau d^3x = -i(d^4x)_E$. If the Euclidean action is defined as $S_E = -iS_M$, then

$$S_E = \int d^4x_E \left[\frac{1}{2}\partial_\mu\phi\partial_\mu\phi + V(\phi) \right]. \tag{5.45}$$

We want to find the equation of motion corresponding to this action and the solution, keeping in mind the boundary condition

$$\lim_{\tau\to\pm\infty} \phi(\tau, x) = 0. \tag{5.46}$$

We also impose

$$\lim_{|x|\to\infty} \phi(\tau, x) = 0\,, \tag{5.47}$$

to make sure the action cannot be infinite. Then choose a random point in Euclidean space as the origin for the coordinate system and define a radial coordinate $\rho = (\tau^2 + x^2)^{1/2}$. The solutions of the equations of motion or e.o.m. will come in the form $\phi = \phi(\rho)$. The action then reads

$$S_E = 2\pi^2 \int_0^\infty d\rho\rho^3 \left[\frac{1}{2}\left(\frac{d\phi}{d\rho}\right)^2 + V(\phi) \right], \tag{5.48}$$

such that the e.o.m. become

$$\frac{d^2\phi}{d\rho^2} + \frac{3}{\rho}\frac{d\phi}{d\rho} = V'(\phi). \tag{5.49}$$

The boundary conditions are simplified into one

$$\lim_{\rho\to\infty} \phi(\rho) = 0. \tag{5.50}$$

It is also required that the solution at the origin is regular, which means that

$$\left.\frac{d\phi}{d\rho}\right|_{\rho=0} = 0. \tag{5.51}$$

When looking at Eq.(5.49), the e.o.m can be seen as the motion of a particle in one dimension described by the coordinate ϕ, with ρ being some kind of time coordinate, moving in a potential $-V(\phi)$, as shown in Figure 5.9.

The particle is also under the influence of a damping force $-\eta(\rho)v$, where $v = d\phi/d\rho$ is the velocity and $\eta(\rho) = 3/\rho$ is the friction coefficient, depending on ρ itself. Looking at the boundary conditions, the particle must start at a time $\rho = 0$ with a velocity zero from an initial position ϕ_i, such that at $\rho \to \infty$, ϕ goes to zero. Since friction is present, the initial energy must be higher than zero. The initial position of the field then can be determined by integrating Eq.(5.49) numerically. This numerical process will assign a value ϕ in the range between ϕ_e and ϕ_0, as shown in Figure 5.9, using an under-shooting/over-shooting procedure [59]. This range of ϕ is chosen because the friction terms ensures that the initial energy must be bigger than zero.

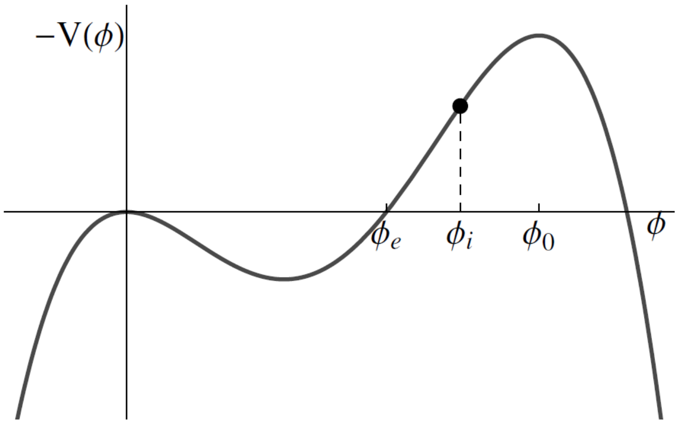

Figure 5.9: This shows the potential $-V(\phi)$. It also shows the range of possible ϕ to choose for the under-and over-shooting procedure. The two boundaries of the range are ϕ_e and ϕ_0. In between these two, the procedure chooses a random value of ϕ to try and calculate the bounce solution. The ideal point to start at is ϕ_i at which ϕ goes to zero for $\rho \to \infty$, because this is exactly the bounce solution. Figure from [52].

If we would choose an initial position, such that there is not enough energy to reach $\phi = 0$, the solution bounces back while oscillating around the minimum of $-V$. It is also possible to choose an initial position such that the solution overshoots and reaches the region $\phi < 0$, which leads to $\phi \to -\infty$. The bounce solution $\phi_b(\rho)$ for which $\phi = 0$ if $\rho \to \infty$ can be written as $\phi = \phi_b\left(\sqrt{-t^2 + r^2}\right)$, where $r = |x|$.

We can pick a fixed t, for example $t = 0$, and look at the dependence of ϕ on r. Then, at small r, ϕ is near the value ϕ_i and thus close to the true vacuum ϕ_0. As we increase r, the value of ϕ will evolve and eventually will reach $\phi = 0$, the false vacuum. This solution represents a nucleation bubble, where the field ϕ sits in the true vacuum in the inner region of the bubble and in the false vacuum in the outer region.

This bubble will expand in the false vacuum at the speed of light in the case of the zero temperature tunneling. The transition rate is then

$$\frac{\Gamma}{V} = Ae^{-S_b}, \tag{5.52}$$

where S_b is the Euclidean action, defined in Eq.(5.48), evaluated on the bounce solution ϕ_b and A is some prefactor, which is complicated to calculate and can be found in [52]. The next step is to examine the tunneling, but in the finite temperature regime.

Tunneling at finite temperature It is time to generalize the procedure in the previous paragraph to finite-temperature quantum field theory. This will be useful for the phase transitions happening in the minimal model, since they happen in the Early Universe at a certain finite temperature. Therefore, the potential must be replaced by the effective potential at finite temperature $V(\phi, T)$ as was introduced in section 5.4. The action is given by

$$S_4[\phi] = \int_0^{1/T} d\tau \int d^3x \left[\frac{1}{2}\partial_\mu\phi\partial_\mu\phi + V(\phi, T) \right] . \tag{5.53}$$

We want to look at the limit where T is large compared to $1/R$, the inverse of the radius of the nucleation bubble. Hence, the dependence of ϕ on Euclidean time becomes negligible, therefore

$$S_4[\phi] \backsimeq \frac{1}{T} S_3[\phi] , \tag{5.54}$$

where

$$S_3[\phi] = \int d^3x \left[\frac{1}{2} \left(\partial_i\phi\right)^2 + V(\phi, T) \right] , \tag{5.55}$$

and $\phi = \phi(x)$. In this case, we will try to find a solution of the form $\phi = \phi_b(r)$, where $r = |x|$. The action reduces to

$$S_3 = 4\pi \int_0^\infty dr r^2 \left[\frac{1}{2} \left(\frac{d\phi}{dr} \right)^2 + V(\phi, T) \right] , \tag{5.56}$$

with the equation of motion

$$\frac{d^2\phi}{dr^2} + \frac{2}{r}\frac{d\phi}{dr} = \frac{dV(\phi, T)}{d\phi} . \tag{5.57}$$

The boundary conditions can be written as $\lim_{r\to\infty} \phi(r) = 0$ and in order to have regularity at the origin we need

$$\left. \frac{d\phi}{dr} \right|_{r=0} = 0 . \tag{5.58}$$

The transition rate meanwhile is now given by

$$\frac{\Gamma}{V} \backsimeq cT^4 e^{-S_{3,b}(T)/T} , \tag{5.59}$$

where $S_{3,b}(T)/T$ is the action $S_3[\phi, T]$ evaluated on the bounce solution $\phi_b(r)$ and c is $\mathcal{O}(1)$. When looking at Eq.(5.52), the prefactor A is now approximated by $c \times T^4$ [52]. The next step of the story is investigating when a nucleation bubble is formed and how to calculate the nucleation temperature.

Nucleation condition As mentioned before, the process starts from large temperatures where the field ϕ sits at the minimum of $\phi = 0$. When the Universe cools down and $T < T_c$, this minimum becomes metastable and the Universe is in a false vacuum. It is possible to transition to the true vacuum via quantum or thermal tunneling. This creates regions or bubbles of true vacuum, in a process called bubble nucleation. The nucleation of a bubble results in an energy gain $(4\pi/3)r^3\Delta\rho_{vac}(T)$, where r is the bubble radius and $\Delta\rho_{vac}(T)$ is the energy difference between the true vacuum and the false vacuum. However, there is a loss of energy due to the surface tension of the bubble given by $4\pi r^2\sigma$. Therefore, there is a critical radius $r_c(T) = 3\sigma/\Delta\rho_{vac}(T)$, such that bubbles with a smaller radius disappear while bubbles with a bigger radius survive and expand.

The probability of nucleation of such a large bubble is small and can be quantified by the nucleation rate $\Gamma(T)$, the transition rate from the false to the true vacuum. But if one waits long enough, such a transition to the true vacuum will happen eventually. However in cosmology, there is a timescale to which we should compare the nucleation rate $\Gamma(T)$ due to the expansion of the Universe, namely the Hubble expansion rate $H(T)$.

If the nucleation rate for bubbles is smaller than $H(T)$, the Universe will have cooled down too much before the nucleation has a significant chance of happening. If $\Gamma(T)$ never becomes as large as $H(T)$, then at $T = T_0$, the field ϕ will roll smoothly from the false vacuum, which now is a local maximum, to the true vacuum. This is a second-order phase transition.

A first-order phase transition will happen when $\Gamma(T)$ becomes as large as $H(T)$ at a temperature T_{nuc}, the nucleation temperature, in the temperature range $T_0 < T_{nuc} < T_c$. Tunneling will happen in that case.

At a time t the rate of bubble nucleation in a Hubble volume is $(\Gamma/V) \times H^{-3}(t)$. The time t_{nuc} at which the phase transition takes place can be computed by requiring that the number of bubbles nucleated from time 0 to t_{nuc} is of order 1

$$\int_0^{t_{nuc}} dt \frac{\Gamma}{VH^3(t)} = \mathcal{O}(1). \tag{5.60}$$

It is possible to transform the variable of this integral from t to T, using $T \approx 1/a$, such that dT/T = - $H\,dt$. We also fill in H, see Eq.(2.7), and the phase transition temperature T_{nuc} is found by computing

$$\int_{T_{nuc}}^{\infty} \frac{dT}{T} \left(\frac{45}{4\pi^3 g_*(T)}\right)^2 \left(\frac{M_{Pl}}{T}\right)^4 e^{-S_3(T)/T} = \mathcal{O}(1). \tag{5.61}$$

However, it will be easier to simplify the integral because it is dominated at the nucleation temperature $T = T_{nuc}$. This will become clear later on when we look at the form of $S_3(T)/T$. This means that Eq.(5.61) is approximated as

$$\left(\frac{45}{4\pi^3 g_*(T_{nuc})}\right)^2 \left(\frac{M_{Pl}}{T_{nuc}}\right)^4 e^{-S_3(T_{nuc})/T_{nuc}} = \mathcal{O}(1). \tag{5.62}$$

It is possible to set $g_*(T_{nuc})$ at its highest value in the minimal model, which would be 113.75 as mentioned before. However this is still small compared to the Planck Mass, therefore one is able to write Eq.(5.62) as

$$\frac{S_3(T_{nuc})}{T_{nuc}} \backsimeq 4 \log\left(\frac{M_{Pl}}{T_{nuc}}\right). \tag{5.63}$$

This equation will be used to compute the nucleation temperature by trying to find the intersection between the bounce action on the left hand side and the log on the right hand side of the equation. However this does depend on the energy scale we are looking at, since M_{Pl} has the dimensions of a mass. Until now everything could have been done dimensionless. Hence the nucleation temperature will depend on which scale is investigated. In the thesis, three scales will be investigated corresponding to different regimes of dark matter production and the nucleation condition will be affected by the variation in these scales.

The vacuum energy density associated with the transition is

$$\rho_* = \left[-V[\eta(T), T] + T\frac{d}{dT}V[\eta(T), T]\right]_{T=T_{nuc}}, \tag{5.64}$$

where $\eta(T)$ is the vacuum expectation value of the scalar field at the true vacuum depending on the temperature. It is convenient to normalize this quantity to the radiation energy density

$$\alpha = \frac{\rho_{vac}}{\rho_{rad}} = \frac{30\rho_*}{\pi^2 g_*(T_{nuc})T_{nuc}^4}, \tag{5.65}$$

where we used that $\rho_R = g_* \pi^2 T^4/30$. The parameter α quantifies the strength of the phase transition.

Another important parameter is the bubble nucleation rate

$$\frac{\Gamma(t)}{V} = \frac{\Gamma_{nuc}}{V} e^{\beta(t-t_{nuc})}\,, \tag{5.66}$$

where t_{nuc} is the time of transition at which the rate is Γ_{nuc}. Since β has dimension t^{-1}, the relevant to be computed parameter will be β/H_*, where H_* = $H(T_{nuc})$.

Until now, it was assumed that the Universe only has a radiation contribution, hence it is possible to fill in the Hubble parameter in Eq.(5.60) to get Eq.(5.61). However, one needs to take the effect of changing the vacuum on the Hubble parameter into account. This leads to the following definition

$$H(T) = \sqrt{\frac{1}{3M_{Pl}^2}\left(\frac{T^4}{s^2} + \Delta V\right)}\,, \tag{5.67}$$

where $s = 30/(\pi^2 g_*)$ and ΔV is the difference between the zero temperature potential at the false vacuum and the zero temperature potential at the true vacuum. The Hubble parameter now has changed contrary to before where we used Eq.(2.7) to insert H into Eq.(5.60). Keeping the Hubble parameter present in Eq.(5.60) and going through the same process again of computing the integral, approximating it at the nucleation temperature with this new Hubble parameter leads to a change of Eq.(5.63) into

$$\frac{S_3(T_{nuc})}{T_{nuc}} \backsimeq 4\log\left(\frac{T_{nuc}}{H(T_{nuc})}\right). \tag{5.68}$$

This is the nucleation condition that is used for the remainder of the thesis.

Since we have now determined T_{nuc}, it is possible to calculate α, see Eq.(5.65) and β, first introduced in Eq.(5.66). β represents the inverse duration of the phase transition. The way to compute β is by expanding the the bounce action around the transition time t_{nuc}

$$\frac{S_{3,b}(T)}{T} \backsimeq \left(\frac{S_{3,b}(T)}{T}\right)_{t=t_{nuc}} + (t-t_{nuc})\frac{d}{dt}\left(\frac{S_{3,b}(T)}{T}\right)_{t=t_{nuc}}. \tag{5.69}$$

Then, β is defined as

$$\beta = -\frac{d}{dt}\left(\frac{S_{3,b}(T)}{T}\right)_{t=t_{nuc}} \backsimeq \frac{\dot{\Gamma}}{\Gamma}\,, \tag{5.70}$$

see Eq.(5.59) for the second equality. We switch again from t to T and we find

$$\frac{\beta}{H_*} = T_{nuc}\frac{d}{dT}\left(\frac{S_{3,b}(T)}{T}\right)_{T=T_{nuc}}. \tag{5.71}$$

To compute β/H_*, one needs to know the nucleation temperature T_{nuc}, the potential $V(\phi, T)$ and how the action depends on T in the vicinity of T_{nuc}, while for α one only needs knowledge about the first two concepts.

The concepts introduced in the paragraphs above will allow us to study FOPT in the Early Universe and the bubble dynamics coming from these phase transitions. To illustrate the concepts, a return to the toy model introduced in Eq.(5.41) is useful. Using the equations and approaches mentioned above, the bounce action and the nucleation temperature can be calculated for this toy model. The bounce action can be calculated using the Mathematica package *FindBounce* [60]. The result is given in Figure 5.10 using the parameters of Table 5.2. Then the nucleation temperature can be found by solving Eq.(5.68), which amounts to finding the intersection between the bounce action and the log, representing the solution of Eq.(5.68). The value of the nucleation temperature T_{nuc} is given by 1.96 $\times 10^3$ GeV in this case.

In the toy model, one can calculate α and β/H_* using T_{nuc}. We find that α = 0.012 and $\beta = 1128.3$. The concepts outlined in this section will be important when examining how to calculate the gravitational wave spectrum in the next section.

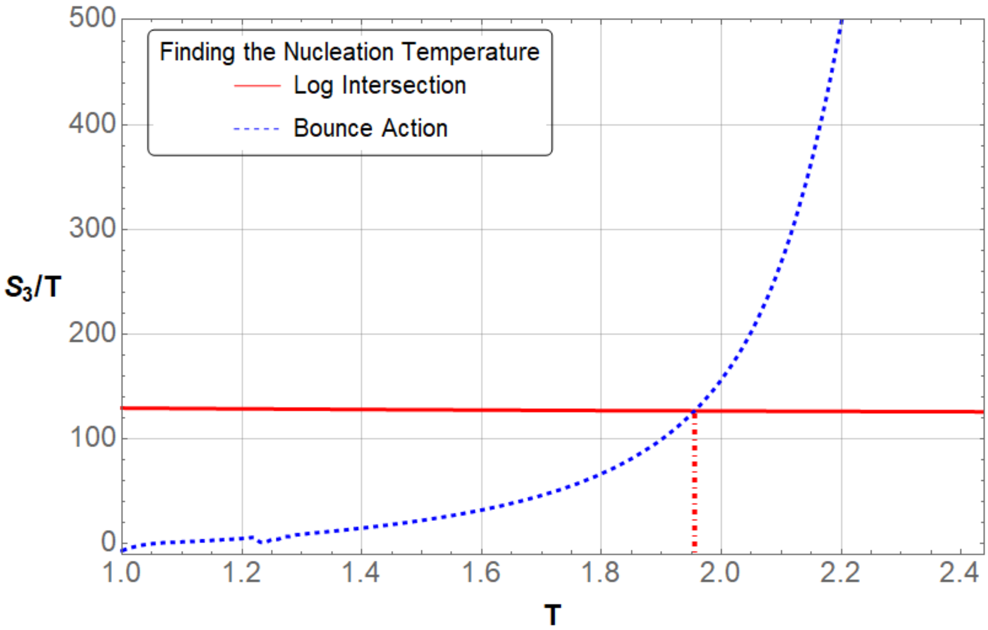

Figure 5.10: This shows the bounce action calculated for the toy model of Eq.(5.41) with the parameter values from Table 5.2 as the blue dashed line. It also shows the way the nucleation temperature is calculated. The intersection between the bounce action and the red horizontal line, which is Eq.(5.68), will define the nucleation temperature. This temperature is represented by the red vertical dotdashed line. The scale is this case is 10^3 GeV.

	λ	T_0	A	γ	T_c	T_{nuc}
Value	0.6	1	1.5	1	$\sqrt{6}$	1.96 $\times 10^3$ GeV

Table 5.2: To give an example for the bounce action and how to compute the nucleation temperature in the toy model, the parameters in this table are chosen. The nucleation temperature is computed using Eq.(5.68).

5.6 GW Spectrum

In this section, we will try to find formulas for the frequency spectrum of the gravitational waves coming from the bubbles [61].

Before we begin, one last important parameter should be introduced, namely the kappa-parameters

$$\kappa_v = \frac{\rho_v}{\rho_{vac}}, \ \kappa_\phi = \frac{\rho_\phi}{\rho_{vac}}. \tag{5.72}$$

These give the fraction of vacuum energy that gets converted into bulk motion of the fluid ρ_v as kinetic energy and into the energy of the scalar field ρ_ϕ. As a last comment, the bubble wall velocity in the rest frame of the plasma far away from and around the bubble will be denoted as v_w.

Bubbles that are spherical will not produce gravitational waves. It is only in processes coming from the collision of bubbles that GWs will be created. There are three processes that can be involved in the production of GW's:

- Collisions of bubbles and shocks in the plasma. These are generally treated with the envelope approximation.
- Sound waves that arise in the plasma after the collision but before the expansion has dissipated the kinetic energy in the plasma.
- Magnetohydrodynamic turbulence, which we will neglect in this thesis.

The contributions can all combine such that

$$h^2\Omega_{GW} \simeq h^2\Omega_\phi + h^2\Omega_{sw} + h^2\Omega_{MHD} \sim h^2\Omega_{sw}\,, \tag{5.73}$$

where Ω_{GW} is defined in Eq.(5.10). The main production process for gravitational waves in the model considered in the thesis is assumed to be the sound waves coming from the plasma surrounding the bubbles. We focus now on on that specific production process.

Sound waves: Bulk motion in the fluid can occur as sound waves. For generic values of v_w, the numerical results are fitted by [62]

$$h^2\Omega_{\rm sw}(f) = 2.65\times 10^{-6}\left(\frac{H_*}{\beta}\right)\left(\frac{\kappa_v\alpha}{1+\alpha}\right)^2\left(\frac{100}{g_*}\right)^{\frac{1}{3}} v_w S_{\rm sw}(f)\,, \tag{5.74}$$

where κ_v is defined in Eq.(5.72). The spectral shape $S_{sw}(f)$ is found using simulations [62]

$$S_{\rm sw}(f) = (f/f_{\rm sw})^3\left(\frac{7}{4+3\,(f/f_{\rm sw})^2}\right)^{7/2}\,, \tag{5.75}$$

where f_{sw} is the peak frequency. An estimate shows that after redshift the peak frequency becomes [62]

$$f_{\rm sw} = 1.9\times 10^{-2}{\rm mHz}\frac{1}{v_w}\left(\frac{\beta}{H_*}\right)\left(\frac{T_*}{100{\rm GeV}}\right)\left(\frac{g_*}{100}\right)^{\frac{1}{6}}\,. \tag{5.76}$$

The dependence on T_{nuc} in the equation for the peak frequency is important for the computations later on. It is there that the scale of interest plays a significant role for the realisation of the GW signal.

On a final note, the form of κ_v is specified. Once again this can be found in [61]. The bubbles will expand in a plasma thereby experiencing friction. This friction works against the expanding bubble, which means that there could be a terminal velocity for the bubbles. Such bubbles are non-runaway bubbles. Runaway bubbles do have an ever increasing velocity until the speed of light, however the runaway bubbles have most of their energy transferred into bubble collisions due to the energy stored in the walls of the bubbles which can also lead to the production of gravitational waves. This will not be considered in this thesis since we look at GW production where sound waves are the dominant source.

Even in a non-runaway context in this model, the bubble will still have a relativistic velocity. Therefore, v_w will be taken to be 1 from now on. In the case of a relativistic terminal velocity, the most important contribution to the GW spectrum for non-runaway bubbles will come from sound waves and then κ_v will be given by [62]

$$\kappa_v = \alpha(0.73 + 0.083\sqrt{\alpha} + \alpha)^{-1}. \tag{5.77}$$

This final formula gives a nice conclusion to the investigation of the GW spectrum and the toy model. Since all parameters needed to produce a spectrum have been examined, it is possible to compute the spectrum using Eq.(5.74) for the toy model. This can be seen in Figure 5.11. The parameters used to calculate this spectrum can be found in Table 5.1 and Table 5.3. In the plot, the spectrum is plotted in red together with three other dotted line that represent the sensitivity of upcoming experiments. For more information about these curves, see section 5.3. The orange line represents the sensitivity of BBO experiment. It seems that this detector would be able to catch the signal coming from the toy model, since the GW spectrum just crosses the sensitivity line. This effect will hopefully return when looking at the GW spectra in the actual dark matter minimal model from this thesis. These spectra are computed and examined in the next section.

	α	β/H_*
Value	1.16×10^{-2}	1128.3

Table 5.3: Using the parameters from Table 5.1, Eq.(5.65) and Eq.(5.71) we calculate α and β/H_* found in this table. From these parameters the GW spectrum of the toy model, see Eq.(5.74) can be calculated.

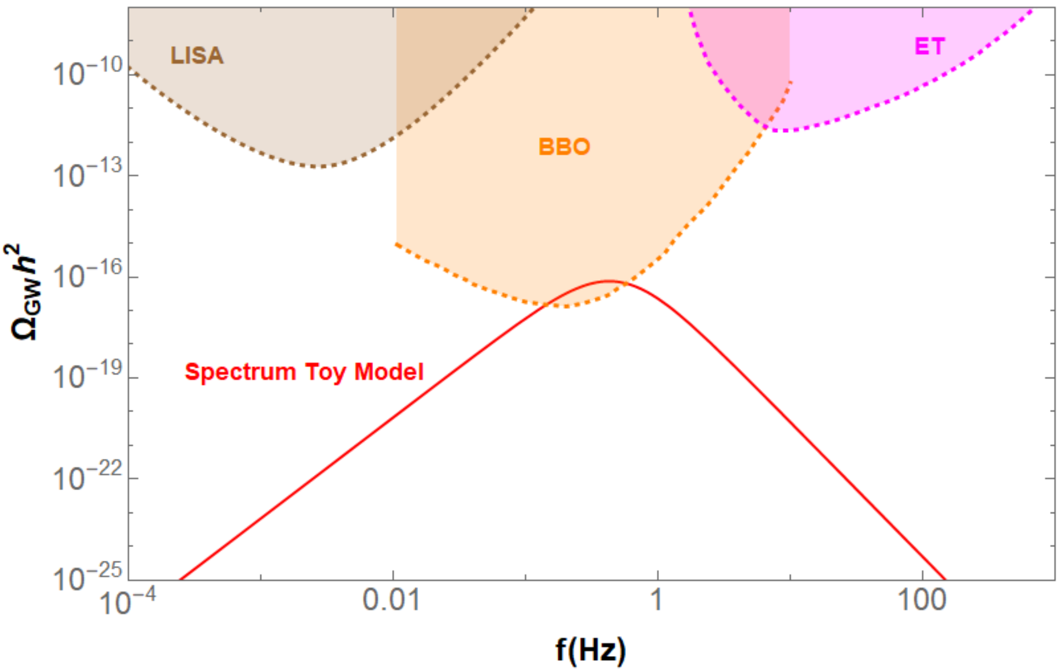

Figure 5.11: This figure shows the computed Ω_{GW} spectrum coming from a first-order phase transition when considering the toy model from Eq.(5.41) in red together with the PLS curves of three experiments, BBO in orange, LISA in brown and Einstein Telescope in magenta.

6 Gravitational Waves in a Minimal Dark Matter Model

Following the discussion of the previous section, we now move to investigate the possible phase transition that can occur in the dark matter minimal model model explored in this thesis given by the Lagrangian Eq.(3.3). We start by computing the potential for the minimal dark matter model and then we calculate T_c and T_0. After that, the bounce action following from the potential can be computed as well. Subsequently, the nucleation temperature is also calculated. However to compute this temperature, one needs to specify the scale at which you are working. In the calculations below, we will work with three different scale corresponding to three different regimes of dark matter production we have discussed in section 2.4. The next step is calculating α and β/H_* from which the GW spectrum resulting from the first order phase transition can be computed. There will also be an analysis of the parameter space from the minimal model.

6.1 Phase transition in the minimal dark matter model

Effective potential, phase transition and bounce action The first required ingredient is the finite temperature effective potential for the scalar ϕ. The thermal and quantum effects which shape the potential depend on the particles interacting with the ϕ particle. Since the ϕ particle is charged under the $U(1)_D$ symmetry, it will interact with the gauge boson of this symmetry, Z'. The self-interaction of ϕ will also be present. Hence there will be only bosons responsible for the one-loop and thermal corrections of the potential. In short, these will be the relevant interactions for these corrections to the potential in this model

$$\mathcal{L} \supset |\mathcal{D}_\mu \phi|^2 - \frac{1}{4} F'_{\mu\nu} F^{\mu\nu\prime} - \mu^2 |\phi|^2 + \lambda |\phi|^4 \,, \tag{6.1}$$

where $|\phi|^2 = \phi^* \phi$. We then define $|\phi| = \frac{\rho}{\sqrt{2}}$ and ρ as the modulus of the scalar complex field with a normalisation factor $\sqrt{2}$ to keep the kinetic term of the Lagrangian canonical. The ρ notation will be used for the remainder of this section. As a reminder, the covariant derivative in the kinetic term is defined as $\mathcal{D}_\mu = \partial_\mu - i g_D Z'_\mu$ and $F'_{\mu\nu}$ is the general field strength tensor for the Z' boson. All other terms where the effect of the first-order phase transition could play a role, such as the new higher-dimensional operator, are assumed to have negligible effects mostly due to small couplings. The quartic self-interaction of ϕ and in some sense also the mass term present in the tree-level potential will also have an effect on the finite temperature effective potential.

The effects of these two bosons can be plugged into Eq.(5.33) and Eq.(5.35) to obtain the one-loop and thermal corrections to the tree-level potential in Eq.(5.17) corresponding to these bosons. To do this, the masses of both bosons must be known. They can be written as

$$\begin{aligned} m^2_{Z'}(\rho, g_D) &= g_D^2 \frac{\rho^2}{2} \,, \\ m^2_\rho(\rho, \mu, \lambda) &= 3\lambda\rho^2 - \mu^2 \,, \end{aligned} \tag{6.2}$$

where ρ is the modulus of the complex field ϕ as defined before. These definitions follow from Eq.(5.20). One can immediately see that for example the Z' boson will be massless at high temperature, since there the ρ field sits in the minimum $\rho = 0$. However, when the ρ field will tunnel to the true vacuum of the effective potential at a lower temperature the Z' boson acquires a mass.

It all begins with the finite temperature effective potential. For the dark matter minimal model of the thesis we use the same form for the tree level potential as in Eq.(5.17), but now with the modulus ρ

$$V_0(\rho) = -\mu^2 \frac{\rho^2}{2} + \lambda \frac{\rho^4}{4}. \tag{6.3}$$

The one-loop correction is given by, see Eq.(5.33)

$$V_1(\rho) = \frac{1}{64\pi^2} \sum_{i=\rho,Z'} \left\{ n_i\, m_i^4\,(\rho) \left(\log \frac{m_i^2\,(\rho)}{m_i^2(v_\phi)} - \frac{3}{2} \right) + 2m_i^2(v_\phi) m_i^2\,(\rho) \right\}. \tag{6.4}$$

The thermal corrections in the minimal model are given by

$$V_T(\rho, T) = \frac{T^4}{2\pi^2} \left[n_\rho\, J_B[m_\rho(\rho)^2/T^2] + n_{Z'}\, J_B[m_{Z'}(\rho)^2/T^2] \right] , \tag{6.5}$$

where we take $n_\rho = 1$ and $n_{Z'} = 3$ from now on.

	μ	g_D	λ	T_0	T_c	T_1
Value	100	1.0	0.01	54	172	220

Table 6.1: These parameters are used to compute the finite temperature effective potential in Figure 6.1 where its dependence on the temperature is investigated. The three parameters T_0, T_c and T_1 are calculated using the finite temperature effective potential for the dark matter minimal model.

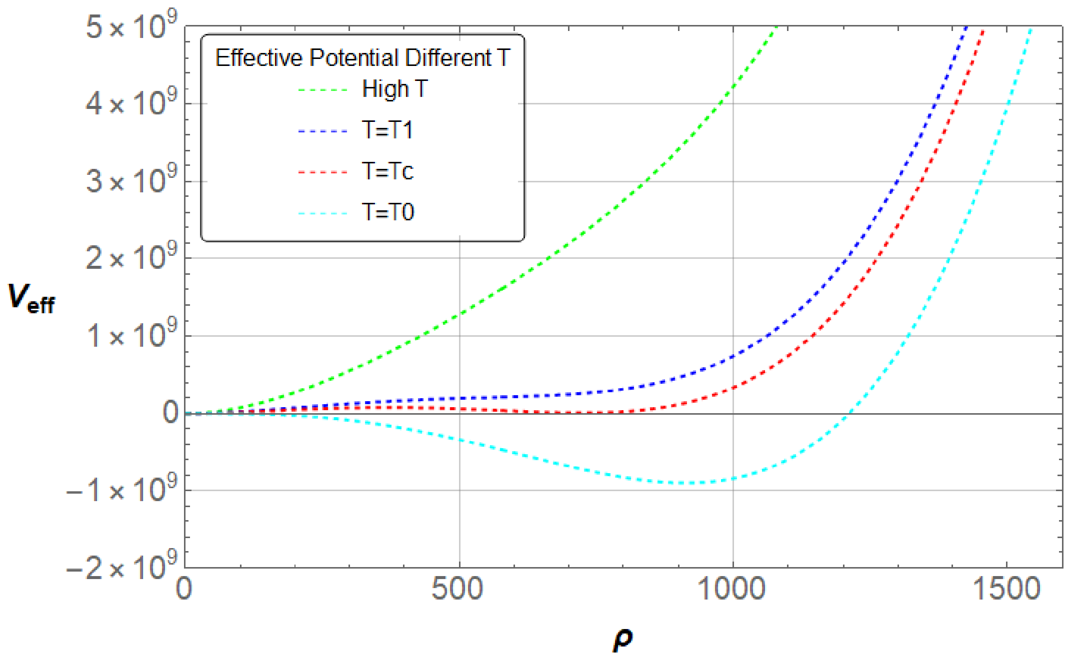

Figure 6.1: This shows the effective potential for the dark matter minimal model in the thesis for different values of T. The green line is at a high temperature where the potential only has a minimum at ρ = 0. Lowering the temperature leads us to T_1 where a second extremum appears as expected. From T_c onward the second extremum becomes the true vacuum and tunneling might occur. This ends at T_0, where the extremum in ρ=0 becomes a local maximum and a smooth crossover can be recovered if the tunneling has not yet taken place. It is also noticed that the position of the second extremum changes depending on the temperature, so this is another effect that needs to be taken into account.

To know the thermal corrections, one needs to calculate the thermal bosonic function, given in Eq.(5.37). Putting all these formulas together will give the finite temperature effective potential of the model which is shown in Figure 6.1 for a certain set of parameters, shown in Table 6.1.

The next step using the effective potential is to find the critical temperature T_c and T_0 of the potential, where T_c is the point at which the potential starts having degenerate minima. From that point on there is a chance that nucleation bubbles will emerge in some patches of space because of the ρ field tunneling from the false minimum to the true vacuum. This is a first-order phase transition, which is a source for gravitational waves which could be observed at Earth. T_0 on the other hand is the point at which the field can roll with ease to the true vacuum resulting in a second-order phase transition, which is of no importance to us, since this does not result into gravitational waves.

The next part is to try and find the bounce action resulting from the potential, which was introduced in the previous paragraphs. The bounce action is very important, since this lets us find the nucleation temperature. After calculating the bounce action it is possible to calculate α and β/H_*, two parameters which will be of particular importance when looking at the gravitational wave spectrum, see Eq.(5.74).

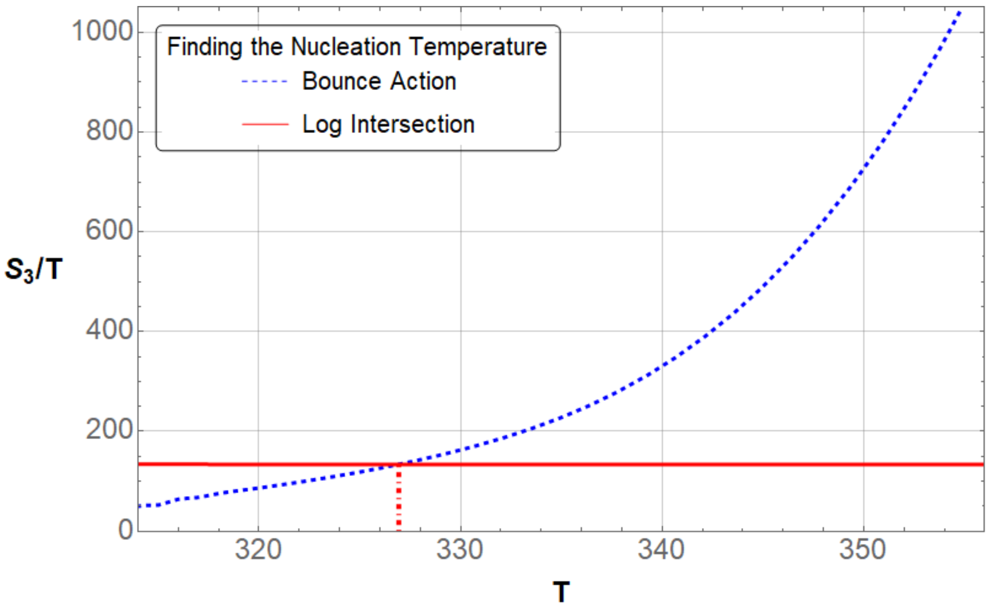

Figure 6.2: The bounce action shown here is calculated for parameters given in Table 6.2. As in the toy example, the search for the nucleation temperature leads one to look for the intersection between the bounce action and the horizontal red line. The nucleation temperature is represented by the vertical red dot-dashed line. The scale in this case is 10^3 GeV.

	g_D	λ	μ
Value	0.85	0.01	100

Table 6.2: To give an example of how the bounce action and the nucleation temperature in the minimal dark matter model are calculated, the parameters of this table are chosen. The coupling λ and μ are chosen such that v_ϕ = 1 TeV.

The bounce action is calculated for specific values of g_D, μ and λ, found in Table 6.2. Figure 6.2 shows this bounce action from which it is possible to compute the nucleation temperature T_{nuc}.

The plot shows the same concept as in the toy model. To find the nucleation temperature after numerically calculating the bounce action, an intersection must be found between the bounce action and Eq.(5.62), yielding T_{nuc}.

Scales and connection to the dark matter production mechanisms Before we start the computation of the GW spectra of interest to the minimal model of the thesis, the dependence of the nucleation condition on the scale is discussed. This is also the reason why there are no units shown in the temperature axis in Figure 6.2 for example. Up until the point of calculating the nucleation temperature it is possible to do the computation without ever mentioning the scale of the problem. The nucleation condition however, Eq.(5.68), does depend on the scale you are studying. The nucleation condition is

$$\frac{S_3(T_{nuc})}{T_{nuc}} \simeq 4\log\left(\frac{T_{nuc}}{H(T_{nuc})}\right) \sim 4\log\left(\frac{M_{Pl}}{T_*}\right), \tag{6.6}$$

where on the left hand side, the bounce action is dimensionless and therefore independent of the scale. It is when looking at the right hand side of the equation and at the ratio of the nucleation temperature with the Hubble rate and more specifically with the Planck Mass that the scale does come into play. Hence, the scale has to be specified to find the right nucleation temperature.

We want to find what are the relevant scales and what is the corresponding frequency range in the SBGW signal. The idea is to compute gravitational wave spectra that can be seen by upcoming detectors, like LISA. The goal is to examine multiple scales of the nucleation corresponding to different dark matter production mechanisms, thereby creating different types of spectra that could be seen in the different interferometer experiments.

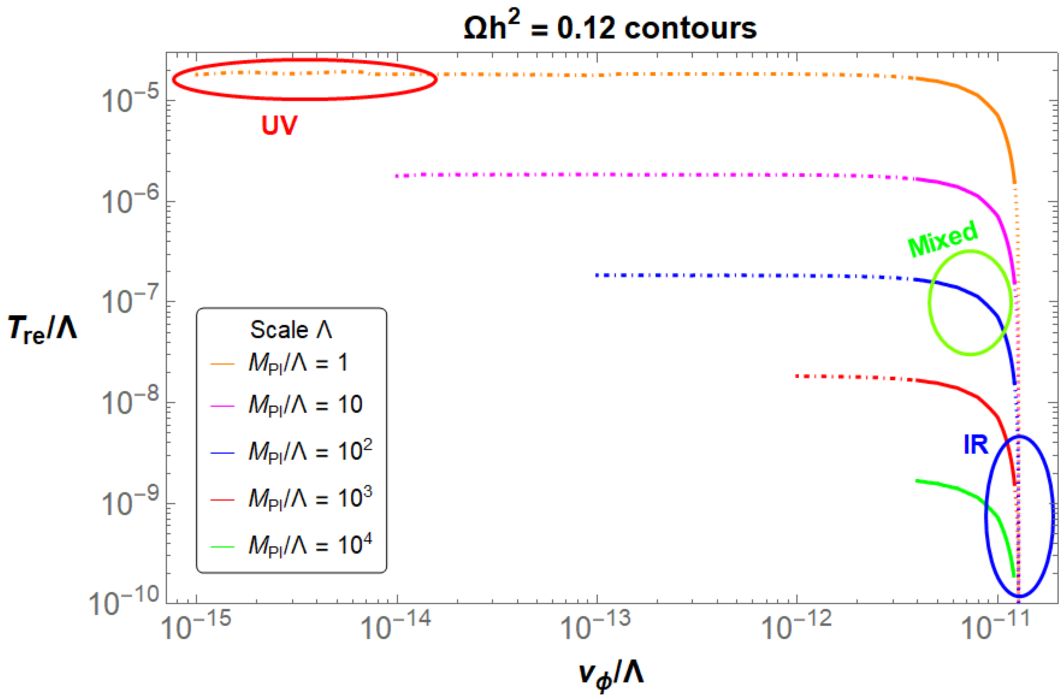

Figure 6.3: This plot shows the contourplot from Figure 4.4 but highlights the three scales that are chosen to represent the three possible production channels for dark matter. On the left side there is the chosen scale for UV dominated production represented by the red ellipse, on the right side below the scale of IR dominated production is represented by the blue ellipse and the third mixed production channels scale is represented by the green ellipse.

The question is then: what are the scales for which we calculate the spectra? Therefore we need to look back at the dark matter part of this thesis, specifically at Figure 4.4. Based on this figure, it is possible to get an idea of what are the relevant and important scales for the dark matter minimal model. For example, three scales corresponding to a fully

IR production dominated, a fully UV production dominated and a mixed contribution from both production channels are chosen to cover all the regimes of the dark matter production. The process of choosing the scales is represented in Figure 6.3. The scale is represented by v_ϕ, since this is where we roughly expect the phase transition to happen.

Looking at the plot, it can be seen that there are multiple possibilities for the scales. Since the gravitational wave spectrum does not depend on Λ, it is possible to pick scales of v_ϕ, represented on the horizontal axis as v_ϕ/Λ, from different contours of M_{Pl}/Λ. For the IR dominated production, all the contours come together at a value around $v_\phi/\Lambda \sim 10^{-11}$. This is the biggest value for this ratio, so to get the highest possible scale of v_ϕ we will take Λ at its highest, namely $\Lambda \sim M_{Pl}$. In that case $v_\phi \sim 10^7$ GeV. This is the scale corresponding to purely IR dominated production for dark matter.

Now for a purely UV dominated production, we would like to pick the smallest scale available. We study the plot and follow the UV dominated part of the contours to its end. There we find that for all the different ratio's of M_{Pl} and Λ the contours stop at a point where $v_\phi \sim 1$ TeV. So this is the scale taken to represent UV dominated production.

The last chosen scale will represent the mixed production of dark matter, coming both from the UV and IR channels. This region can be found in the part with full lines on the graph. Here the contours take a turn. But it is seen that the turns are all around the value of $v_\phi/\Lambda \sim 2 \times 10^{-11}$. If we then take the ratio of the Planck mass and Λ to be 10^2 we can find that $v_\phi \sim 2 \times 10^5$ GeV. Thereby we have found the three scales for which we would like to calculate the gravitational waves spectra. An overview of the three scales is given in Table 6.3.

As seen in Figure 6.3, the freedom to choose a scale corresponding to a certain dark matter production scenario is rather large. For example for the UV scale, we could also have picked a scale on the pink, blue or red dotdashed line, because these also represent a UV dominated dark matter production regime. However, we have picked these three scales here for a reason. We wanted to make sure that the two scales corresponding to the UV and the IR contribution represented the outer most possible scales in the dark matter minimal model with the mixed contribution as the perfect in-between.

dark matter Production	UV	IR	Mixed
Scale v_ϕ	1 TeV	10^4 TeV	200 TeV
g_D	1.197	1.171	1.179
T_{nuc}	120 TeV	146×10^4 TeV	139×200 TeV
α	0.2	0.2	0.2
β/H_*	248	408	318

Table 6.3: The table shows the three chosen scales for v_ϕ that correspond to the different cases in dark matter production in the minimal model of the thesis, one where the UV production is dominant, one where the IR production is dominant and one where the production is mixed. The table also shows the relevant parameters to calculate the benchmark for the GW spectrum for each of the three scales shown in Figure 6.8. The double line in the table is to divide the input parameters v_ϕ and g_D from the computed parameters.

Exploring the parameter space of the model Now the real work can start. For all three chosen scales, starting from the finite temperature effective potential, the bounce action will be computed for varying g_D. After this, α, β/H_* will be computed for all the values of g_D. A benchmark for one specific g_D per scale will then be chosen corresponding to the highest possible value of α that is the same for all three scales. From the chosen α and β/H_*, we calculate the gravitational wave spectrum for the three scales.

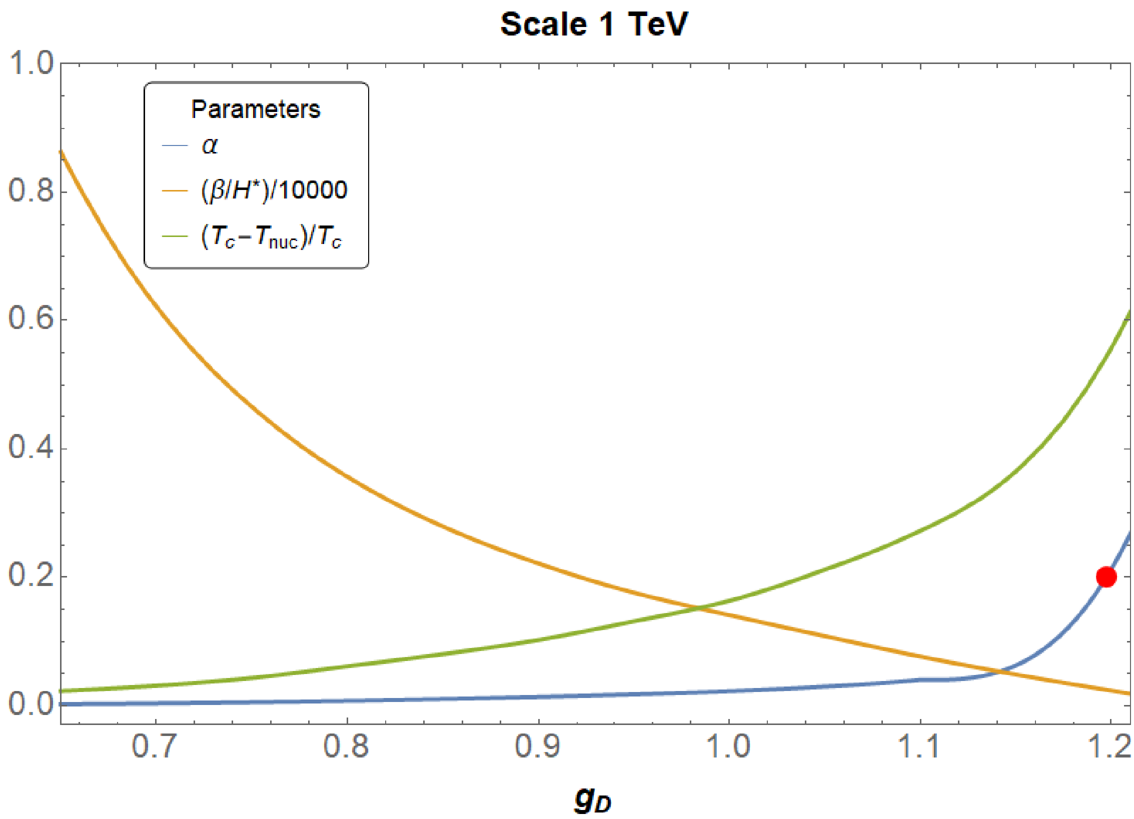

Figure 6.4: This figure gives the results of the bounce action computation for a scale of 1 TeV. It shows the interpolated functions for α, β/H_* and the relative difference between T_{nuc} and T_c as a function of g_D.

Throughout all calculations, λ, the coupling of the quartic self-interaction, is taken to be 0.01. The reason for this choice is that, by direct investigation, we found that a small value for λ favours the creation of a sizeable SBGW, but at the same time we do not want to tune this parameter to unnaturally small values. Then the first scale that is investigated is 1 TeV, corresponding to a UV dominated production for dark matter. The potential, the bounce action and all the parameters needed to obtain the spectra are calculated as a function of g_D. In this case we do not go to the very small values of g_D, since at these very small values of the dark gauge coupling there will be no first-order phase transitions, because there will be no barrier present through which the field can tunnel. The results of the 1 TeV computation are shown in Figure 6.4.

As seen in the plot, both α and the relative difference between the temperatures increase with higher values of g_D while β/H_* decreases for higher values of g_D. This can be explained by looking at the calculated bounce actions and the corresponding nucleation temperatures for different values of g_D, shown in Figure 6.5.

The two bounce actions for different values of g_D are clearly present in a different range of temperatures. It is noticed in Figure 6.5 that even though the intersection log stays the same, the nucleation temperature for the two bounce actions is different. This will have the greatest effect on β/H_*, defined in Eq.(5.71) as the derivative of the bounce action at the nucleation temperature multiplied by the nucleation temperature. It is clear from the plot that for smaller g_D, β/H_* is bigger, since the bounce action is steeper at the intersection point and the derivative is therefore larger as well. There is also a secondary effect that makes β/H_* bigger, since the nucleation temperature is higher for smaller g_D. This enlarges β/H_* even more compared to larger g_D.

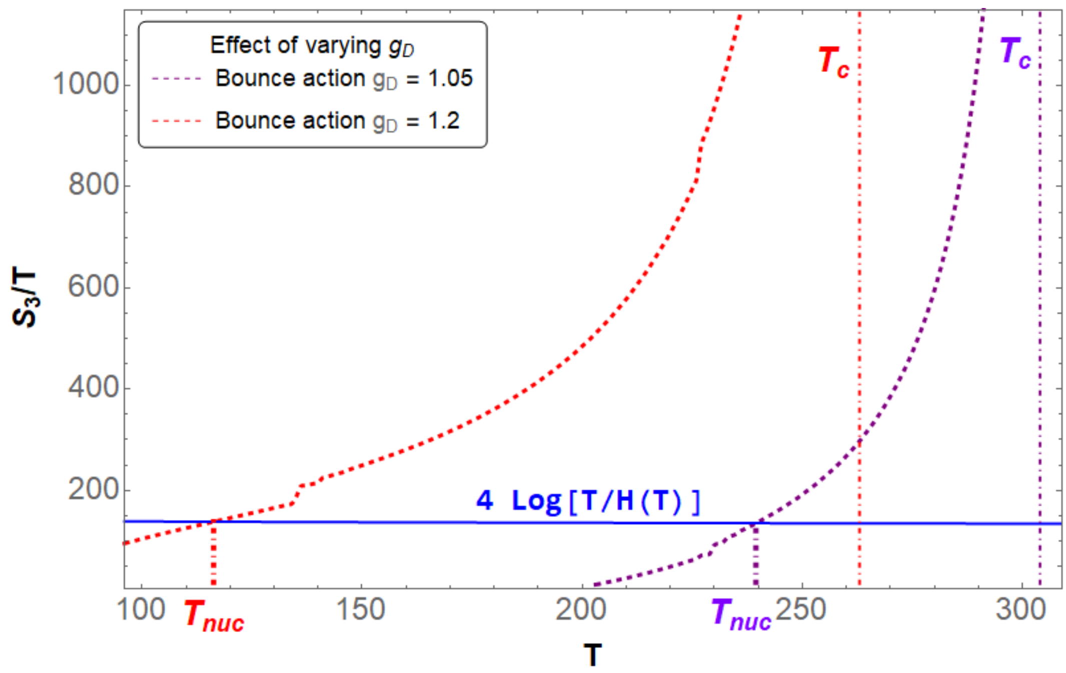

Figure 6.5: The figure shows two different bounce actions for two different values of g_D. The two log intersections overlap with each other since the two values of g_D, 0.8 for the smaller value and 1.2 for the larger value, are not orders of magnitude different from each other. This difference will not be seen when put in the log. The two T_c are also shown as a dotdashed line in their respective colours as are both T_{nuc}. The scale chosen to plot the nucleation condition is this case is 1 TeV.

We also see an effect on the ratio $(T_c - T_{nuc})/T_c$ in Figure 6.4. This ratio becomes bigger for larger g_D. This effect is also observed in Figure 6.5. The intersection point for the larger value of g_D is further away from T_c, where T_c is shown as the smaller dotdashed purple line. For the case with smaller g_D, T_c is shown as the smaller red dotdashed line. There the difference between T_{nuc}, represented as a thicker dot-dashed line in their respective colours, and T_c is visibly smaller. The ratio in the latter case is therefore smaller than in the former case, because the difference between T_c and T_{nuc} is smaller. This effect is seen in Figure 6.4, where the ratio becomes larger for increasing g_D.

The last remaining parameter we need to discuss is α. As seen in Eq.(5.65), it depends on T_{nuc} as $\alpha \sim 1/T_{nuc}^4$. This means that a smaller nucleation temperature means a bigger value of α. The nucleation temperature for the larger value of g_D is smaller and α is therefore bigger. Thus, the larger g_D, the larger α will be. This effect is also seen in Figure 6.4.

The computation of α, β/H_* and the ratio of T_c and T_{nuc} was also carried out for other scales, namely 200 TeV and 10^4 TeV. The results of these calculations can be found in Figure 6.6.

These results show the same behaviour as the plot for a scale of 1 TeV, which is to be expected since all computations for the three scales are done with the same bounce actions. Remember that the scale only comes into play when the nucleation temperature is calculated according to Eq.(5.68). This means that the same qualitative trends will be seen, even though the exact values of the important parameters might not be the same.

We observe that for higher scales the values of the parameters α and the ratio of the temperatures become higher, while β/H_* becomes smaller. This can be explained by looking at how the bounce action and the nucleation temperature is computed. The procedure for the different scales is given in Figure 6.7 using the parameters from Table

6.2.

As seen in the plot for larger scales, given in purple, the intersection with the bounce action will be lower than in the case with the lower scale, given in red. The reason why this intersection will have a larger value is understood when studying Eq.(6.6). Since the temperature and scale divide the Planck mass, which is a constant, in the log, the scale will make sure that the intersection has a smaller value, but not that much smaller due to the log in front. Hence the intersection will have a lower value, leading to the following effects.

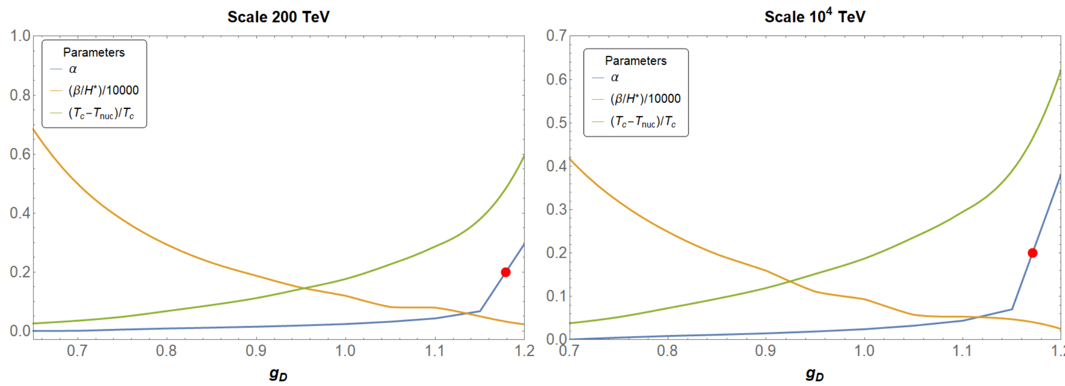

Figure 6.6: Both plots show the interpolated functions for α, β/H_* and the ratio $\frac{T_c - T_{nuc}}{T_c}$ as a function of g_D. On the left for a scale of 200 TeV and on the right for a scale of 10^4 TeV.

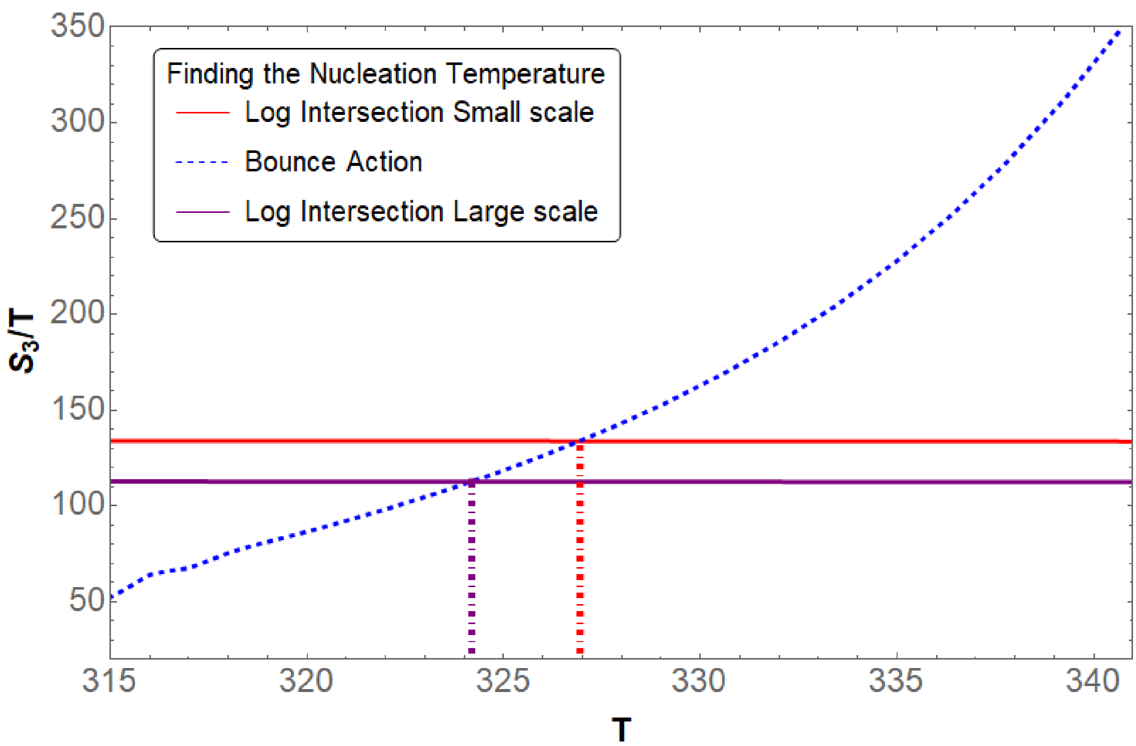

Figure 6.7: This bounce action and the intersection are shown here to investigate the difference in the scales that can be studied and how these scales change the intersection point and the nucleation temperature. The little bump in the left part of the bounce action is due to numerical errors.

The lower intersection results into a lower nucleation temperature for the higher scale compared to the lower scale as seen in Figure 6.7. Therefore this influences the ratio, $\frac{T_c - T_{nuc}}{T_c}$ which becomes smaller as a result, since T_c stays the same. This phenomenon of a lower nucleation temperature for larger scales has an effect on the important parameters that generate the GW spectrum. This is most clearly noticed when studying β/H_*. The intersection which defines the nucleation temperature has a lower intersection point with the bounce action. Therefore β/H_* will decrease twice by this effect, once because the derivative of the bounce action decreases and once because the nucleation temperature is smaller.

However, a different effect will be happening when looking at α, Eq.(5.65). As seen from its definition it has the following dependence on the nucleation temperature, $\alpha \sim 1/T_{nuc}^4$. Hence a smaller nucleation temperature will actually lead to a rise in α, the same effect we had when studying a varying gauge coupling g_D. We conclude that the different scales at which you calculate the nucleation temperature do have an effect on the relevant parameters and therefore on the computed GW spectra.

Gravitational Wave Signal The following step is to take the same value of α for the three different scales and plot the predicted GW spectra that could possibly be seen in upcoming detectors like LISA and Einstein Telescope. Taking the same α will result in the benchmark having a different value for both β/H_* and g_D. We pick $\alpha = 0.2$ for comparison between the different scales. These benchmarks appear as the red dots in Figure 6.4 and Figure 6.6 and are also shown in Table 6.3. This is the largest value of α that is present for all scales and therefore is the logical choice, since larger values of α account for a bigger amplitude in the GW signal and therefore more chance of being seen in detectors. We also deduce then that for larger values of g_D one gets a GW signal with a higher amplitude.

As a small sidenote, we can wonder why the computation for varying g_D does not extend beyond $g_D = 1.2$, since higher values for g_D will give rise to more potent GW signals. However, by direct inspection we find that for larger values of g_D, keeping λ fixed, the one-loop effects proportional to g_D become bigger than the tree-level λ effects and change qualitatively the shape of the potential at zero temperature. This is something which might signal a breaking of perturbativity. We want to avoid this scenario and therefore we decided to consider 1.2 as the maximally allowed value of g_D.

The spectra can be calculated using Eq.(5.74) applied to the minimal model

$$h^2\Omega_{\rm sw}(f) = 2.54 \times 10^{-6} \left(\frac{H_*}{\beta}\right) \left(\frac{\kappa_v \alpha}{1+\alpha}\right)^2 S_{\rm sw}(f), \tag{6.7}$$

where the peak frequency in the minimal model is given by

$$f_{\rm sw} = 1.94 \times 10^{-2} {\rm mHz} \left(\frac{\beta}{H_*}\right) \left(\frac{T_*}{100{\rm GeV}}\right), \tag{6.8}$$

where in both equations we have taken $v_w = 1$ and $g_* = 113.75$. The result can be seen in Figure 6.8.

As foreseen the signals have more or less the same amplitude, since the chosen α is the same for all scales. The power law is also the same, since the SBGW production mechanism for all scales are assumed to be sound waves in the plasma. However there is a difference when looking at the peak frequency of each scale. This feature is the one that could make it possible to distinguish between the different scenarios experimentally.

We want to examine the signals themselves first. The IR production corresponds to the biggest scale of v_ϕ and UV to the smallest since the IR contribution will dominate for bigger v_ϕ and the UV will dominate for smaller v_ϕ. The IR signal is shown in blue, the UV signal in red and the signal for a mixed contribution of dark matter production is shown in green. The signals are moving towards higher frequencies when the scale increases. This is explained by utilising Eq.(5.76). The peak frequency is dependent on the nucleation temperature. The nucleation temperature is influenced by the scale, which is different for the three cases. As a result the peak frequency is bigger for a bigger scale, which translates into a shift of the signal to the right in the plot towards higher frequencies. Thus, the peak frequency of the signal indicates the scale v_ϕ, which in turn correlates to the dark matter production mechanism through Figure 6.3. While β/H_* is also different in the three cases, see Table 6.3, this will only have a slight decreasing effect. This is why the amplitude of the spectrum in the three cases is going down slightly from the UV case to the IR case even though α is the same for the three cases.

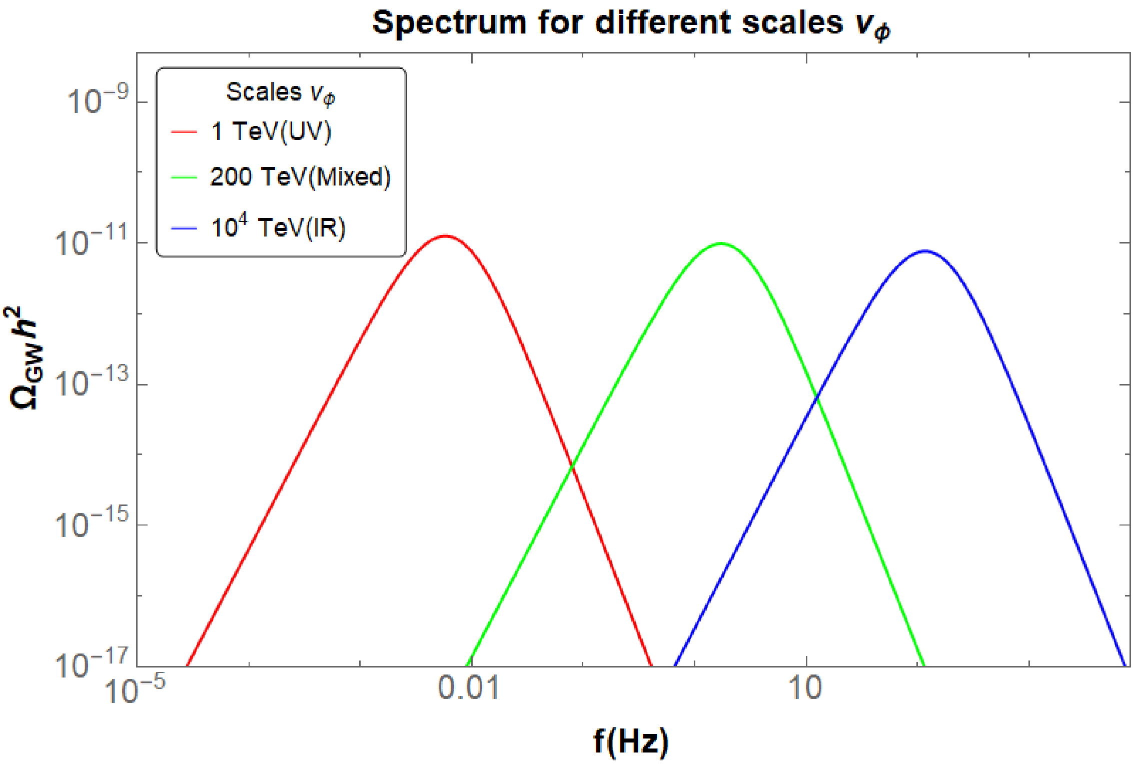

Figure 6.8: This shows the calculated GW spectra for different scales of v_ϕ corresponding to different dark matter production scenarios.

The three spectra together cover a frequency range from around 10^{-5} Hz until 100 Hz. Therefore, in general, a SBGW signal from the dark matter minimal model is expected to be in this frequency range. This is good, because this frequency range agrees with the frequency ranges where upcoming experiments for detecting gravitational waves coming from a cosmological stochastic background of gravitational waves like LISA, ET and BBO are sensitive.

We have chosen the benchmarks such that g_D does not have the same value for the three different production regimes, since these spectra would not have the same amplitude if we picked the same value of g_D for the three cases. The dependence on g_D comes into play when looking at the corrections to the potential coming from interactions of ρ with the Z' boson. So this has an effect on the behaviour of the potential and therefore also on the bounce action, on the calculated values of T_{nuc} and all other parameters computed from the bounce action. That leads to a possibly false interpretation that for some scales, the amplitude of the signal would be larger than other scales which is not necessarily the case. The amplitude depends on the exact parameters of the model and the amplitude for each scale changes when varying the parameters. Therefore it was chosen to compute α, β/H_* and the ratio between T_{nuc} and T_c, $\frac{T_c - T_{nuc}}{T_c}$, for different values of g_D

and to try and find the same value of α such that the amplitude of the spectra is more or less the same for different scales. We chose α, since if you look at Eq.(5.74), the biggest dependence of the spectrum is on the value of α. Before discussing the detectability of these GW signals coming from a first-order phase transition in the dark matter minimal model in section 6.3, we will now shift our focus to a semi-analytical approach to try and compute the effective potential using a high T expansion.

6.2 High Temperature Expansion

All the previous calculations were performed using the full form of the finite temperature effective potential, Eq.(5.34). To compute the thermal part of the potential, numerical computations were required. However, as already mentioned in section 5.4, there exists a high T expansion for the thermal bosonic function J_B, see Eq.(5.38). In this section it is investigated if this high T expansion is a good approximation and is capable of computing the potential, the bounce action and parameters like α and β/H_* within a reasonable range from the numerical calculations. In performing the high T expansion we will also receive additional information about the existence of the barrier which makes sure that a first-order phase transition can happen and which parameter is responsible for this barrier. The high T expansion will also work as a cross-check for the numerical results.

Another interesting effect of this high T expansion is that the finite temperature effective potential of the dark matter minimal model can be written in a form similar to the toy model in Eq.(5.41). The constants present in that Lagrangian can be mapped to properties of the minimal model, such as the masses of the relevant particles. In the dark matter minimal model of the thesis, the loop contribution of ρ will be subdominant compared to the contributions coming from the new gauge Z' boson for the regime of couplings we are interested in, where $\lambda \ll 1$ and g_D is of order 1. In this section, the self-interaction of ϕ in the one-loop and thermal corrections is neglected. This means that the one-loop potential in this case is

$$V_1 = \frac{n_{Z'}}{64\pi^2}\left\{m_{Z'}^4(\rho)\left(\log\frac{m_{Z'}^2(\rho)}{m_{Z'}^2(v_\phi)} - \frac{3}{2}\right) + 2m_{Z'}^2(v_\phi)m_{Z'}^2(\rho)\right\}, \tag{6.9}$$

where the masses are given by Eq.(6.2), such that $m_{Z'}^2(v_\phi) = g^2 v_\phi^2/2$ is the mass of Z' boson and $n_{Z'} = 3$ is the degrees of freedom for the Z' boson.

Starting from Eq.(5.38), only using the thermal bosonic function for Z' and neglecting the sum over l, the first step of trying to map the high T expansion onto the toy model Eq.(5.41) is rewriting the thermal part of the effective potential into

$$V_T = \frac{T}{120}\left(-4\pi^2T^3 + \frac{15\, m_{Z'}^2(v_\phi)T\rho^2}{v_\phi^2} - \frac{30\, m_{Z'}^{3/2}(v_\phi)\rho^3}{\pi v_\phi^3}\right) - \frac{3g^4\rho^4\log\left[\frac{m_{Z'}^2(v_\phi)\rho^2}{a_b T^2 v_\phi^2}\right]}{256\pi^2}, \tag{6.10}$$

where a_b = 16 $\pi^2 e^{3/2-2\gamma_E}$ and γ_E = 0.5772 is the Euler-Mascheroni constant.

The second step in testing the high T expansion is to map the correct parameters to the constants A, D, T_0 and λ from Eq.(5.41). By plugging Eq.(6.9) and Eq.(6.10) into Eq.(5.34) and writing it in the form of Eq.(5.41), the following relations are found

$$D = \frac{m_{Z'}^2}{4v_\phi^2}, \tag{6.11}$$

$$T_0 = \frac{1}{4}\sqrt{4\,\mu^2\left(\frac{14\,v_\phi^2}{m_{Z'}^2} - \frac{3\,m_{Z'}^2}{\pi^2 v_\phi^2\lambda}\right)}, \tag{6.12}$$

$$A = \frac{m_{Z'}^3}{4\pi v_\phi^3}\,, \tag{6.13}$$

$$\lambda(T) = \lambda - \frac{3}{16\pi^2 v_\phi^4}\left(m_{Z'}^4 \log\left[\frac{m_{Z'}^2}{A_b T^2}\right]\right)\,, \tag{6.14}$$

where $\log A_b = \log a_b - 3/2$.

The next step is plugging in these constants into the potential for a certain benchmark of the relevant parameters and examine if the potential coming from the high T expansion does approximate the actual potential well enough. This comparison is done in Figure 6.9 using the parameters from Table 6.4.

μ	g_D	λ
100	1.0	0.01

Table 6.4: These parameters are used to calculate and compare the numerical potential with the approximated potential in the high T expansion in Figure 6.9. They are also used in the comparison between the numerical bounce action with the bounce action coming from the high T expansion. That is shown in Figure 6.10.

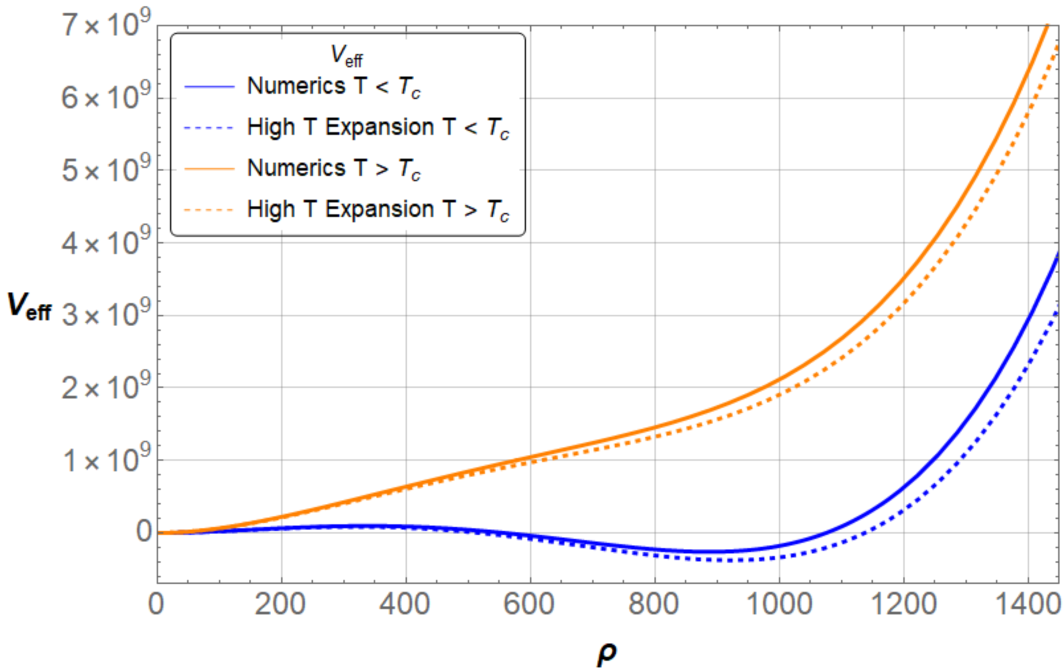

Figure 6.9: This shows both the actual potential coming from the numerical calculations as a full line and the potential in the high T expansion as a dashed line. The blue lines represent a lower temperature while the orange lines represent a higher temperature.

The figure shows both the potential calculated numerically, the full line, and the potential in the high T expansion, dashed line, for two different temperatures, $T < T_c$ in blue and $T > T_c$ in orange. Since it is the high T expansion, it is expected that for higher temperatures the approximation works better. This is confirmed by the potentials in the figure. The orange lines are on average closer together than the blue lines even for higher ρ. However, even for the smaller temperatures the high T expansion is very close to the numerical case, especially in the more important parts of the potential close to the barrier. That is already a good first indicator that the high T expansion works well even in regions where the temperature is lower.

The two approximated potentials are also in general a bit lower compared to the numerical potential for higher values of ρ. This is because not only the thermal bosonic function was approximated, the ρ contribution in the one-loop and thermal part of the potential were also neglected. Therefore the potential in the high T expansion will be a bit smaller compared to the numerical one. This means that in the high T expansion, T_c will be a little bit bigger than in the numerics case, since the point of degenerate vacua is reached faster when T is decreased. This also means that in the high T expansion the point where ρ becomes a local maximum is achieves faster as well, leading to a bigger T_0. Nevertheless, from our analysis, it can be concluded that in general the high T expansion approaches the actual potential well enough.

From the approximated potential, it is also possible to calculate the bounce action via a semi-analytical formula. The bounce action can be derived for the potential form of Eq.(5.41) and is given by [51]

$$\frac{S_3}{T} = \frac{13.72}{A^2}\left[D\left(1-\frac{T_0^2}{T^2}\right)\right]^{3/2} f\left[\frac{\lambda(T)D}{A^2}\left(1-\frac{T_0^2}{T^2}\right)\right], \tag{6.15}$$

where

$$f(x) = 1+\frac{x}{4}\left[1+\frac{2.4}{1-x}+\frac{0.26}{(1-x)^2}\right], \tag{6.16}$$

is a fitted function coming from numerical calculations [51, 63].

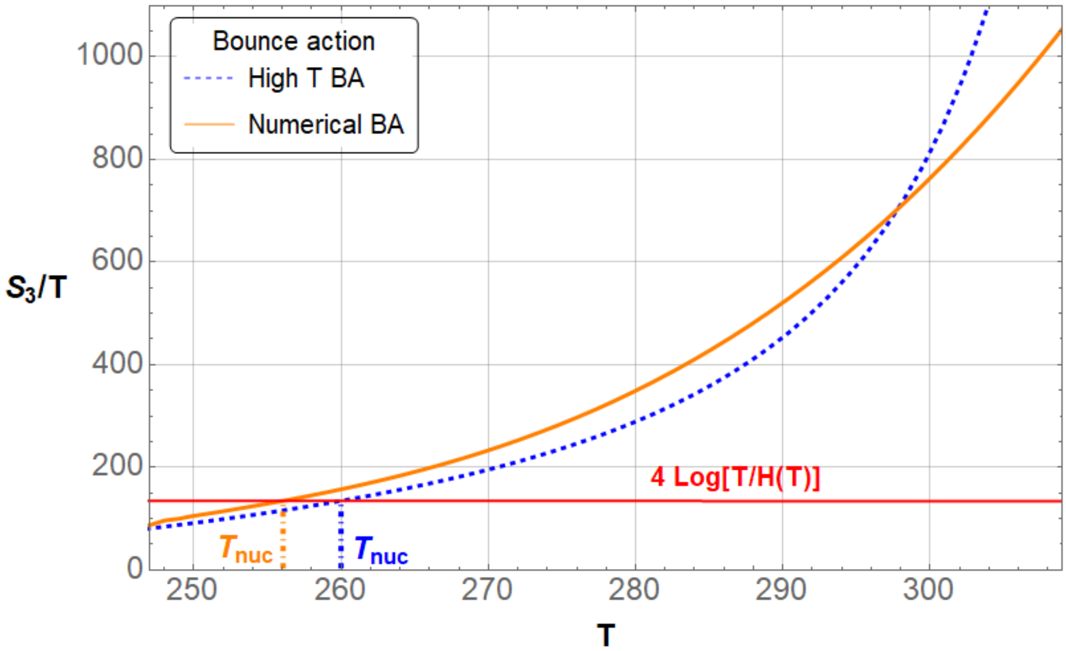

Figure 6.10: In the plot, two bounce actions are shown denoted as BA. The numerical one is shown as the orange full line, while the high T expansion bounce action computed using Eq.(6.15) is shown as the blue dashed line. Once again, the nucleation temperature can be computed using Eq.(6.6), this time represented as the full red line. The resulting nucleation temperatures are represented by the dot-dashed lines with the matching colours to their respective bounce actions. The scale is chosen here to be 1 TeV.

From this semi-analytical formula for the bounce action and using Eqs.(6.11)-(6.14) to fill in for the constants, one can compute the bounce action using the high T expansion. The nucleation temperature can be computed in the same way as before using Eq.(5.68), but now making use of the bounce action obtained with the high T expansion. It is once again interesting to compare the bounce action and the nucleation temperature to the full numerical result. The result can be seen in Figure 6.10 using the parameters from Table 6.4.

The semi-analytical bounce action agrees reasonably well with the numerical one, especially in the most relevant temperature region for the nucleation condition close to T_{nuc}. This is expected since the region that determines the bounce action is the region of the potential close to the barrier, which is well approximated by the high T expansion, as seen in Figure 6.9. At higher T, closer to T_c, the two bounce actions deviate more from each other, this is because Eq.(6.16) is no longer accurately fitting the bounce action at those points. This function $f(x)$ will blow up when $x \to 1$, this is exactly the point where $T \to T_c$. At those temperatures the bounce action will no longer be accurately represented by the high T expansion. Following the general trend of higher values for the computed temperatures, like T_c and T_0, here the nucleation temperature for the high T expansion is also higher than in the numerical computation. That will lead to a lower value of α.

As seen in the plot, both values for T_{nuc} are close to each other. This ensures that the semi-analytical approach can also lead to reasonably good values for parameters α and β/H_*.

We perform a last comparison between the parameters α, Eq.(5.65), and β/H_*, Eq.(5.70), looking at the numerical results and results coming from the semi-analytical approach. The result is shown in Figure 6.11 where the full lines represent the numerical results and the dashed lines represent the semi-analytical results from the high T expansion.

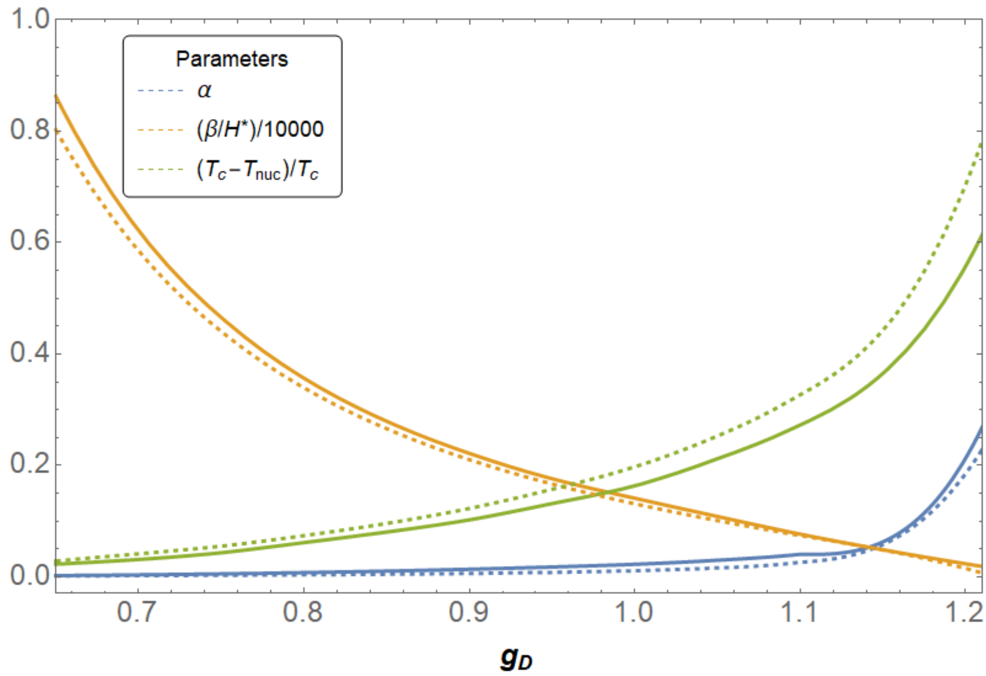

Figure 6.11: The figure shows both the numerical values, as full lines, and the semi-analytical ones, as dashed lines, for α, β/H_* and $(T_c - T_{nuc})/T_c$.

For small values of g_D these two almost agree completely for both α and the ratio of T_{nuc} and T_c. The agreement between the two is slightly worse for β/H_*, but still reasonable. It can be concluded that at these smaller g_D, corresponding to bigger T_{nuc}, the high T expansion works best. Looking at increasing g_D where T_{nuc} decreases, see the discussion around Figure 6.5 to understand why, it is expected that the high T expansion will be less and less accurate. Even then for the three parameters, the different lines stay quite close to each other.

Two of these parameters, β/H_* and T_{nuc}, are computed using the bounce action and the bounce actions of the numerical and semi-analytical result are in good agreement with each other in the region around T_{nuc} such that it was expected that these two parameters stay close to each other. The final parameter α however is calculated using the potential. It will still remain a good result for the high T expansion if one approximates ρ_* as

$$\rho_* = \left[-V[\eta(T),T] + T\frac{d}{dT}V[\eta(T),T]\right]_{T=T_{nuc}} \approx -V[\eta(T),T] \xrightarrow{T\to 0} \Delta V\,, \tag{6.17}$$

to calculate α, and where $\Delta V = V_1(v_{False}) + V_0(v_{False}) - V_1(v_\phi) - V_0(v_\phi)$. We can do the first approximation where we neglect the second piece with the derivative of the potential since the numerics show that it is subdominant. The second approximation is a bit more complex. This approximation is performed because we want the closest value of α compared to the full computation in the regime for larger g_D where the GW signal is the strongest. If we take a non-zero temperature, the semi-analytical value of α will significantly deviate from the fully computed value. However, if the temperature is zero, the semi-analytical computation does agree quite well with the full calculation.

An interesting viewpoint is also to review the results for a very small gauge coupling g_D. At some point there will no longer be a first-order phase transition. This is more easily understood using the formulas Eqs.(6.11)-(6.14) from the high T expansion. For a certain small value of g_D, there is no longer a barrier for finite temperatures in the potential. This is because the barrier in the potential is induced by the cubic term. See for example the discussion of Eq.(5.39) where there is no first-order phase transition due to the absence of the cubic term. The effect of the cubic term and therefore of the existence of the barrier becomes bigger or smaller depending on the value of A, given in Eq.(6.13). Since $m_{Z'} \sim g_D$, also $A \sim g_D^3$ such that if g_D gets smaller, A will get smaller as well and the barrier in the potential will disappear. Since there is no barrier there is no tunneling and a smooth crossover instead of a FOPT is expected.

The semi-analytic analysis is useful to extract some generic property of the phase transition and how they depend on the fundamental parameter of the model, as for example just discussed for the first vs. second order nature of the phase transition. The next step in the story is to try and combine the GW spectra from Figure 6.8 with the PLS curves from interferometer experiments discussed in section 5.3.

6.3 Detectability of the minimal model gravitational wave signals

The resulting Figure 6.12 shows the result of the hard work done in this thesis where we combine the PLS curves of LISA, BBO and the Einstein Telescope from Figure 5.6 with the GW spectra from Figure 6.8 that were calculated for the dark matter model. Before analysing this plot it has to be noted that these three signals are not the only signals possible for the model proposed in this thesis. We have chosen the three benchmarks from Table 6.3 as an example for the UV, Mixed and IR Freeze-In contribution to the dark matter production. One can imagine a line going from the top of the UV signal to the IR signal to represent all possible signals that could happen in the model depending on the chosen parameters. However it should be noted that the amplitude of the GW spectrum will depend strongly on the chosen values of the relevant parameters T_{re}, v_ϕ and $m_{\tilde{\ell}}$.

That being said, we can check what can already be concluded coming from these signals when comparing them to the PLS curves. Remember that a signal in a detector is seen with a certain threshold $\mathrm{SNR}_{\mathrm{thr}}$ when the gravitational wave signal comes above the PLS curve of this experiment.

Together with the three signals, we plot three PLS curves for three different experiments, namely LISA, BBO and the Einstein Telescope. If the signal reaches and crosses such a curve, then we could observe a signal in the detector with a given $\mathrm{SNR}_{\mathrm{thr}}$. The main goal of this thesis was to see if this was possible for the dark matter minimal model of the project and that we could link a GW signal to the dynamic history of the dark matter. Using the three chosen benchmarks it is possible to get a general idea if a signal will be visible for the three different production regimes and in which detector we need to look for such a signal.

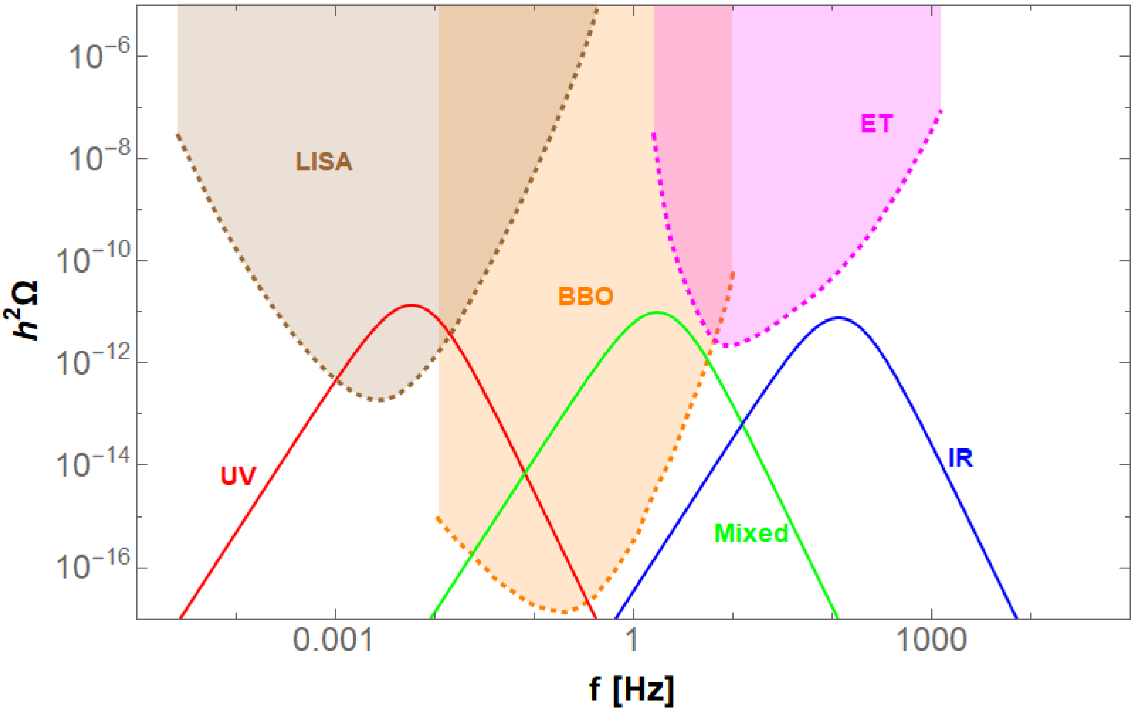

Figure 6.12: This plot shows the combined effort from the calculated GW spectra for the dark matter minimal model for different scales corresponding to different dark matter production regimes as well as the PLS curves from upcoming gravitational wave detectors, such as LISA in brown, Einstein telescope in magenta and BBO in orange.

Starting the discussion with the UV signal, it is observed that this signal crosses the PLS curve for both LISA and BBO. It can however not be concluded that the UV signal would be seen in LISA, since there are too many parameters fixed, for example changing $m_{\tilde{\ell}}$ can have an effect on the GW signal. It does however give an indication that if there was a signal noticed in LISA that this could point to a UV Freeze-In dominated dark matter production. We remind the reader that UV Freeze-In dark matter production happens when the dark matter is feebly coupled to the thermal bath via the higher-dimensional operator in Eq.(3.1) in contrast to IR Freeze-In production which is described by Eq.(3.5) where the dark matter is coupled to the thermal bath via the feeble coupling v_ϕ/Λ and where ϕ has taken a VEV. Other benchmarks for the relevant parameters can give another type of signal for the UV production which might have a smaller amplitude, for example if another smaller g_D is chosen where α is smaller. In that case, it could be possible that the signal is not seen at all in LISA.

The IR Freeze-In signal, in blue, does not cross any of the PLS curves for the specific parameters used in this benchmark. However, the frequency range in which the IR signal is present does correspond to the PLS curve of the Einstein Telescope. For this benchmark the signal will not be seen, but it is possible that for other different benchmarks, the signal goes slightly to the left and crosses the PLS of the Einstein Telescope. It can be noted that if a signal is seen in the Einstein Telescope it will probably come from an IR dominated dark matter production regime or possibly also the third and last option, the mixed dark matter production. The mixed production for this benchmark is completely engulfed by the PLS curve for BBO and is quite close to the Einstein Telescope PLS.

As a note on the end of this section, we need to mention that these PLS curves are made to observe and detect power law GW spectra. However, in our case, we are working with a broken power law from which the peak frequency crosses the PLS curve. Therefore, we need to be careful with stating that the signals are detectable by the experiments. However this process does give already an indication of the detectability of these signals.

7 Conclusion

This thesis started with a short summary on the status of dark matter. There was an overview of the experimental evidence for it, ranging from the rotation velocity curves of a galaxy to the observations of the anisotropies from the CMB. After that, we examined the possible existing options for what dark matter might be. For the thesis, we chose the path where we describe dark matter as a new fundamental particle.

Next, we discussed the two most studied dark matter production mechanisms, Freeze-Out and Freeze-In. The biggest difference between those two regimes is the coupling strength of the interaction and the presence of a dark matter initial abundance after reheating. The focus of this thesis is on the Freeze-In production regime.

To study dark matter, we introduced a dark matter minimal model consisting of four new particles: a scalar ϕ, a scalar mediator $\tilde{\ell}$, one fermion χ, the actual dark matter candidate, and a gauge boson Z'. This gauge boson was added together with one new gauge $U(1)_D$ symmetry with a gauge coupling g_D. One of the new particles ϕ takes a VEV v_ϕ, which spontaneously breaks the gauge symmetry.

In this thesis, two cases of the Freeze-In production regime were examined: the UV Freeze-In and the IR Freeze-In production. UV Freeze-In production happens most significantly at large temperatures, specifically close to the temperature of reheating T_{re}. The IR Freeze-In production happens significantly at lower temperatures close to $T \sim m_{\tilde{\ell}}$ until the mediator gets Boltzmann suppressed. We can ensure that both production regimes happen during the cosmological evolution of the Universe when we let ϕ take a VEV.

After a small introduction to the model and its production mechanisms in section 3, there was a more detailed discussion in section 4. Both relevant production mechanisms, UV and IR Freeze-In, were investigated and we found an analytical estimate for the yield in both cases.

After that, the yield and relic abundance for the dark matter minimal model were computed. We discussed the dependence of the yield on the parameters of the minimal model, both for a fixed UV contribution, meaning keeping T_{re} fixed, and for a fixed IR contribution where v_ϕ is kept fixed. Contours of the relic abundance were also calculated to check what parameter range is valid for this dark matter minimal model keeping in mind that $\Omega h^2 = 0.12$. The behaviour of these contours depending on the parameters of the minimal model was also discussed as well as for which values of the parameters that dark matter is dominantly produced by UV or IR Freeze-In.

The spontaneous symmetry breaking of the gauge symmetry when ϕ takes a VEV can also lead to the generation of gravitational waves, which is what we examined in the second part of the thesis. A short introduction was given on the concept of gravitational waves themselves. The relevant form for GW in the thesis was a stochastic background of gravitational waves coming from a first-order phase transition. After the introduction of the PLS curves of experiments which help us understand when a signal could be seen in a detector, we shifted our focus to a more detailed discussion of a stochastic background of gravitational waves coming from a first-order phase transition.

We studied the finite temperature effective potential in section 5.4. Starting from the tree-level potential, the effective potential was constructed where the one-loop and thermal corrections are added to this tree-level potential. We also introduced the high T expansion in this section which would is an approximation valid at high temperatures.

Phase transitions are divided in two categories, first-order and second-order. Both were illustrated with an example toy model in section 5.5. Second order phase transitions do not have a barrier and therefore the field can roll smoothly from the false vacuum to the true vacuum. In first-order phase transitions however, described by the finite temperature effective potential, there exists a barrier between the false and the true vacuum.

The field must tunnel to get to the true vacuum. This tunneling process is quantified by the bounce action and was both discussed for the zero temperature and finite temperature case. When the particle tunnels, bubbles are generated and gravitational waves can be created due to the friction of this bubble moving in the plasma around it. The temperature at which this process takes place can be found using the nucleation condition. At each point in the discussion about the first-order phase transition, we illustrated the concepts with a toy model. We ended the section with a discussion of how the GW signal coming from sound waves is generated from the properties of the effective potential and bounce action, specifically using α, β/H_* and T_{nuc} which capture the most important effect of the effective potential on the GW spectrum.

Then, we used the concepts of the first-order phase transition and implemented them in our minimal dark matter model. First, the finite temperature effective potential was computed for the minimal model. Then, to compute the GW spectra for the minimal model, we choose three benchmarks corresponding to three different scenarios of dark matter production. The benchmarks all correspond to a different scale for v_ϕ. The chosen scale has an influence on the nucleation condition and therefore on the nucleation temperature. This has an effect on the peak frequency of the GW signal that we might detect in the experiments.

We also explored what happens with the bounce action if we look at a varying gauge coupling g_D and what effect this has on the values of α, β/H_* and T_{nuc}. We saw that for large gauge couplings, corresponding to a larger barrier, α is larger, β/H_* is smaller and therefore the GW signal will have a larger amplitude. We also explored the nucleation condition for different scales and found that for larger scales, the nucleation conditions intersection with the bounce action is at a lower point in the bounce action, thereby leading to a lower nucleation temperature.

There was a small discussion about the high T expansion of the effective potential. The thermal part of the potential is approximated in that expansion and the scalar contribution is neglected. It was examined if this semi-analytical approximation agrees reasonably well with the full computation for the effective potential as well as for the bounce action. Seeing that this approach works quite well, we went a step further and compared parameters such as α and β/H_* with these parameters for the full case. Even then, the semi-analytical approach, with some extra approximations, seems to be quite reasonable. This high T expansion also helped us understand the reasons as to why a barrier exists in the effective potential for a first-order phase transition.

In the last section of the thesis, we investigated if the GW signals coming from the dark matter minimal model could be seen in upcoming interferometer experiments. It was found that indeed such signals are possible and can exist in the frequency range corresponding to the sensitivity range of experiments such as LISA, BBO and the Einstein Telescope. If such a signal is then observed in the detector, it might be possible to link this signal to different scales and thus for different dark matter production mechanisms when we make some assumptions about the parameters in the minimal model.

We end the conclusion by investigating future research and by examining complimentary probes to the gravitational wave signatures. In our approach in the thesis, we mainly focused on the relation between the peak frequency of the GW signal, i.e. the scale of the phase transition, and the dark matter production mechanism. It would be interesting to further explore the properties of dark matter and try to connect them to a resulting SBGW signal. In particular, we can investigate if these GW signals can provide extra information about the fundamental parameters of a dark matter model.

There are complimentary methods to try and discover dark matter and the new particles in our dark matter minimal model. For dark matter, we can look at direct and indirect detection where dark matter is tried to be detected by it scattering with SM particles or its self-annihilations into SM particles. However since we are interested in Freeze-In production for dark matter, the coupling of dark matter with the thermal bath is too feeble and we do not expect a significant signal in these types of dark matter experiments. Instead, we should be able to probe the other particles present in the dark matter minimal model, specifically ρ and $\tilde{\ell}$ at colliders if their mass is within the TeV scale.

It is possible that there are mixing terms between ρ, the dynamical fluctuation of ϕ, and H, the Higgs field. In this case, we could probe ρ at the LHC indirectly via modification of the expected Standard Model Higgs couplings or directly via pp production and the resulting decay products of ρ. The phenomenology in this case is analogous to the mixing of Higgs with a singlet [64].

Another particle that could be observed at colliders is the mediator $\tilde{\ell}$. Because of its hypercharge, it could be produced in electroweak processes at the LHC. Due to the small coupling, it has a long decay time, making it stable in colliders. Since it is a charged particle, we might be able to observe this particle as a stable heavy charged particle which will manifest itself at the LHC as a charged track [65, 66, 67].

In conclusion, as the original contribution of this thesis, we introduced a Freeze-In dark matter minimal model where both UV and IR Freeze-In production occurs. We have studied the dark matter yield and relic abundance coming from this minimal model and how it behaves in the parameter space of the model. In addition, we studied the first-order phase transition occurring in this model and the resulting SBGW signal. As a final result, we related the peak frequency of the SBGW to the corresponding dark matter production mechanism in the early Universe. Further investigation is necessary to further explore possible connections between dark matter models and GW signatures.

Acknowledgements What a year it has been. A year stuck inside my house, at my desk, behind a computer. Admittedly, not the way I had expected my last year of my master in physics to play out. I had expected to be stuck behind a desk behind a computer but at the VUB. The fact that you are able to read this thesis, which I am quite proud of and for which a lot of hours have been spend cursing, asking myself why I chose physics to begin with, but also being happy when it all works out in the end, is due to all the fantastic people I will mention here (I am so sorry if I forget anyone, but the deadline is really close right now). Without them, this would never have been possible and I am them very thankful for all their support.

First of all, I want to thank my promotor Prof. Dr. Alberto Mariotti for all his support and motivational words throughout the year. You were always there, even in the later hours, to answer my questions, to motivate me, to read my text, and to try and solve the problem I encountered together. I am also very grateful for the chance you gave me for the next 4 years to continue doing physics. Every week we met to discuss my proceedings and possible problems. Also present on those meetings were my two supervisors, Sam Junius and Kevin Turbang. Two people who also deserve a lot of the credit for the end result. They have supported me through the year and were also always present to have a quick chat when I had questions or when I was stuck on coding or physics. They read every part of this thesis multiple times and gave their comments for which I am very grateful. I must say that I am very happy to have worked this year with these three very supportive people who always challenged me, deepened my understanding of the physics presented in the thesis and improved my writing and without them, the result would not be even a quarter as good as it is now I think. I can say that they made this year more fun and rewarding that I imagined it even though we had almost no physical contact. *Grazie Mille a tutti!*

I also thank my parents, mostly for funding all this. No I am kidding, I mostly thank them for raising me to what I have become (for the good or for the worse), for being always supportive of whatever I do and for being there when needed. I thank them for making a warm home in which I feel at home.

I would like to thank my ex-girlfriend, who has supported me through the years and still does now. Thank you for being there and for making all the éclairs. They are great.

Last, but not least I will thank my fellow class mates, my colleagues, my friends. My not-physics related friends won't read this, but I thank them anyway for all the years together, the laughs and the amazing experiences which helped me to come to what I do and am today.

However, the colleagues of the master in physics, they might (I force them otherwise) read this. Floriano, thank you for being an overall great dude, my fellow fast cars on circuits (not in parks!) lover and a great friend who is always there for a chat or a quick meme. We all know that your drawing was better and remember, next year is our year. Yarno, thank you for all the late night chats and quizzes we did this year. For all the memes, for the support and for all the dreams. Thank you for being a bro, bro. Mitja, I think I speak for all master students when I say that without your ever supporting words and physics insights, we would not have made it this far. I know that you have got everyones back and that you are always there when needed. Thanks also for being a great organizer and really the king of the discord. Aäron, I thank you for laughing, for giving me greater insight in physics and mathematical equations. For being our coach, for being the happy vibe we need in our life and for having the best cut of us all. Nordin, thank you for being the Reinhardt to my Zarya, thank your mom for making food and your brother for his car. Your drawing skills on walls making Keith Haring look like a amateur never stop to amaze me and blessed be The Reference Man. Emilie, I thank for going on the campus cup journey with me, I can safely say that this was one of the things this year that kept my morale high and I enjoyed it a lot to do with you! Also I thank you for being a great taxi driver and for the musical interludes we had on the trips to Leuven which I was very sad about, have been cut short due to the small thing called the pandemic.

As a last thank you note, I want to thank all the people in the physics students VUB discord. Together, we had a lot of fun night this year, watching movies, playing video games and so much more. I am quite happy to see us all come together and enjoy our company. I am very happy to get to know the people in the lower years before I bow out and end this chapter of my life which I thoroughly enjoyed.

A Appendix

A.1 Boltzmann equation

The Boltzmann equation states that the rate of change in the number density n of a particle is given by subtracting the rate of annihilation of a particle from the production rate of a particle. A Boltzmann equation can schematically be represented as [68]

$$a^{-3}\frac{d\left(na^3\right)}{dt} = \mathcal{C}[n]\,, \tag{A.1}$$

where $\mathcal{C}[n]$ represents all possible interaction terms that have an effect on the number density of a particle. If there were no interactions, the Boltzmann equation shows that the number density times the scale factor cubed is a conserved quantity. This is an effect of the expanding Universe.

To further write out the Boltzmann equation for a particle, one need to pick the interactions through which it interacts. To give an example which is relevant to the thesis, we will write out a Boltzmann equation where it is assumed that the abundance of the particle is only affected by one process of annihilation consisting of four particles, 1 + 2 → 3 + 4, where particle 1 would be the particle of interest. In such a process particle 1 and particle 2 can annihilate producing particles 3 and 4. In the other direction, particles 3 and 4 can annihilate producing particles 1 and 2. The Boltzmann equation for such a process is

$$\begin{aligned} a^{-3}\frac{d\left(n_1a^3\right)}{dt} = & \int\frac{d^3p_1}{(2\pi)^3 2E_1}\int\frac{d^3p_2}{(2\pi)^3 2E_2}\int\frac{d^3p_3}{(2\pi)^3 2E_3}\int\frac{d^3p_4}{(2\pi)^3 2E_4} \\ & \times (2\pi)^4\delta^3\left(p_1+p_2-p_3-p_4\right)\delta\left(E_1+E_2-E_3-E_4\right)|\mathcal{M}|^2 \\ & \times \left\{f_3f_4\left[1\pm f_1\right]\left[1\pm f_2\right] - f_1f_2\left[1\pm f_3\right]\left[1\pm f_4\right]\right\}, \end{aligned} \tag{A.2}$$

where f_i is the distribution function for the corresponding particle i, with $i \in$ {1,2,3,4} and $|\mathcal{M}|^2$ is the Feynman amplitude for the annihilation process. It has been assumed that the amplitude of this interaction is reversible, identical in both directions of the interactions. The $1 \pm f_i$ terms, where $+$ sign stands for bosons and $-$ stands for fermions, represent the effects of Bose enhancement and Pauli blocking. Putting aside these terms for a second, the Boltzmann equation says that the production rate of particle 1 is proportional to the distribution functions of particles 3 and 4, f_3 and f_4. The annihilation rate depends on the distribution functions of particles 1 and 2, f_1 and f_2. The Dirac delta distributions ensure that energy and momentum conservation is satisfied. In this case, $E = \sqrt{p^2+m^2}$. To find the total number of interactions, one needs to integrate over all momenta. This is the first line of the equation.

To make the equation even simpler, it can be assumed that the scattering processes enforce kinetic equilibrium which means that the scattering takes place swiftly enough such that the distribution functions will follow the Bose-Einstein or Fermi-Dirac distributions

$$f = \frac{1}{e^{(E-\mu)/T}\pm 1}, \tag{A.3}$$

where $+$ is for the Bose-Einstein distribution for bosons and $-$ is the Fermi-Dirac distribution for fermions. To simplify the equation even further, we can look at interactions that take place at temperatures $T < E-\mu$. In that case both distribution functions become

$$f \backsimeq e^{\mu/T}\, e^{-E/T}, \tag{A.4}$$

Maxwell-Boltzmann distributed. The Pauli blocking and Bose enhancements can then also be neglected in the Boltzmann equation. This means that the last line from the Boltzmann equation becomes

$$\begin{aligned} & f_3 f_4 \left[1 \pm f_1\right]\left[1 \pm f_2\right] - f_1 f_2 \left[1 \pm f_3\right]\left[1 \pm f_4\right] \\ \rightarrow \quad & e^{-(E_1+E_2)/T}\left\{e^{(\mu_3+\mu_4)/T} - e^{(\mu_1+\mu_2)/T}\right\}, \end{aligned} \tag{A.5}$$

where energy conservation, $E_1 + E_2 = E_3 + E_4$ was used. Since we work with the number densities on the left hand side, it would be nice to have these number densities on the right hand side as well. The number density n is related to μ via

$$n_i = g_i\, e^{\mu_i/T} \int \frac{d^3p}{(2\pi^3)} e^{-E_i/T}, \tag{A.6}$$

where g_i is the degeneracy of the particle. The equilibrium density can also be defined

$$n_i^{EQ} \equiv g_i \int \frac{d^3p}{(2\pi)^3} e^{-E_i/T} = \begin{cases} g_i \left(\frac{m_i T}{2\pi}\right)^{3/2} e^{-m_i/T} & m_i \gg T \\ g_i \frac{T^3}{\pi^2} & m_i \ll T. \end{cases} \tag{A.7}$$

Using these definitions, $e^{\mu/T}$ can be written as n_i/n_i^{EQ}. Eq.(A.5) becomes

$$e^{-(E_1+E_2)/T}\left\{\frac{n_3 n_4}{n_3^{EQ} n_4^{EQ}} - \frac{n_1 n_2}{n_1^{EQ} n_2^{EQ}}\right\}. \tag{A.8}$$

As a last step, one can define the thermally averaged cross section

$$\begin{aligned} \langle \sigma v \rangle \equiv & \frac{1}{n_1^{EQ} n_2^{EQ}} \int \frac{d^3p_1}{(2\pi)^3 2E_1} \int \frac{d^3p_2}{(2\pi)^3 2E_2} \int \frac{d^3p_3}{(2\pi)^3 2E_3} \int \frac{d^3p_4}{(2\pi)^3 2E_4} e^{-(E_1+E_2)/T} \\ & \times (2\pi)^4 \delta^3\left(p_1 + p_2 - p_3 - p_4\right) \delta\left(E_1 + E_2 - E_3 - E_4\right) |\mathcal{M}|^2, \end{aligned} \tag{A.9}$$

such that the Boltzmann equation for a two-by-two particle scattering is rewritten in its simplest form as

$$a^{-3}\frac{d\left(n_1 a^3\right)}{dt} = n_1^{EQ} n_2^{EQ} \langle \sigma v \rangle \left\{\frac{n_3 n_1}{n_3^{EQ} n_1^{EQ}} - \frac{n_1 n_2}{n_1^{EQ} n_2^{EQ}}\right\}. \tag{A.10}$$

Another case for the Boltzmann equation may be a decay interaction

$$1 \rightarrow 2 + 3. \tag{A.11}$$

Then it can be written as

$$\begin{aligned} a^{-3}\frac{d(n_1 a^3)}{dt} = & \int \frac{d^3p_1}{(2\pi)^3 2E_1} \frac{d^3p_2}{(2\pi)^3 2E_2} \frac{d^3p_3}{(2\pi)^3 2E_3} \delta^4\left(p_2 + p_3 - p_1\right) \\ & \times \left[|M|^2_{1\rightarrow 2+3} f_1 \left(1 \pm f_2\right)\left(1 \pm f_3\right) - |M|^2_{2+3\rightarrow 1} f_2 f_3 \left(1 \pm f_1\right)\right]. \end{aligned} \tag{A.12}$$

Using the same techniques are for the scattering process, this Boltzmann equation can be simplified. The big difference with the scattering is that the thermally averaged cross section will here be substituted for a decay rate.

A.2 Feynman amplitudes and Boltzmann equations

In this section of the appendix, a detailed calculation is given for the relevant Feynman amplitudes in the dark matter minimal model using the operator Eq.(3.4) and Eq.(3.5). We will also rewrite the Boltzmann equation for the UV Freeze-In with detailed steps.

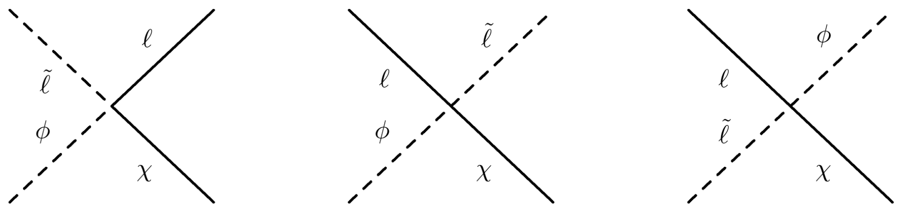

Figure A.1: These are the three relevant scattering processes for the UV Freeze-In production of dark matter.

A.2.1 UV Freeze-In

Feynman Diagrams Starting with the following Feynman diagrams in Figure A.1, we follow the Feynman rules to write down the Feynman amplitude. Focusing on the left Feynman diagram first we write the vertex and the spinors for the fermions

$$\frac{1}{\Lambda}\overline{u}_r(p_3)P_R\, v_s(p_4), \tag{A.13}$$

where we have taken p_3 for the momentum of the lepton and p_4 for the momentum of the dark matter particle and the projection operator $P_R = (1+\gamma_5)/2$ factor comes from the interaction only happening with right-handed leptons. The spin states are denoted by r, s = 1,2. It follows that

$$|\mathcal{M}|^2 = \sum_{r,s} \frac{1}{\Lambda^2}\,\mathrm{Tr}[\overline{u}_r(p_3)P_R\, v_s(p_4)\, \overline{v}_s(p_4)P_L\, u_r(p_3)], \tag{A.14}$$

where Tr[] represents taking the trace of a matrix, $P_L = (1-\gamma_5)/2$ and we have summed over the outgoing spin stares in r and s. Using

$$\sum_i u_i(p_j)\overline{u}_i(p_j) = \not{p}_j + m_i \quad \text{and} \quad \sum_i v_i(p_j)\overline{v}_i(p_j) = \not{p}_j - m_i, \tag{A.15}$$

where $\not{p} = \gamma^\mu p_\mu$, and the cyclic properties of the trace, we can write

$$\frac{1}{\Lambda^2}\mathrm{Tr}\left[P_R \sum_s v_s(p_4)\overline{v}_s(p_4)P_L \sum_r u_r(p_3)\overline{u}_r(p_3)\right] = \frac{1}{\Lambda^2}\mathrm{Tr}[P_R(\not{p}_4 - m_\chi)\, P_L\, \not{p}_3], \tag{A.16}$$

where the mass of the lepton was assumed to be negligible. The terms with m_χ disappear because the trace of an odd number of gamma matrices is zero and Tr$[\gamma_5\gamma^\mu]$ = 0. We can pull P_L through the slashed notation. Due to the γ^μ present in the slash and the anti-commutation relation between γ_5 and γ^μ, P_L changes into P_R. At the left side we then have P_R^2 = P_R. Another property of gamma matrices in traces is that

$$\mathrm{Tr}[\gamma_5\gamma^\mu\gamma^\nu] = 0, \tag{A.17}$$

such that only the term with two gamma matrices stays. Using the property of the gamma matrices

$$\mathrm{Tr}[\gamma_\mu\gamma_\nu] = 4\eta_{\mu\nu}, \tag{A.18}$$

the amplitude can be rewritten as

$$|\mathcal{M}|^2 = \frac{1}{\Lambda^2}2p_4\cdot p_3. \tag{A.19}$$

Using the Mandelstam variable $s = (p_3 + p_4)^2 \backsimeq 2p_4 \cdot p_3$, if the masses of the particles are assumed to be negligible, remember that $p_i^2 = m_i^2$, the amplitude for the scattering process is found

$$|\mathcal{M}|^2 = \frac{s}{\Lambda^2}. \tag{A.20}$$

The other two diagrams will have a different amplitude. Theirs is given by

$$|\mathcal{M}|^2 = \frac{s + t - m_\phi^2}{\Lambda^2}. \tag{A.21}$$

Rewriting the Boltzmann equation Since the Feynman amplitudes are now computed, the Boltzmann equations can be simplified. We start from the total UV Freeze-In Boltzmann equation in Eq.(4.1). Now, we will focus on the left diagram from Figure A.1, then it is possible to rewrite this into Eq.(4.3) using steps which can be found in [26]. Starting from Eq.(4.3), we can introduce some assumptions and simplifications into the equation. Firstly the mass of ϕ is assumed to be significantly larger than all other masses. This means that Eq.(4.4) can be rewritten. There are two cases, one for $P_{\phi,\tilde{\ell}}$ and $P_{\ell,\chi}$

$$P_{\phi,\tilde{\ell}} = \frac{[s - (m_\phi + m_{\tilde{\ell}})^2]^{\frac{1}{2}} [s - (m_\phi - m_{\tilde{\ell}})^2]^{\frac{1}{2}}}{2\sqrt{s}} = \frac{s - m_\phi^2}{2\sqrt{s}}, \tag{A.22}$$

$$P_{\ell,\chi} = \frac{[s - (m_\chi + m_\ell)^2]^{\frac{1}{2}} [s - (m_\chi - m_\ell)^2]^{\frac{1}{2}}}{2\sqrt{s}} = \frac{s}{2\sqrt{s}}. \tag{A.23}$$

It follows that $P_{\phi,\tilde{\ell}} P_{\ell,\chi} = \frac{[s - m_\phi^2]}{4}$. The Boltzmann equation is then

$$\dot{n}_\chi + 3Hn_\chi = \frac{2T}{512\pi^6} \int_{m_\phi^2}^{\infty} ds\, d\Omega\, \frac{[s - m_\phi^2]}{4} |\mathcal{M}|^2 K_1 \left(\frac{\sqrt{s}}{T}\right) / \sqrt{s}. \tag{A.24}$$

We can use the computed Feynman amplitude, Eq.(A.20), and perform the integral over $d\Omega$, which gives a factor 4π, to find

$$\dot{n}_\chi + 3Hn_\chi = \frac{2T}{512\pi^5\Lambda^2} \int_{m_\phi^2}^{\infty} ds\, [s - m_\phi^2] \sqrt{s}\, K_1 \left(\frac{\sqrt{s}}{T}\right). \tag{A.25}$$

The left hand side of the equation can be rewritten using the definition of the yield $Y = n/S$, with $S = (2\pi^2 g_S T^3)/45$, the entropy. First, the l.h.s can be written as

$$\dot{n}_\chi + 3Hn_\chi = \frac{1}{a^3} \frac{d(n_\chi a^3)}{dt} = T^3 \frac{d(n_\chi / T^3)}{dt}. \tag{A.26}$$

Then combine this with r.h.s, the definition of the yield and the integral defined in Eq.(4.6) to write

$$\frac{dY}{dt} = \frac{45}{512\, g_S\, \pi^7 \Lambda^2 T^2} I(T). \tag{A.27}$$

Switching the time variable to temperature T, using $dT/dt \sim -H\,T$, with $H = \frac{1.66\sqrt{g^\rho}T^2}{M_{Pl}}$ such that

$$\frac{dY}{dT} = -\frac{45\, M_{Pl}}{512\, g_S \pi^7\, (1.66) \sqrt{g_\rho} \Lambda^2} \frac{I(T)}{T^5}. \tag{A.28}$$

However, this is not the only contribution for the UV Freeze-In process. We also have additional contribution from the other two processes shown in Figure A.1. Their Feynman amplitude is given in Eq.(A.21). The first difference we see is that this amplitude also depends on the Mandelstam variable t. This will have an impact on the calculation, since

t is dependent on θ, which sits in the integral in $d\Omega = d\phi dcos(\theta)$. So, the integral over the angle will no longer give a factor 4π.

Let's write down the right hand side of the (simplified) Boltzmann equation for the middle diagram, where $\ell\phi \to \tilde{\ell}\chi$, in Figure A.1

$$\frac{2T}{512\pi^6}\int_{m_\phi^2}^{\infty} ds\, d\Omega\, P_{\phi,\ell}\, P_{\tilde{\ell},\chi}\, |\mathcal{M}|^2\, K_1\left(\frac{\sqrt{s}}{T}\right)/\sqrt{s}. \tag{A.29}$$

Before writing this out, we want to examine how t depends on θ. Using the calculations from [69, 70] we can write

$$\begin{aligned} t &= (p_1 - p_3)^2 = p_1^2 + p_3^2 - 2p_1 \cdot p_3 \\ &= -2E_1E_3 + |p_1||p_3|cos(\theta)\,, \end{aligned} \tag{A.30}$$

where p_1 is the momentum from the lepton and p_3 the momentum of the mediator. We have also chosen to neglect their masses and since $p_i^2 = m_i^2$, the first two terms were put away. From [70], we know that $E_1 = \frac{s-m_\phi^2}{2\sqrt{s}}$ and $E_3 = \frac{s}{2\sqrt{s}}$. We will need these formula's to perform the integral over s. However, we need to start with the integral over $dcos(\theta)$. As we can see, there is one term dependent on $cos(\theta)$ and this is an odd function in $cos(\theta)$, however since the boundaries of the integral are -1 and 1, odd functions integrated over this integral will result in zero. Therefore only the terms without $cos(\theta)$ stay. They get an extra factor 2 from the integration. Also, we have to take into account that the integral over $d\phi$ gives another factor of 2π.

Putting this all together, we find that

$$t = -\frac{s - m_\phi^2}{2} + |p_1||p_3|cos(\theta), \tag{A.31}$$

and the integral over $cos(\theta)$ gives an extra factor 2 such that Eq.(A.29) becomes

$$\frac{4T}{512\pi^5}\int_{m_\phi^2}^{\infty} ds\, P_{\phi,\ell}\, P_{\tilde{\ell},\chi}\, (s - m_\phi^2)\, K_1\left(\frac{\sqrt{s}}{T}\right)/\sqrt{s}. \tag{A.32}$$

Next, we want to write $P_{\phi,\ell}, P_{\tilde{\ell},\chi}$ as a function of s. We can compute them as

$$P_{\phi,\ell} = \frac{[s-(m_\phi+m_\ell)^2]^{\frac{1}{2}}[s-(m_\phi-m_\ell)^2]^{\frac{1}{2}}}{2\sqrt{s}} = \frac{s-m_\phi^2}{2\sqrt{s}}\,, \tag{A.33}$$

$$P_{\tilde{\ell},\chi} = \frac{[s-(m_\chi+m_{\tilde{\ell}})^2]^{\frac{1}{2}}[s-(m_\chi-m_{\tilde{\ell}})^2]^{\frac{1}{2}}}{2\sqrt{s}} = \frac{s}{2\sqrt{s}}\,, \tag{A.34}$$

where we neglected all masses except m_ϕ. It follows that $P_{\phi,\ell}P_{\tilde{\ell},\chi} = \frac{s-m_\phi^2}{4}$. The Boltzmann equation then becomes

$$\frac{T}{512\pi^5}\int_{m_\phi^2}^{\infty} ds\, (s - m_\phi^2)^2\, K_1\left(\frac{\sqrt{s}}{T}\right)/\sqrt{s}. \tag{A.35}$$

We can change the variable from s to $z = s/m_\phi^2$, change the number density n to the yield Y, change the variable t to T, and then T to $y = T/m_\phi$ and find

$$\frac{dY_{\ell\phi\to\tilde{\ell}\chi}}{dy} = -\frac{45\, m_\phi}{512 g_S \pi^7 1.66\sqrt{g_\rho}\Lambda}\,\frac{M_{Pl}}{\Lambda}\frac{F(y)}{2}\,, \tag{A.36}$$

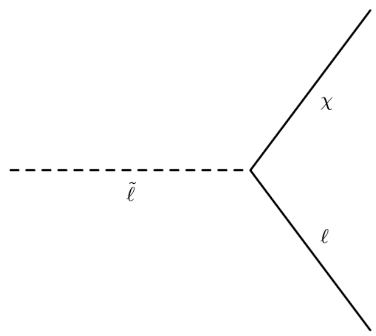

Figure A.2: This is the relevant process for the IR Freeze-In production.

where

$$F(y) = \frac{1}{y^5}\int_1^\infty dz\,\frac{(z-1)^2}{\sqrt{z}}K_1\left(\frac{\sqrt{z}}{y}\right). \tag{A.37}$$

The third and last Feynman diagram on the right side in Figure A.1 has the same Feynman amplitude as the middle one. Therefore this process will have the same contribution to the yield. Its contribution is therefore also represented by Eq.(A.36).

The total UV yield is counting all these contributions together as

$$\frac{dY_{Total}}{dy} = -\frac{45\,m_\phi}{512 g_S \pi^7 1.66\sqrt{g_\rho}\Lambda}\frac{M_{Pl}}{\Lambda}(I(y)+F(y)). \tag{A.38}$$

A.2.2 IR Freeze-In

In the IR Freeze-In the relevant production process is the decay of the mediator, see Figure A.2.

We can write down the amplitude again, this time with a slightly different vertex since the operator has changed due to the spontaneous symmetry breaking

$$\frac{v_\phi}{\Lambda}\overline{u}_s(p_2)P_R\,v_r(p_3), \tag{A.39}$$

where p_2 is the momentum of the lepton and p_3 is the momentum of the dark matter particle. The amplitude is then

$$|\mathcal{M}|^2 = \sum_{r,s}\left(\frac{v_\phi}{\Lambda}\right)^2 \mathrm{Tr}[\overline{u}_s(p_2)P_R\,v_r(p_3)\,\overline{v}_r(p_3)P_L\,u_s(p_2)]. \tag{A.40}$$

Using Eq.(A.15), neglecting the mass of the lepton and using the trace properties of the gamma matrices as in the UV Freeze-In case, this can be rewritten as

$$|\mathcal{M}|^2 = 2\left(\frac{v_\phi}{\Lambda}\right)^2 p_3\cdot p_2. \tag{A.41}$$

Because $m_{\tilde{\ell}}^2 = p_1^2 = (p_3+p_2)^2 = m_\chi^2 + m_\ell^2 + 2p_3\cdot p_2$, neglecting the mass of the lepton, we can write $m_{\tilde{\ell}}^2 - m_\chi^2 = 2p_3\cdot p_2$. The Feynman amplitude for the decay process is then recovered

$$|\mathcal{M}|^2 = \left(\frac{v_\phi}{\Lambda}\right)^2 (m_{\tilde{\ell}}^2 - m_\chi^2). \tag{A.42}$$

From the Feynman amplitude, it is possible to calculate the decay rate via the following formula [71]

$$\Gamma = \frac{p}{8\pi m_{\tilde{\ell}}^2}|\mathcal{M}|^2, \tag{A.43}$$

where the integral over the angles gave a factor of 4π, since the amplitude does not depend on any of the angles. The momentum p of an outgoing particle is computed to be

$$p = \frac{1}{2\,m_{\tilde{\ell}}}(m_{\tilde{\ell}}^2 - m_\chi^2). \tag{A.44}$$

The decay rate can be rewritten as

$$\Gamma = \frac{1}{16\pi}\left(\frac{v_\phi}{\Lambda}\right)^2 m_{\tilde{\ell}}\left(1-\left(\frac{m_\chi}{m_{\tilde{\ell}}}\right)^2\right)^2. \tag{A.45}$$

A.3 Late time ϕ decay channel

It is possible that the dynamical fluctuation of ϕ, $\delta\phi$, decays into a lepton, χ and the mediator, thereby creating dark matter after ϕ has frozen out. The question here is if this channel of dark matter production has a significant effect on the dark matter relic abundance. It will be shown that this channel has a negligible effect on the dark matter production for the parameters of the model chosen in such a way that they are valid for the minimal model, see the discussion about scales in section 6, while also representing the maximal possible contribution for the $\delta\phi$ decay to the relic abundance.

To investigate this particular interaction, the branching ratio needs to be examined. The branching ratio is defined as the ratio of the decay rate of the process of interest, here $\delta\phi \to \chi\ell\tilde{\ell}$, and the total decay rate of $\delta\phi$. In general, a quartic interaction of the type $\lambda_{\phi\tilde{\ell}}|\phi|^2|\tilde{\ell}|^2$ is allowed in the Lagrangian, Eq.(3.3). Even if $\lambda_{\phi\tilde{\ell}}$ is small, this interaction induces a decay channel of the type $\delta\phi \to \tilde{\ell}\tilde{\ell}$. Since the coupling for $\delta\phi \to \chi\ell\tilde{\ell}$ is v_ϕ/Λ, the total decay rate will be dominated by the decay into two mediators as soon as $v_\phi/\Lambda < \lambda_{\phi\tilde{\ell}}$. In this regime, the resulting branching ratio can be estimated as

$$\mathrm{Br} \equiv BR_{\delta\phi\to\chi\ell\tilde{\ell}} \sim \left(\frac{v_\phi}{\Lambda\,\lambda_{\phi\tilde{\ell}}}\right)^2. \tag{A.46}$$

There is also an additional suppression effect, since the $\delta\phi$ decay into dark matter is a three body interaction and therefore has a three body phase space, while the decay into mediators has a two body phase space, however this effect is neglected. This type of dark matter production will not have a significant effect even if the phase space suppression is not accounted for.

Then, Y_χ = Br $Y_{\delta\phi}$, hence Ω_χ = Br $\frac{m_\chi}{m_{\delta\phi}}\Omega_{\delta\phi}$. A small calculation shows that

$$\Omega_\chi h^2 \sim \frac{8\pi G h^2}{3H_0^2} m_\chi\,\mathrm{Br}\,\frac{2\pi^2 g_*}{45} T_0^3 Y_{\delta\phi}^\infty, \tag{A.47}$$

where the yield of ϕ for this production channel is

$$Y_{\delta\phi}^\infty = g\,45\left(\frac{x_f}{2\pi}\right)^{3/2}\frac{e^{-x_f}}{2\pi^2 g_*}, \tag{A.48}$$

assuming that $\delta\phi$ follows the equilibrium density and with $x_f = m_{\delta\phi}/T_f$, the moment of freeze-out of $\delta\phi$. This approximation takes the equilibrium density of $\delta\phi$ at a time of freeze-out x_f and assumes this density stays the same for all time after freeze-out. It is possible to make a plot for the contribution of this channel by varying the moment of freeze-out x_f around the typical value of freeze-out which is $x_f \sim 20$. This is displayed in Figure A.3 using the parameters from Table A.1 and taking $\lambda_{\phi\tilde{\ell}}$ of order 1.

On the vertical axis of the plot, there is the relic abundance and it is seen that the maximum contribution of the $\delta\phi$ has an order of magnitude around 10^{-8}, which is much smaller than the expected dark matter abundance $\Omega h^2 = 0.12$, hence it is concluded that this channel is not relevant to the dark matter production.

It is also possible to reverse this question and look at a bound for the branching ratio such that this contribution is negligible. By fixing x_f to its typical value $x_f \sim 20$, it can be found that for $BR_{\delta\phi \to \chi\ell\tilde{\ell}} < 5 \cdot 10^{-3}$, the $\delta\phi$ decay channel contribution is negligible compared to the other dark matter production channels if m_χ = 1 GeV and if we take a normal freeze-out value of $x_f \sim 20$. This value for the branching ratio is never achieved for the relevant scope of the parameters in this thesis, even for small $\lambda_{\phi\tilde{\ell}}$, since $v_\phi/\Lambda \ll 1$.

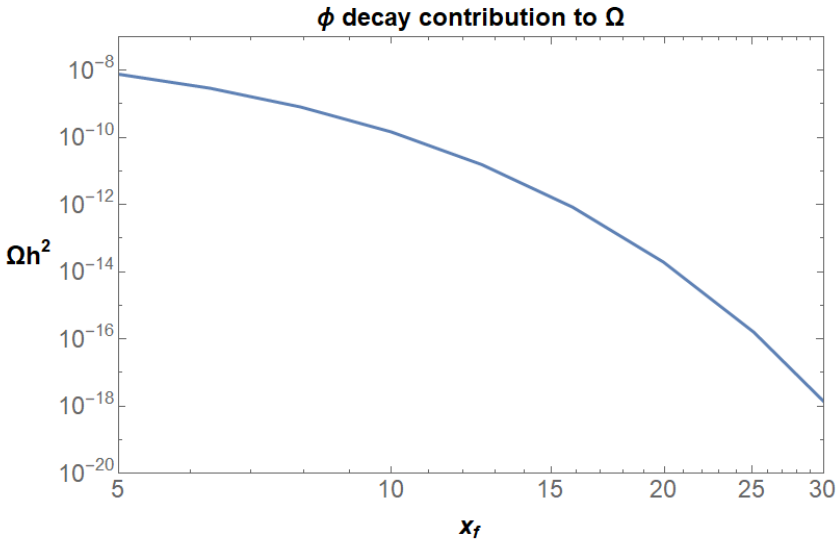

Figure A.3: This figure gives the dark matter relic abundance phi decay channel contribution as a function of x_f, the time of freeze-out of $\delta\phi$. To calculate the abundance, v_ϕ was chosen to be 10^7 GeV and $\lambda_{\phi\tilde{\ell}}$ was taken of order 1. For these particular values for the parameters, see Table A.1, the contribution to the dark matter relic abundance due to the $\delta\phi$ decay is negligible.

Λ	m_χ	v_ϕ
10^{14} GeV	1 GeV	10^7 GeV

Table A.1: To calculate the $\delta\phi$ decay contribution in Figure A.3, the following parameters in the table are chosen. These represent the values for these parameters which would produce the biggest contribution from $\delta\phi$ decay for the relevant scales of these parameters in the minimal model. This is only one example in the parameter space, however it does give a good idea of the contribution to the dark matter because it is an upper bound for the relevant parameter range in the dark matter minimal model of the thesis.

References

[1] Sean Carroll. *Spacetime and Geometry: An introduction to General Relativity: Pearson New International dition*. Pearson Education Limited.

[2] Alan H. Guth. "Inflationary universe: A possible solution to the horizon and flatness problems". In: *Phys. Rev. D* 23 (2 Jan. 1981), pp. 347–356. DOI: 10.1103/PhysRevD.23.347. URL: https://link.aps.org/doi/10.1103/PhysRevD.23.347.

[3] Lev Kofman, Andrei D. Linde, and Alexei A. Starobinsky. "Reheating after inflation". In: *Phys. Rev. Lett.* 73 (1994), pp. 3195–3198. DOI: 10.1103/PhysRevLett.73.3195. arXiv: hep-th/9405187.

[4] Planck Collaboration et al. *Planck 2018 results. VI. Cosmological parameters*. 2020. arXiv: 1807.06209 [astro-ph.CO].

[5] Planck Collaboration et al. "Planck 2018 results - I. Overview and the cosmological legacy of Planck". In: *A&A* 641 (2020), A1. DOI: 10.1051/0004-6361/201833880. URL: https://doi.org/10.1051/0004-6361/201833880.

[6] C. L. Bennett et al. "TheMicrowave Anisotropy ProbeMission". In: *The Astrophysical Journal* 583.1 (Jan. 2003), pp. 1–23. ISSN: 1538-4357. DOI: 10.1086/345346. URL: http://dx.doi.org/10.1086/345346.

[7] "The Scientific programme of Planck". In: (Apr. 2006). Ed. by J. Tauber et al. arXiv: astro-ph/0604069.

[8] Andrew Liddle. *An introduction to modern cosmology*. Wiley, 2015.

[9] T. S. van Albada et al. "Distribution of dark matter in the spiral galaxy NGC 3198." In: *apj* 295 (Aug. 1985), pp. 305–313. DOI: 10.1086/163375.

[10] Aaron D. Lewis, David A. Buote, and John T. Stocke. "ChandraObservations of A2029: The Dark Matter Profile Down to below 0.01rvirin an Unusually Relaxed Cluster". In: *The Astrophysical Journal* 586.1 (Mar. 2003), pp. 135–142. ISSN: 1538-4357. DOI: 10.1086/367556. URL: http://dx.doi.org/10.1086/367556.

[11] Richard Massey, Thomas Kitching, and Johan Richard. "The dark matter of gravitational lensing". In: *Rept. Prog. Phys.* 73 (2010), p. 086901. DOI: 10.1088/0034-4885/73/8/086901. arXiv: 1001.1739 [astro-ph.CO].

[12] Douglas Clowe et al. "A Direct Empirical Proof of the Existence of Dark Matter". In: *The Astrophysical Journal* 648.2 (Aug. 2006), pp. L109–L113. ISSN: 1538-4357. DOI: 10.1086/508162. URL: http://dx.doi.org/10.1086/508162.

[13] N. Aghanim et al. "Planck 2018 results". In: *Astronomy & Astrophysics* 641 (Sept. 2020), A5. ISSN: 1432-0746. DOI: 10.1051/0004-6361/201936386. URL: http://dx.doi.org/10.1051/0004-6361/201936386.

[14] Joel R. Primack and Michael A. K. Gross. "Hot dark matter in cosmology". In: (July 2000). Ed. by David O. Caldwell. arXiv: astro-ph/0007165.

[15] Rennan Barkana, Zoltan Haiman, and Jeremiah P. Ostriker. "Constraints on warm dark matter from cosmological reionization". In: *Astrophys. J.* 558 (2001), p. 482. DOI: 10.1086/322393. arXiv: astro-ph/0102304.

[16] M. Aker et al. *First direct neutrino-mass measurement with sub-eV sensitivity*. 2021. arXiv: 2105.08533 [hep-ex].

[17] A. Boyarsky et al. "Sterile neutrino Dark Matter". In: *Progress in Particle and Nuclear Physics* 104 (Jan. 2019), pp. 1–45. ISSN: 0146-6410. DOI: 10.1016/j.ppnp.2018.07.004. URL: http://dx.doi.org/10.1016/j.ppnp.2018.07.004.

[18] John Preskill, Mark B. Wise, and Frank Wilczek. "Cosmology of the Invisible Axion". In: *Phys. Lett. B* 120 (1983). Ed. by M. A. Srednicki, pp. 127–132. DOI: 10.1016/0370-2693(83)90637-8.

[19] Timothy D. Brandt. "Constraints on MACHO Dark Matter from Compact Stellar Systems in Ultra-Faint Dwarf Galaxies". In: *Astrophys. J. Lett.* 824.2 (2016), p. L31. DOI: 10.3847/2041-8205/824/2/L31. arXiv: 1605.03665 [astro-ph.GA].

[20] Carlos Blanco et al. "Z′ mediated WIMPs: dead, dying, or soon to be detected?" In: *JCAP* 11 (2019), p. 024. DOI: 10.1088/1475-7516/2019/11/024. arXiv: 1907.05893 [hep-ph].

[21] Giorgio Arcadi et al. "The waning of the WIMP? A review of models, searches, and constraints". In: *Eur. Phys. J. C* 78.3 (2018), p. 203. DOI: 10.1140/epjc/s10052-018-5662-y. arXiv: 1703.07364 [hep-ph].

[22] Lawrence J. Hall et al. "Freeze-In Production of FIMP Dark Matter". In: *JHEP* 03 (2010), p. 080. DOI: 10.1007/JHEP03(2010)080. arXiv: 0911.1120 [hep-ph].

[23] Nicolás Bernal et al. "The dawn of FIMP Dark Matter: A review of models and constraints". In: *International Journal of Modern Physics A* 32.27 (Sept. 2017), p. 1730023. ISSN: 1793-656X. DOI: 10.1142/s0217751x1730023x. URL: http://dx.doi.org/10.1142/S0217751X1730023X.

[24] Benjamin W. Lee and Steven Weinberg. "Cosmological Lower Bound on Heavy-Neutrino Masses". In: *Phys. Rev. Lett.* 39 (4 July 1977), pp. 165–168. DOI: 10.1103/PhysRevLett.39.165. URL: https://link.aps.org/doi/10.1103/PhysRevLett.39.165.

[25] Tanedo F. "Defense Against the Dark Arts: Notes on dark matter and particle physics." In: (2011), p. 81. URL: https://www.physics.uci.edu/~tanedo/files/notes/DMNotes.pdf.

[26] Joakim Edsjo and Paolo Gondolo. "Neutralino relic density including coannihilations". In: *Phys. Rev. D* 56 (1997), pp. 1879–1894. DOI: 10.1103/PhysRevD.56.1879. arXiv: hep-ph/9704361.

[27] K. S. Babu. "TASI Lectures on Flavor Physics". In: (2009). arXiv: 0910.2948 [hep-ph].

[28] Marco Fedele, Alessio Mastroddi, and Mauro Valli. "Minimal Froggatt-Nielsen Textures". In: (Sept. 2020). arXiv: 2009.05587 [hep-ph].

[29] M. Drees, R. Godbole, and P. Roy. *Theory and phenomenology of sparticles: An account of four-dimensional N=1 supersymmetry in high energy physics*. 2004.

[30] Gerard Jungman, Marc Kamionkowski, and Kim Griest. "Supersymmetric dark matter". In: *Physics Reports* 267.5-6 (Mar. 1996), pp. 195–373. ISSN: 0370-1573. DOI: 10.1016/0370-1573(95)00058-5. URL: http://dx.doi.org/10.1016/0370-1573(95)00058-5.

[31] Fatemeh Elahi, Christopher Kolda, and James Unwin. "UltraViolet freeze-in". In: *Journal of High Energy Physics* 2015.3 (Mar. 2015). ISSN: 1029-8479. DOI: 10.1007/jhep03(2015)048. URL: http://dx.doi.org/10.1007/JHEP03(2015)048.

[32] Shao-Long Chen and Zhaofeng Kang. "On ultraviolet freeze-in dark matter during reheating". In: *Journal of Cosmology and Astroparticle Physics* 2018.05 (May 2018), pp. 036–036. ISSN: 1475-7516. DOI: 10.1088/1475-7516/2018/05/036. URL: http://dx.doi.org/10.1088/1475-7516/2018/05/036.

[33] Nelson Christensen. "Stochastic gravitational wave backgrounds". In: *Reports on Progress in Physics* 82.1 (Nov. 2018), p. 016903. ISSN: 1361-6633. DOI: 10.1088/1361-6633/aae6b5. URL: http://dx.doi.org/10.1088/1361-6633/aae6b5.

[34] Albert Einstein. "Näherungsweise Integration der Feldgleichungen der Gravitation". In: *Sitzungsberichte der Königlich Preußischen Akademie der Wissenschaften (Berlin* (Jan. 1916), pp. 688–696.

[35] B P Abbott et al. "LIGO: the Laser Interferometer Gravitational-Wave Observatory". In: *Reports on Progress in Physics* 72.7 (June 2009), p. 076901. DOI: 10.1088/0034-4885/72/7/076901. URL: https://doi.org/10.1088/0034-4885/72/7/076901.

[36] F Acernese et al. "Advanced Virgo: a second-generation interferometric gravitational wave detector". In: *Classical and Quantum Gravity* 32.2 (Dec. 2014), p. 024001. DOI: 10.1088/0264-9381/32/2/024001. URL: https://doi.org/10.1088/0264-9381/32/2/024001.

[37] Yoichi Aso et al. "Interferometer design of the KAGRA gravitational wave detector". In: *Phys. Rev. D* 88 (4 Aug. 2013), p. 043007. DOI: 10.1103/PhysRevD.88.043007. URL: https://link.aps.org/doi/10.1103/PhysRevD.88.043007.

[38] B. P. Abbott et al. "Observation of Gravitational Waves from a Binary Black Hole Merger". In: *Phys. Rev. Lett.* 116 (6 Feb. 2016), p. 061102. DOI: 10.1103/PhysRevLett.116.061102. URL: https://link.aps.org/doi/10.1103/PhysRevLett.116.061102.

[39] B. P. Abbott et al. "GW170817: Implications for the Stochastic Gravitational-Wave Background from Compact Binary Coalescences". In: *Phys. Rev. Lett.* 120 (9 Feb. 2018), p. 091101. DOI: 10.1103/PhysRevLett.120.091101. URL: https://link.aps.org/doi/10.1103/PhysRevLett.120.091101.

[40] Pau Amaro-Seoane et al. *Laser Interferometer Space Antenna*. 2017. arXiv: 1702.00786 [astro-ph.IM].

[41] Chiara Caprini et al. "Reconstructing the spectral shape of a stochastic gravitational wave background with LISA". In: *JCAP* 11 (2019), p. 017. DOI: 10.1088/1475-7516/2019/11/017. arXiv: 1906.09244 [astro-ph.CO].

[42] N. Aghanim et al. "Planck 2018 results. VI. Cosmological parameters". In: *Astron. Astrophys.* 641 (2020), A6. DOI: 10.1051/0004-6361/201833910. arXiv: 1807.06209 [astro-ph.CO].

[43] Eric Thrane and Joseph D Romano. "Sensitivity curves for searches for gravitational-wave backgrounds". English. In: *Physical Review D* 88.12 (2013), pp. 1–11. ISSN: 2470-0010. DOI: 10.1103/PhysRevD.88.124032.

[44] Matthew R. Adams and Neil J. Cornish. "Detecting a Stochastic Gravitational Wave Background in the presence of a Galactic Foreground and Instrument Noise". In: *Phys. Rev. D* 89.2 (2014), p. 022001. DOI: 10.1103/PhysRevD.89.022001. arXiv: 1307.4116 [gr-qc].

[45] Jeff Crowder and Neil J. Cornish. "Beyond LISA: Exploring future gravitational wave missions". In: *Phys. Rev. D* 72 (2005), p. 083005. DOI: 10.1103/PhysRevD.72.083005. arXiv: gr-qc/0506015.

[46] M. Punturo et al. "The Einstein Telescope: A third-generation gravitational wave observatory". In: *Class. Quant. Grav.* 27 (2010). Ed. by Fulvio Ricci, p. 194002. DOI: 10.1088/0264-9381/27/19/194002.

[47] Eric Thrane and Joseph D. Romano. "Sensitivity curves for searches for gravitational-wave backgrounds". In: *Physical Review D* 88.12 (Dec. 2013). ISSN: 1550-2368. DOI: 10.1103/physrevd.88.124032. URL: http://dx.doi.org/10.1103/PhysRevD.88.124032.

[48] Kent Yagi, Norihiro Tanahashi, and Takahiro Tanaka. "Probing the size of extra dimension with gravitational wave astronomy". In: *Phys. Rev. D* 83 (2011), p. 084036. DOI: 10.1103/PhysRevD.83.084036. arXiv: 1101.4997 [gr-qc].

[49] Nathaniel Craig et al. "Ripples in Spacetime from Broken Supersymmetry". In: *JHEP* 21 (2020), p. 184. DOI: 10.1007/JHEP02(2021)184. arXiv: 2011.13949 [hep-ph].

[50] B. Sathyaprakash et al. "Scientific Objectives of Einstein Telescope". In: *Class. Quant. Grav.* 29 (2012). Ed. by Mark Hannam et al. [Erratum: Class.Quant.Grav. 30, 079501 (2013)], p. 124013. DOI: 10.1088/0264-9381/29/12/124013. arXiv: 1206.0331 [gr-qc].

[51] Mariano Quiros. "Finite temperature field theory and phase transitions". In: *ICTP Summer School in High-Energy Physics and Cosmology*. Jan. 1999. arXiv: hep-ph/9901312.

[52] Michele Maggiore. *Gravitational waves*. Oxford University Press, 2014.

[53] G. 't Hooft and M. Veltman. "Regularization and renormalization of gauge fields". In: *Nuclear Physics B* 44.1 (1972), pp. 189–213. ISSN: 0550-3213. DOI: https://doi.org/10.1016/0550-3213(72)90279-9. URL: https://www.sciencedirect.com/science/article/pii/0550321372902799.

[54] Greg W. Anderson and Lawrence J. Hall. "Electroweak phase transition and baryogenesis". In: *Phys. Rev. D* 45 (8 Apr. 1992), pp. 2685–2698. DOI: 10.1103/PhysRevD.45.2685. URL: https://link.aps.org/doi/10.1103/PhysRevD.45.2685.

[55] F. Englert and R. Brout. "Broken Symmetry and the Mass of Gauge Vector Mesons". In: *Phys. Rev. Lett.* 13 (9 Aug. 1964), pp. 321–323. DOI: 10.1103/PhysRevLett.13.321. URL: https://link.aps.org/doi/10.1103/PhysRevLett.13.321.

[56] Peter W. Higgs. "Broken Symmetries and the Masses of Gauge Bosons". In: *Phys. Rev. Lett.* 13 (16 Oct. 1964), pp. 508–509. DOI: 10.1103/PhysRevLett.13.508. URL: https://link.aps.org/doi/10.1103/PhysRevLett.13.508.

[57] Serguei Chatrchyan et al. "Observation of a New Boson at a Mass of 125 GeV with the CMS Experiment at the LHC". In: *Phys. Lett. B* 716 (2012), pp. 30–61. DOI: 10.1016/j.physletb.2012.08.021. arXiv: 1207.7235 [hep-ex].

[58] Edward Witten. "Cosmological Consequences of a Light Higgs Boson". In: *Nucl. Phys. B* 177 (1981), pp. 477–488. DOI: 10.1016/0550-3213(81)90182-6.

[59] Gerald V. Dunne and Hyunsoo Min. "Beyond the thin-wall approximation: Precise numerical computation of prefactors in false vacuum decay". In: *Phys. Rev. D* 72 (12 Dec. 2005), p. 125004. DOI: 10.1103/PhysRevD.72.125004. URL: https://link.aps.org/doi/10.1103/PhysRevD.72.125004.

[60] Victor Guada, Miha Nemevšek, and Matevž Pintar. "FindBounce: Package for multi-field bounce actions". In: *Comput. Phys. Commun.* 256 (2020), p. 107480. DOI: 10.1016/j.cpc.2020.107480. arXiv: 2002.00881 [hep-ph].

[61] Chiara Caprini et al. "Science with the space-based interferometer eLISA. II: Gravitational waves from cosmological phase transitions". In: *JCAP* 04 (2016), p. 001. DOI: 10.1088/1475-7516/2016/04/001. arXiv: 1512.06239 [astro-ph.CO].

[62] Mark Hindmarsh et al. “Numerical simulations of acoustically generated gravitational waves at a first order phase transition”. In: *Phys. Rev. D* 92.12 (2015), p. 123009. DOI: 10.1103/PhysRevD.92.123009. arXiv: 1504.03291 [astro-ph.CO].

[63] A.D. Linde. “Decay of the false vacuum at finite temperature”. In: *Nuclear Physics B* 216.2 (1983), pp. 421–445. ISSN: 0550-3213. DOI: https://doi.org/10.1016/0550-3213(83)90293-6. URL: https://www.sciencedirect.com/science/article/pii/0550321383902936.

[64] Dario Buttazzo, Filippo Sala, and Andrea Tesi. “Singlet-like Higgs bosons at present and future colliders”. In: *JHEP* 11 (2015), p. 158. DOI: 10.1007/JHEP11(2015)158. arXiv: 1505.05488 [hep-ph].

[65] Morad Aaboud et al. “Search for heavy charged long-lived particles in proton-proton collisions at $\sqrt{s} = 13$ TeV using an ionisation measurement with the ATLAS detector”. In: *Phys. Lett. B* 788 (2019), pp. 96–116. DOI: 10.1016/j.physletb.2018.10.055. arXiv: 1808.04095 [hep-ex].

[66] “Search for heavy stable charged particles with $12.9\ \mathrm{fb}^{-1}$ of 2016 data”. In: (2016).

[67] Lorenzo Calibbi et al. “Displaced new physics at colliders and the early universe before its first second”. In: *JHEP* 05 (2021), p. 234. DOI: 10.1007/JHEP05(2021)234. arXiv: 2102.06221 [hep-ph].

[68] Scott Dodelson. *Modern Cosmology*. Amsterdam: Academic Press, 2003. ISBN: 978-0-12-219141-1.

[69] Mark Thomson. *Modern particle physics*. New York: Cambridge University Press, 2013. ISBN: 978-1-107-03426-6.

[70] D.R. Tovey and J.D. Jackson. URL: https://pdg.lbl.gov/2017/mobile/reviews/pdf/rpp2017-rev-kinematics-m.pdf.

[71] David Griffiths. *Introduction to elementary particles*. 2008. ISBN: 978-3-527-40601-2.